ION BEAM ASSISTED DEPOSITION OF BIAXIALLY-TEXTURED THIN FILMS FOR ENERGY APPLICATIONS

by
Sicong Sun

A dissertation submitted to the Materials Science and Engineering Program,
Cullen College of Engineering
in partial fulfillment of the requirements for the degree of

DOCTOR OF PHILOSOPHY

in Materials Science and Engineering

Chair of Committee: Venkat Selvamanickam

Committee Member: Jae-Hyun Ryou

Committee Member: James K. Meen

Committee Member: Haleh Ardebili

Committee Member: Jiming Bao

University of Houston
May 2020

ACKNOWLEDGMENTS

Firstly, I would like to present my sincere gratitude to my advisor, Prof. Venkat Selvamanickam, for offering me an excellent opportunity to join this fantastic group and providing his guidance throughout all my research projects. I also would like to show my most significant appreciation for his support in the research and coursework, his sponsorship for attending academic conferences, and his recommendation for my scholarship applications over the past five years. His earnestness, meticulousness, and persistence will keep inspiring me in my future professional development and career.

I also want to thank Prof. Jae-Hyun Ryou and Prof. James K. Meen, for their instructions on all the material characterization tools. Also, I would like to thank Prof. Haleh Ardebili and Prof. Jiming Bao, for serving as committee members of my Ph.D. dissertation defense. Their insightful advices are very valuable to me.

I want to show my gratitude to Dr. Pavel Dutta, Dr. Ying Gao, and Dr. Xiaofen Li; they helped me build up a solid background related to our research field. Also, I benefited a lot from their analytical skills and learning abilities.

I also appreciated great help from Prof. Jarek Wosik, Dr. Eduard Galstyan, Dr. Goran Majkic, and Mr. George Pope; their professional guidance helped me avoid many unnecessary detours in my research.

All my colleagues, including Dr. Yao Yao, Dr. Yongkuan Li, Dr. Devendra Khatiwada, Dr. Rudra Pratap, Mehdi Kochat, Sara Pouladi, Siwei Chen, Carlos Favela, Chuanze Zhang, Sahil Sharma and Bo Yu, gave me lots of support and help on my research works.

All my special gratefulness are due to my parents and beloved girlfriend Yanan; their encouragement and support helped me gain this unique experience in my life.

ABSTRACT

Ion beam assisted deposition (IBAD) is a promising way to realize high efficient and scalable manufacturing of a single-crystal-like, biaxially-textured thin film on various substrates. This biaxially-textured film has been employed for different kinds of purposes, such as epitaxial growth of single-crystal-like high-temperature superconductor (HTS) films and replacing the wafer-based epitaxial process for thin-film optoelectronic and electrical applications such as flexible solar cells and thin-film transistors.

This dissertation is focused on different IBAD processes that could benefit both the semiconductor and superconductor fields. A highly biaxially-textured IBAD TiN was demonstrated on the Hastelloy tape without foreign oxide seed layers. This enables the feasibility of all-electrically conductive buffers on Hastelloy.

The conventional architecture of $LaMnO_3$/IBAD MgO for HTS tapes was also improved through the use of Ag/TiN intermediate layers. The buffer architecture was optimized to achieve significant improvement in texture and avoid possible crystalline defects. The texture of $LaMnO_3$ was improved to (002) $\Delta\omega$ of 1.7º and (110) $\Delta\phi$ of 2.45º using Ag/TiN layers.

Additionally, IBAD MgO and related HTS cap layers have been developed on flexible non-metallic tape. The non-metallic substrate could extend the scope of HTS materials to unconventional applications such as high-quality flexible MRI receiving coils and transmission lines for cryogenic quantum computing systems.

Finally, a novel architecture of single-crystalline-like ultra-bandgap semiconductor β-Ga_2O_3 film on IBAD MgO-capped flexible Hastelloy was demonstrated. The β-Ga_2O_3 film shows a strong biaxial texture with (400) $\Delta\omega$ of 1.54º and {002} $\Delta\phi$ of 4.81º. The crystal orientation relationship between the β-Ga_2O_3 and IBAD MgO was also studied.

TABLE OF CONTENTS

LIST OF TABLES

LIST OF FIGURES

CHAPTER 1 INTRODUCTION TO SINGLE-CRYSTALLINE-LIKE BUFFER ARCHITECTURES

1.1 Introduction

Epitaxial growth is one of the most common methods that have been widely used in semiconductor and superconductor industries. In most situations, the epitaxy depends on the crystalline structure condition of the substrate. In this case, there are many requirements to achieve epitaxial growth since they establish strict constraints for the geometry and crystalline state of the substrate. Since the 1960s, with the boost in the semiconductor industry, scale up of wafer size was begun to promote the efficiency of large-scale semiconductor device fabrication [1], [2]. However, even with tremendous investments and efforts of researchers, the wafer size has risen from 51 mm to only 450 mm (for silicon) [3]. Moreover, the large wafers, particularly for the III-V group semiconductors, remain expensive [2].

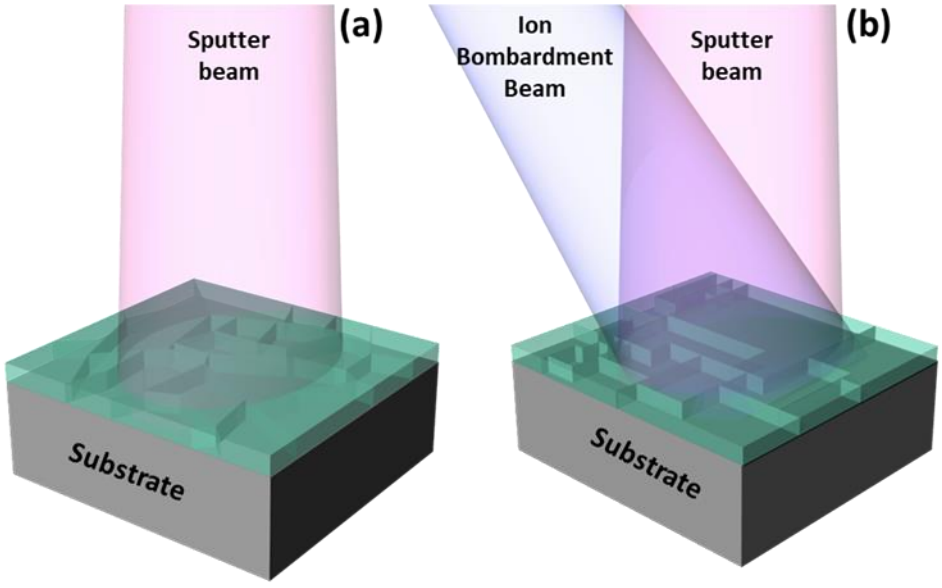

Figure 1.1 Schematic demonstration of (a) fiber-textured film growth with sputter beam only; (b) biaxially-textured film growth with sputter beam and ion bombardment beam.

Alternative methods to realize epitaxial thin film growth to reduce the dependency on the single crystal wafers have been explored. Usually, films grown on non-single crystal substrate are amorphous, polycrystalline, or fiber-textured [4]. The fiber-texture indicates that the grains in the film are aligned only uniaxially, normal to the substrate, as illustrated in Figure 1.1(a). However, the grains are still tilted with a random orientation in the plane of the film. This uniaxial-textured film can form without an additional heating source and orientation is dominantly such as to minimize the interfacial energy between the substrate and the deposited material. As an example, the silver (Ag) deposited on amorphous glass by thermal evaporation exhibits a <111> crystallite orientation.

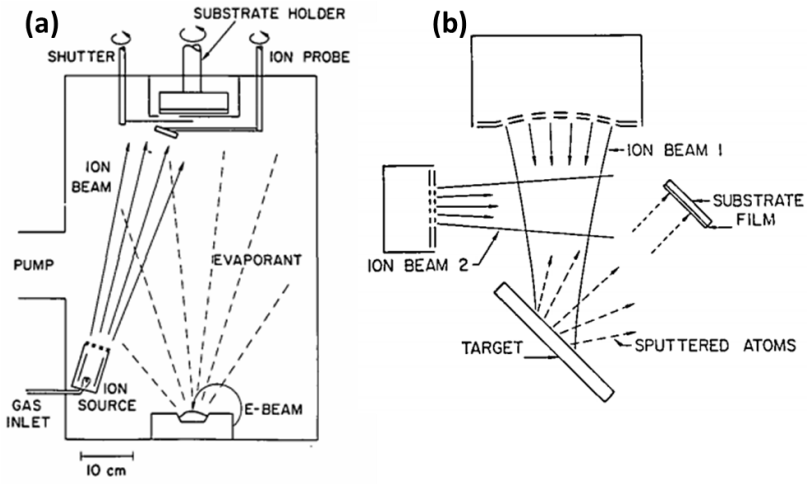

Figure 1.2 (a) System with e-beam evaporator for film deposition and ion source for bombardment; (b) System with dual ion sources for sputter deposition and ion bombardment [5].

In the 1980s, Rossnagel and other researchers of IBM discovered that Argon (Ar) ion beam bombardment can help align the grains in the thin film azimuthally during deposition of niobium (Nb) on amorphous silica substrate by ion beam sputtering of a Nb target [5], [6], [7]. The grains then showed a preferred orientation in the film instead

of random alignment, and the degree of order increased when the assist bombardment beam possessed a higher ion/atom flux ratio (Figure 1.1 b). They also proposed a prototype apparatus for ion beam assisted deposition (IBAD). As illustrated in figure 1.2, one version uses an inclined ion source with an e-beam evaporator as the material source, while another version employs dual ion beam deposition, where one ion beam is used to sputter the target, and the other is used for ion bombardment during the deposition process [5].

The need for biaxial alignment to achieve high critical current density in high-temperature superconductor (HTS) material motivated research on biaxially-textured buffers in the 1990s. Based on the IBAD technique, Iijima developed a way to realize the a, b axes alignment of yttrium barium copper oxide ($YBa_2Cu_3O_{7-x}$, abbreviated to YBCO) grains [8]. A single-crystal-like, highly-aligned biaxially-textured yttria-stabilized zirconia (YSZ) film was grown by IBAD on polished Hastelloy on which an HTS layer with strong a, b axes alignment was demonstrated. The strong a,b axes alignment enabled a high critical current density of the YBCO film [9]. After this demonstration, many researchers investigated the influences of different features of the IBAD method, including ion bombardment time, incident angle, related materials, and possible ways to scale up for long-length deposition [10], [11], [12], [13], [14]. The single-crystal-like biaxially-textured buffer has turned out to be an enabling technology for HTS wire tape manufacturing.

Besides the IBAD technique, there is also another method to obtain this single-crystal-like biaxially-textured buffer called rolling-assisted biaxially-textured substrate

(RABiTS) that can be used for HTS tapes [15]. Both methods will be discussed in detail in the next section.

The grain alignment in a single-crystal-like biaxially-textured film can be categorized by two metrics. The first one is used to evaluate how the grains are tilted from the normal direction of the substrate—that is, the "out-of-plane texture". The second one is used to examine the azimuthal twist of grains—the "in-plane texture". The texture spreads of the out-of-plane and in-plane texture are expressed by the full-width-half-maxima (FWHM) of the related crystalline plane X-ray Diffraction (XRD) rocking curves, as $\Delta\omega$ and $\Delta\phi$, respectively.

1.2 Methods to create a single-crystalline-like film

1.2.1 Ion beam assisted deposition (IBAD)

The IBAD technique is the most promising method to introduce a biaxial texture to a film on a wide range of substrates. A state-of-art IBAD system can achieve fast, large-scale, industrial level roll-to-roll manufacturing of an IBAD magnesium oxide (MgO) cap layer on polished Hastelloy tape (C-276). The IBAD system used in this work is equipped with a roll-to-roll tape feeding system and shutter-controlled deposition, which makes it suitable for both a long tape process and a stationary short sample.

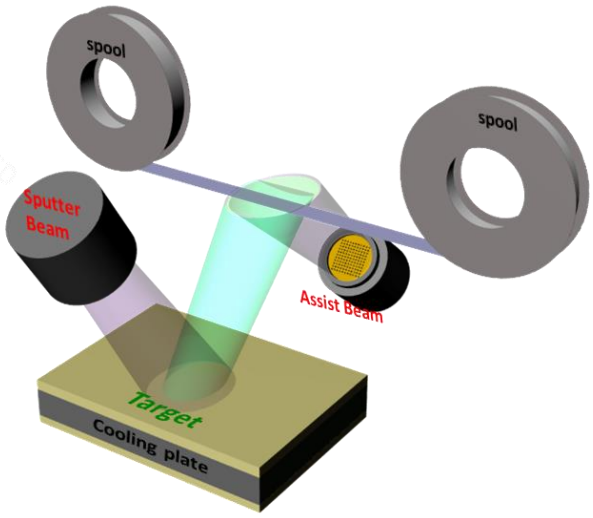

Figure 1.3 Schematic of IBAD process.

Figure 1.3 provides a schematic view of the IBAD process. This dual ion beam system can ion bombard the target and the substrate simultaneously. A seed layer can be deposited on the substrate by ion bombarding the target only. After the amorphous seed layer deposition, the target assembly can be flipped over to deposit a second material under ion bombardment to grow a biaxially- textured film. The substrate is continuously delivered from a spool during deposition to achieve a long, flexible tape with the biaxially-textured film.

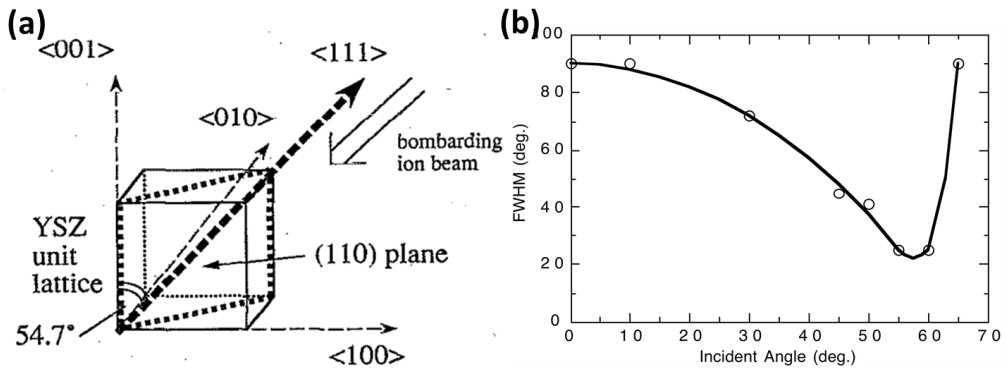

Figure 1.4 Schematic view of YSZ unit cell and ion bombardment orientation; (b) The changes of YSZ (111) FWHM as a function of bombarding ion beam incident angle [16], [17].

Further research on IBAD YSZ revealed that the incident angle of the assist beam is a critical factor in determining the crystallographic spread of the biaxially-textured film [18]. A (110)-oriented fiber-textured YSZ may form spontaneously without an assist beam since it is the crystalline plane with the lowest surface energy. The addition of the assist ion beam causes the (110)-oriented fiber-texture grains to be replaced by (100)-oriented biaxially-textured texture grains. The YSZ (111) in-plane texture shows significant improvement when the incident assist beam angle is at 55º to the substrate normal, as shown in figure 1.4. This is because 54.7º is the angle between YSZ <111> and the substrate normal, which means the biaxial alignment of the YSZ grains is established by the <111>-oriented ion channeling.

The relationship between the incident beam and ion channeling was modeled by Sonnenberg by columnar structure development [14]. In this model, a shadowing effect of the grains with the channeling direction is proposed. During the ion bombardment process, the effect of ion etching will be at the lowest level for the grains whose channeling direction is parallel to the bombardment beam, allowing these grains to be fully developed. On the contrary, the grains in which the channeling direction is tilted from the ion beam could suffer from ion bombardment, and their growth would then be terminated. Figure 1.5 illustrates the whole process of IBAD biaxial texture formation using Pyrex glass as a substrate for IBAD YSZ growth. At the initial stage, the film is composed of grains of different orientations. Ion bombardment by the assist beam could continuously etch the misoriented grains which have different channeling directions. Meanwhile, the grains with the appropriate channeling direction can avoid the etch

effect by the assist ion beam and continue their growth. The as-grown columnar grains can shadow unfavorably-oriented grains and finally cover the whole film.

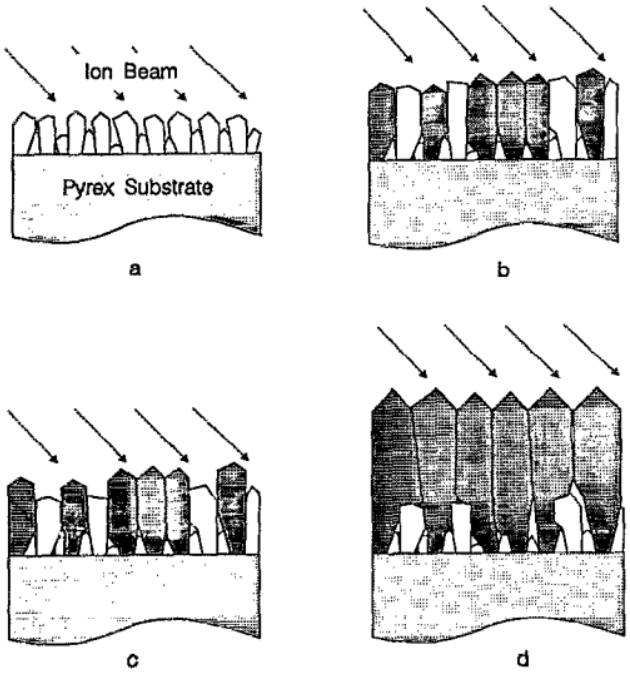

Figure 1.5 The growth process of biaxially textured IBAD YSZ [14].

The in-plane alignment, as proposed in this model, occurred at the growth process, and not during nucleation; the initial film has random in-plane alignment. An experiment on the study of development of IBAD YSZ texture proved that the YSZ film has to reach 1 μm in thickness to realize 12º around the in-plane texture [14], [19].

Other alternative materials have been investigated by the IBAD process after the development of IBAD YSZ, such as cerium oxide (CeO_2) [20], [21], [22], calcium fluoride (CaF_2) [23], [24], titanium nitride (TiN) [25], [26], and MgO [12], [27]. Rock-salt-structured materials are promising due to their quick biaxial texture formation process. Different from the IBAD YSZ texture evolution process, the rock-salt-structured materials such as MgO and TiN can realize a biaxial texture at the grain

nucleation step [28]. Wang first demonstrated IBAD MgO on amorphous silicon nitride (Si_3N_4) [12]. The texture of IBAD MgO can reach the minimal FWHM even at a 10-nm thickness. In this case, the substrate surface may be fully covered by textured MgO crystallites once this thickness is reached.

The reason for the fast texture formation may be the spontaneous preferred alignment of (100) rock-salt-structured MgO. Therefore, the assist ion beam can be used to align the grains with an in-plane orientation from the very beginning. Besides that, the IBAD MgO texture form near room temperature which makes it readily scalable to manufacturing.

Arendt showed that yttrium oxide (Y_2O_3) could function as a seed layer in addition to Si_3N_4 [29]. Only a few nanometer thick amorphous Y_2O_3 is needed for IBAD MgO nucleation. However, as shown in the third chapter, IBAD TiN has been grown on polished Hastelloy without foreign seed layers. The surface roughness (<1 nm) and surface energy conditions of the substrate could therefore be the more critical influences on IBAD layer growth.

1.2.2 Rolling-assisted biaxially textured substrate (RABiTS)

Rolling-assisted biaxially textured substrate (RABiTS) is a large-scale thermomechanical process developed in the 1990s with the initial purpose of realizing the epitaxial growth of the high-temperature superconductors (HTS) [15]. The process of nickel (Ni)-based RABiTs tape is illustrated in Figure 1.6. High-purity (99.99%) Ni bar/plate is continuously mechanically cold-rolled to a thin sheet until more than 90% reduction in cross sectional area has occurred within a copper-type rolling texture. The

following annealing step induces recrystallization of Ni which consists of cube- textured {001}<001> grains. The final biaxially-textured HTS thin film can be realized on top of this textured substrate with appropriate epitaxial buffer layers. A biaxially-textured germanium (Ge) template has also been demonstrated on textured $Ni_{0.95}W_{0.05}$ (NiW) tape with different cap layers [30]. This technique is promising for applications in the semiconductor field, such as solar cells, owing to its flexibility and low costs.

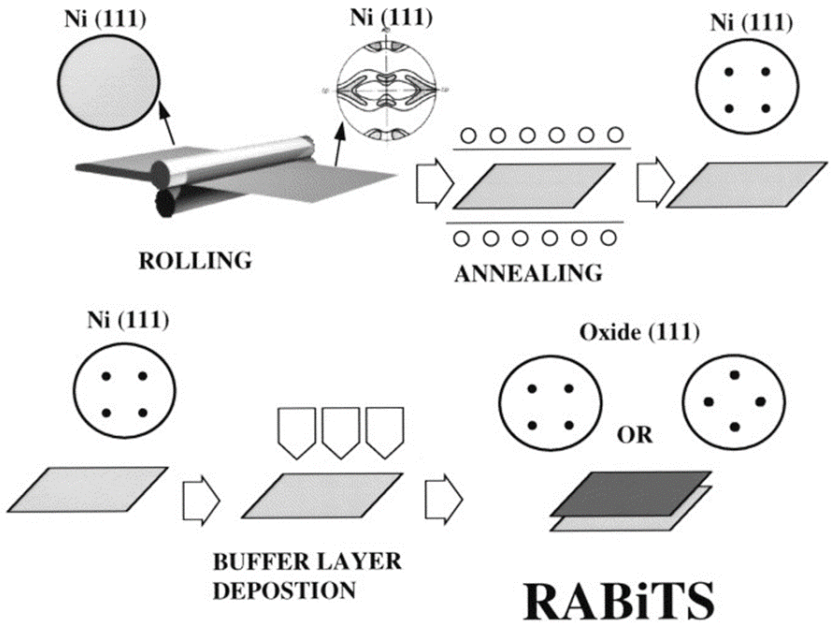

Figure 1.6 Schematic of the RABiTS process [31].

However, there only a few kinds of metals that can be used to realize biaxially-textured tape using the RABiTS technique. Due to the unique cold rolling process, only metals with a face centered cubic (FCC) structure such as Ag, Ni, copper (Cu), and Ni-based alloys can be used [31]. Another drawback is also related to the use of high-purity metals since most candidates cannot provide sufficient tensile strength. Nickel-based alloys may solve this issue [32]; however, the elements in this alloy such as chromium (Cr), tungsten (W), and Cu can influence recrystallization during the RABiTS process.

Besides that, these elements may diffuse to the upper functional layers if an appropriate cap layer is not used. In general, the application of this technique is mainly restricted by the substrate metals, so it cannot be as universal as the IBAD technique for achieving low cost, biaxially-textured functional layers on various flexible substrates for energy applications.

1.3 Buffer structure design for energy applications

1.3.1 Buffer layers architecture with oxide layers

Since the IBAD MgO is the most cost-efficient buffer layer for the HTS application, different cap layers have been demonstrated for the purpose of achieving functional highly-textured $REBa_2Cu_3O_{7-x}$ (REBCO, RE = rare earth) films [29]. For the requirements of large-scale commercial applications, the cap layers should have thermal properties similar to those of the REBCO film and good chemical stability [33]. For the requirements mandated by the fabrication process, a high deposition rate, good surface quality with a smooth surface, and small lattice mismatch with REBCO are more desirable [34].

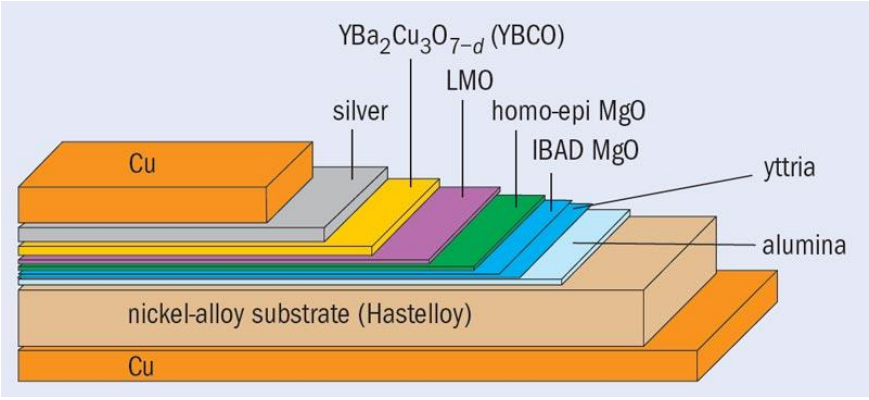

Figure 1.7 Schematic of HTS layer structure on a flexible Hastelloy with IBAD buffer [35].

Many materials have been used for the cap layers, such as $LaMnO_3$ (LMO) [36], [37], [38], (La,Sr)TiO_3 (LSTO) [39], [40], $La_{0.7}Sr_{0.3}MnO_3$ (LSMO) [41], [42], $LaNiO_3$ [43], $SrRuO_3$ (SRO) [29], [38], [44], $SrZrO_3$ (SZO) [45], [46], and CeO_2 [21], [47], [48]. These cubic oxides buffers have excellent chemical stability, small lattice mismatch with REBCO film, and reduce the possible strain-related misorientations in REBCO film. LMO is the most-used cap layer material since it has a broader process window and a high deposition rate using a LaMn target [36].

REBCO tape with LMO/IBAD MgO on Hastelloy has already been demonstrated and commercialized by SuperPower Inc [49]. Figure 1.7 provides a schematic view of the tape structure. The first film directly deposited on the polished Hastelloy (<1 nm roughness) is alumina (Al_2O_3). The alumina (50-70 nm) can be employed in either an amorphous or nanocrystalline form to act as a diffusion barriers to block metal atoms from moving to the top functional layer during the following high-temperature deposition process. A thin (<10 nm) nanocrystalline Y_2O_3 layer is deposited on top of the alumina as the IBAD MgO seed layer. The surface roughness should remain <1 nm after coating these two layers.

Homo-epitaxial MgO deposited on top of the IBAD MgO can preserve the texture of the IBAD layer and improve the texture when a thicker film is applied. Matias found that the in-plane texture spread could improve from 5.5º to 1.6º FWHM when the film thickness was increased from 120 nm to 1.5 μm [50]. The same texture improvement was also observed in our group, but high surface roughness with large MgO grains was also seen, as demonstrated in chapter 6. The top LMO cap layer is the intermediate layer between the REBCO and the MgO. The lattice constant of the cubic MgO is 4.21Å,

which has a 9.26% and 7.60% lattice mismatch with the a, b of orthorhombic REBCO (a=3.82Å, b=3.89Å, and c=11.68Å), respectively. The intermediate perovskite LMO can narrow down the mismatch. The pseudocubic lattice constant of the LMO unit cell is 3.92Å, so the LMO/MgO has a smaller lattice mismatch. The lattice mismatch between REBCO a, b, and LMO are also reduced from 2.65% to 0.86%. Besides that, the thermal expansion coefficient of MgO, LMO, and REBCO are quite close [51]. In conclusion, the LMO/MgO/IBAD MgO is a well-established buffer architecture for the large-scale manufacture of REBCO-coated conductors.

1.3.2 All-electrically conductive buffer architecture

Intermediate nonconductive buffer layers that are located between the top HTS film and bottom metal substrate prevent shunting of overcurrent to the conductive substrate which lead to thermal destruction of the tape. This kind of localized thermal destruction on the HTS tape is of serious consequence during the use of HTS tape in commercial applications at the industrial level, such as the power transmission grid [52]. An optional way to manage an overcurrent occurrence is to use an interlock. However, a better way to manage this type of risk could be within the HTS tape itself if a conductive material is used as a buffer layer.

An all-conductive architecture using conductive buffer layers may also benefit devices with III–V semiconductor functional layers. Multilayer architectures of gallium arsenide (GaAs) solar cells [53], [54], and silicon (Si) transistors [55] have been successfully developed on Hastelloy-based biaxially-textured germanium/ion-beam-assisted deposited magnesium oxide (Ge/IBAD MgO) buffer [56]. However, this

"device layers/oxide buffer/metal tape substrate" architecture has drawbacks in achieving a high-performance device. For example, in the GaAs solar cell device, the nonconductive buffer isolated solar cell functional layers from the metal substrate, which meant that a lateral design was needed for the back contact (Figure 1.8). This lateral design caused higher series resistance and shadowing effects, which could have limited device performance. Additionally, the cost of device fabrication would also be higher because of the extra steps of etching needed to fabricate a lateral back contract. These issues could be overcome if the isolation between the device layer and the metal substrate is eliminated (Figure 1.8 b).

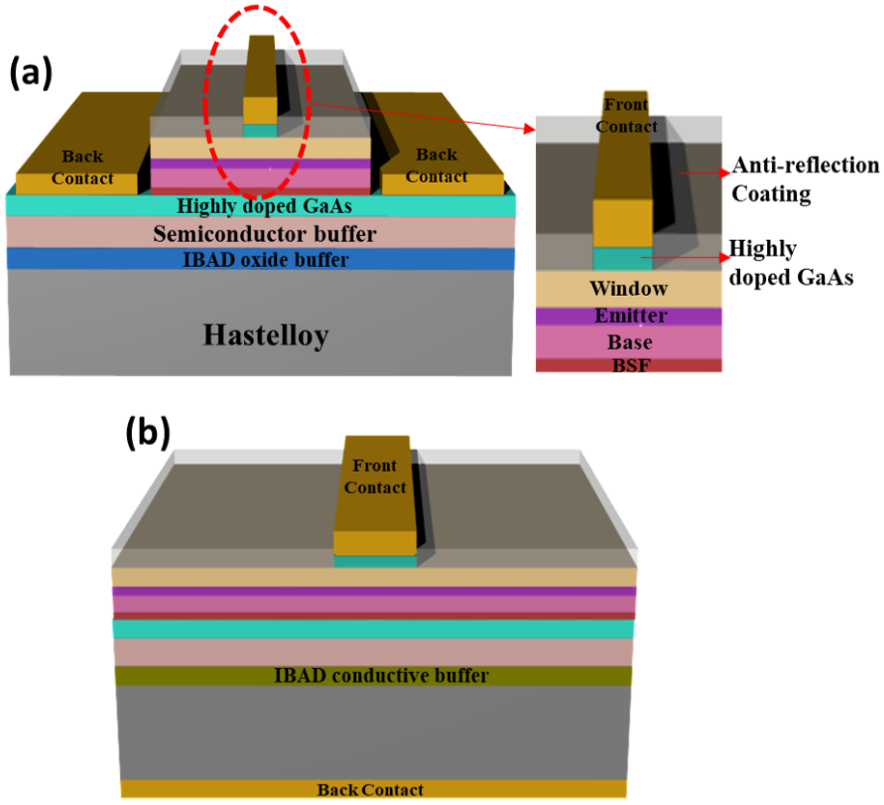

Figure 1.8 Single junction gallium arsenide (GaAs) solar cell on the flexible Hastelloy substrate with (a) ion beam-assisted deposition (IBAD) oxide conductive buffer with both front and back contacts on top; (b) IBAD conductive buffer (simplified structure). Different functional layers are marked with a specific color in both structures.

There are two possible routes of using the metal substrate as the bottom electrode for a back contact: (1) use of biaxially-textured metal tape, such as textured nickel tungsten (NiW) tape with appropriate conductive cap layers or (2) use of conductive materials to replace the IBAD MgO and oxide seed layer on an untextured substrate such as Hastelloy.

Transition metal nitrides, such as titanium nitride (TiN) and niobium nitride (NbN), in the rock-salt-structure family are promising candidates for this study since they are quite similar to MgO with respect to structure. Besides that, most nitrides have excellent electrical conductivity, thermal stability, and high mechanical hardness [57].

TiN is the most common nitride with a structure similar to MgO. Additionally, the TiN thin film can act as a barrier to diffusion of the metallic elements in the substrate and protect the top functional layer [58], [25]. TiN also shows superior stability under humid conditions (compared with MgO) [45]. Many groups have successfully demonstrated IBAD TiN as the biaxially textured buffer layer for HTS coated conductor application [59], [60], [61]. However, the seed layers used for the IBAD TiN growth in these studies, such as Y_2O_3, Si_3N_4, and Al_2O_3, are electrical barriers since none of them are conductive [62], [63].

Hühne et al proposed a way to build an all-conductive buffer for biaxially-textured films using tantalum nickel ($Ta_{0.75}Ni_{0.25}$; TaNi) as the seed layer [45]. TaNi is a metallic material with low resistivity (200 μΩ/cm) and high thermal stability. They demonstrated that the sputtered $Ta_{0.75}Ni_{0.25}$ remained in the amorphous phase on the

electropolished Hastelloy substrate after the homo-epitaxial TiN texture was achieved on top at 700 ºC.

Xia proposed an all-conductive architecture using RABiTS-processed NiW tape [64]. Conductive perovskite strontium ruthenate ($SrRuO_3$/SRO) was used as the cap layer between YBCO and TiN on textured NiW tape. SRO has only a small lattice mismatch with YBCO in addition to low oxidation resistance. They claimed that the resistance of the YBCO/SRO/TiN/NiW structure is three orders of magnitude smaller than the YBCO/CeO_2/YSZ/Y_2O_3/NiW structure (containing cerium oxide and yttria-stabilized zirconia) and that YBCO shows good texture (4.7º for $\Delta\omega$ and 7.5º for $\Delta\phi$) on the SRO/TiN/NiW buffer.

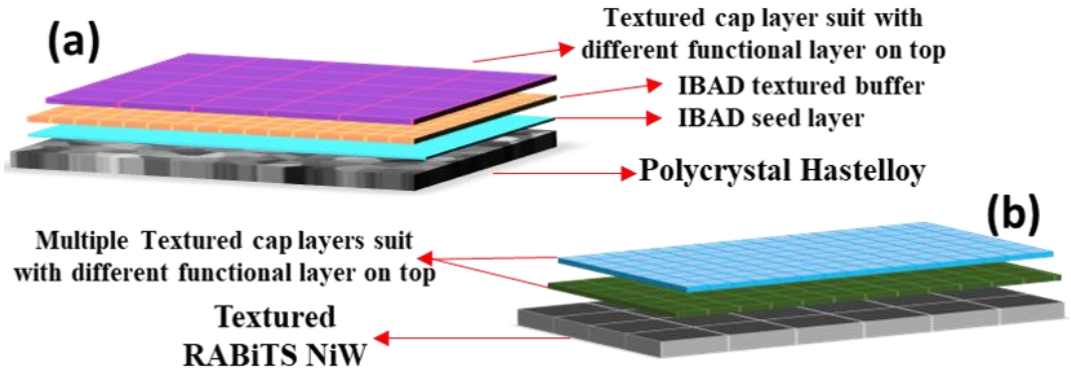

Figure 1.9 Different biaxial texture architectures on (a)Hastelloy and (b) rolling assisted biaxially textured substrate (RABiTS) nickel tungsten (NiW). (a) For Hastelloy-based conductive buffers, the structure containing tantalum nickel (TaNi) could be conductive seed layer in IBADTiN/$Ta_{0.75}Ni_{0.25}$/Hastelloy structure; (b) For the NiW-based conductive buffer, the structure could be conductive perovskite/TiN/NiW as described in the references [65], [66], [67].

In summary, TiN has already been proven to be an ideal candidate for a conductive buffer on both the Hastelloy structure and textured NiW tape (Figure 1.9) when used together with conductive perovskite cap layers such as SrRuO3 or LaNiO3. However, either a textured NiW buffer or conductive seed layer for IBAD TiN is required. A

simpler way is to apply the IBAD TiN layer directly on the Hastelloy structure as both a biaxially-textured layer and diffusion barrier without the seed layer; that process is discussed in chapter 3.

1.3.3 The influence of biaxial texture quality on top functional layers

The single-crystal-like biaxially-textured film that was formed using the IBAD protocol provides an alternative way for achieving an epitaxial film on various types of substrates. However, this single-crystal-like film, which consists of aligned crystalline grains, still cannot fully replace the single crystal wafer in certain respects.

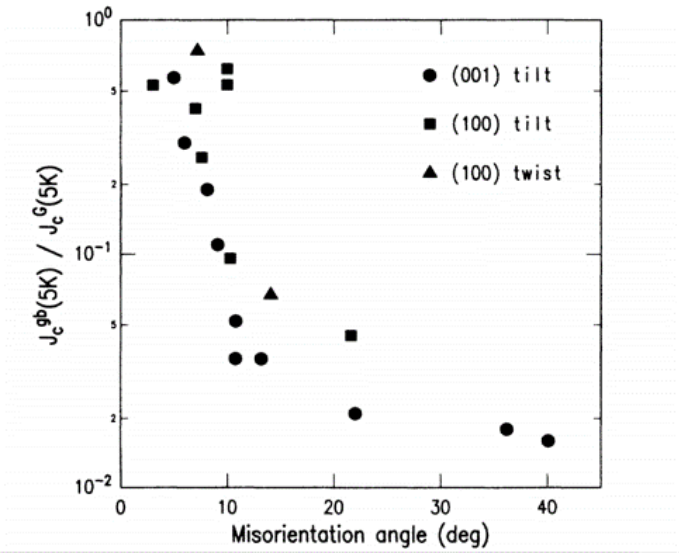

Figure 1.10 Evolution of critical current density ratio (J_c^{gb}/J_c^{g}) as a function of yttrium barium copper oxide (YBCO) grain misorientation angle [68].

In the high-temperature superconductor field, the critical current density (J_c) of the YBCO film is significantly affected by the alignment of YBCO grains [69]. By investigating the relationship between grain misorientation and critical current using bicrystal YBCO, Dimos et al. found that the ratio of the critical current density flowing through the grain boundaries to that flowing within the grains (J_c^{gb}/J_c^{g}) was two orders

of magnitude higher at large misorientation angles (Figure 1.10) [68], [70]. This sharp drop happened when the oriented angle exceeded 5º.

The J_c of polycrystalline YBCO was improved when grown on a biaxially-textured IBAD buffer film [9]. The large-angle grain boundaries were avoided using biaxially-textured buffer MgO, on which YBCO film could be grown with a narrow texture spread [71], [72]. Since the in-plane texture of IBAD MgO-based buffers is about 6º, there is still room to improve the YBCO texture by optimizing the buffer texture for minimizing the texture spread along both the c and a,b axes.

The IBAD method also provided a way to achieve a single-crystal-like semiconductor film on a flexible substrate. Recently, a high-efficiency GaAs solar cell was demonstrated on the IBAD MgO buffered Hastelloy substrate with a single-crystal-like Ge template [53], [73]. Compared with the similar solar cell device on a single-crystal wafer, the efficiency of solar cells on this flexible base was still mainly limited by the absorption and leakage/recombination at the grain boundaries, sidewall, and defects [74]. These can act as potential barriers in solar cell devices and significantly diminish the carrier lifetime by promoting recombination velocity. Besides the methods that can minimize the recombination, such as device passivation, the texture of the functional materials still can be further optimized still by improving the grain alignment in the buffer layer.

Many researchers have tried to improve biaxially-textured films by narrowing the texture spread and reducing the defects/grain boundaries. Gsell proposed a concept to introduce iridium (Ir) to achieve a near single crystal texture epitaxial thin film on IBAD-textured film [75]. A texture <1º in both in-plane and out-of-plane directions for

the Ir (002) oriented film corresponded to a Δω of 1.57º and Δϕ of 4.2º for the MgO layer. To investigate how the texture evolved when Ir was deposited on the oxide buffer, different thicknesses of Ir were deposited on the IBAD YSZ oxide on a Si (001) substrate.

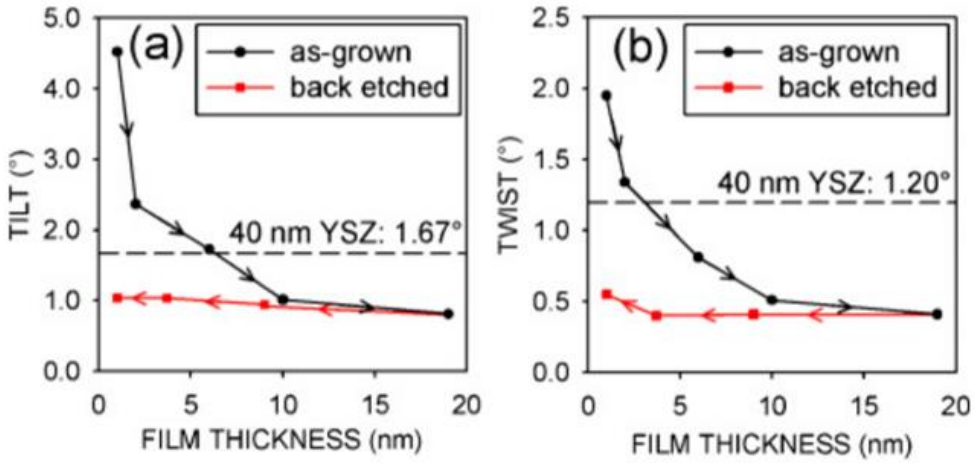

Figure 1.11 Texture evolution (a)Δω (b)Δϕ of iridium (Ir) film on IBAD yttria-stabilized zirconia (YSZ) as a function of Ir film thickness. Both as-grown and back-etched textures are marked with circles and square lines, respectively. The IBAD YSZ substrate texture is also included [75].

As shown in Figure 1.11, tilt and twist (Δω and Δϕ, respectively) dropped significantly when the Ir film became thicker, which indicates that the Ir texture changed dynamically during the growth process. At the very beginning of the deposition process, the Ir grains still followed the high-texture spread of the YSZ buffer. Paradoxically, the Ir metal film texture showed a constant low spread when the film was etched back. The authors indicate that a "massive recrystallization and reorientation of the metal islands" may have happened when the Ir became thicker. The Ir metal grains merged, and an intermediate orientation was adopted on the newly formed grain. This <1º film texture, which is very close to a single crystal film, provides a new route for improving the IBAD buffer texture.

However, Ir is one of the rarest elements on earth [76]; thus, it is impractical to use this element as a buffer material for large-scale manufacturing. Instead, silver (Ag) is a potential candidate to replace Ir for texture improvement purposes. Ag is one of the most stable transition metals and has a face-centered cubic structure. A highly textured Ag growth on IBAD MgO, IBAD TiN, and TiN-coated RABiTS NiW tape has already been demonstrated in previous studies [77]. The intermediate Ag layer was proven to be a promising metal cap layer for textural improvement on the IBAD buffer. This buffer structure on a flexible Hastelloy substrate is an up-and-coming candidate for high-efficiency solar cell devices.

1.4 Flexible non-metallic substrate for HTS application

1.4.1 Background introduction

Commercialized 2G-HTS REBCO on metal tape has been developed by large-scale roll-to-roll manufacturing in recent decades [78]. Related applications include magnetic resonance imaging (MRI), particle accelerators, and high-efficiency power grids [79], [80]. However, state-of-the-art REBCO made by thin-film buffer structures on Hastelloy tape have limited the application and performance of REBCO material.

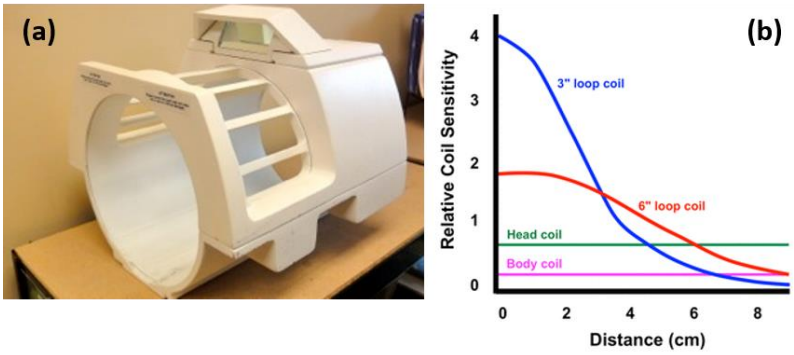

Figure 1.12 (a) Receiver head coil for a commercial MRI system [81]; (b) Signal-to-noise ratio for RF coils of various sizes [82].

Traditional RF receiver coils in commercial MRI are rigid and cumbersome. Each part of the human body needs a unique coil of a specific shape (e.g., Figure 1.12 a) [83]. In addition, the resolution of the MRI image created via these MRI coils cannot meet the requirements of modern medical diagnosis. The low signal-to-noise ratio (SNR) is the main source for the low resolution—there could be two reasons for this. First, the rigid shape of the coil leads to a far distance between the coil and the body parts. The SNR will be low because the SNR is very sensitive to the distance (Figure 1.12 b) [82]. Second, the coil metal could create radio frequency (RF) eddy currents that will lower the SNR [84].

A high SNR is an essential quality for achieving high-resolution MRI. REBCO is an ideal candidate for high SNR receiver coil/antennas in MRI systems [85], [86], [87]. This is attributed to its low surface resistance at 77 K. REBCO extensively used in many applications is based on flexible Hastelloy tape which not applicable in RF coils due to the metal base. Many researchers have developed REBCO films on non-metallic substrates such as sapphire and MgO wafer [87], [88]. However, this is still not the best option because flexibility is sacrificed and the single crystal wafers are very expensive. Thus, REBCO on a flexible, non-metallic substrate remains an important goal.

Next-generation qubits quantum computers also need specific superconducting material. The unique qubit coherence work function relies on a hierarchal temperature system called dilution refrigerator [89], which could progressively lower the temperature from Kelvin to milliKelvin levels to keep the qubits in a coherent state . In this temperature hierarchy structure, multiple signal amplifiers work together in different temperature ranges to bring the signal from millikelvin qubits to user interface

(UI) at room temperature [90]. State-of-the-art qubits signals are still very weak and sensitive to noise at such a low temperature [91], [92]. Researchers are dedicated to improving the computing accuracy of the qubit quantum computer by reducing the noise effect in the structure [93].

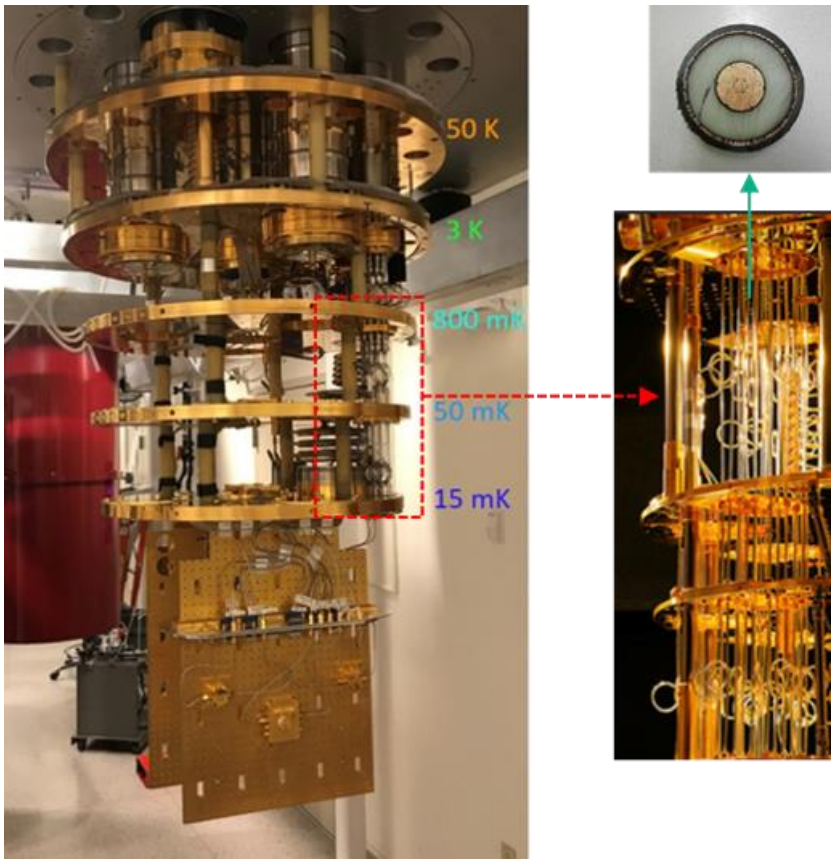

Figure 1.13 (a) Photograph of a dilution refrigerator. Each circular plate works at a progressively lower temperature (adopted from MIT Lincoln Laboratory); (b) coaxial microwave transmission cables in the setup; (c) cross-section of a typical transmission cable [90].

One of the opportunities to reduce the noise is the transmission cable. These cables used between signal amplifiers and qubits need to cause less attenuation of signals transmitted between milliKelvin and Kelvin temperature range. Therefore, the thermal resistance of these cables needs to be high. However, state-of-the-art RF coaxial cables could introduce massive thermal loads and weaken the cooling efficiency of the dilution

refrigerators, even disturbing the coherence of qubits by adding thermal noise. Additionally, the physical size of traditional coaxial cable is not compact enough for dilution refrigerators because the space to reach milliKelvin is very reduced [94]. Micro size superconducting transmission lines on flexible dielectric substrates could solve these issues.

Some researchers have developed a micro transmission line based on a niobium (Nb)/polyimide ribbon substrate to replace the coaxial wires [95]. The superconducting material on polyimide could provide enough mechanical strength and excellent small transmission loss in Kelvin to the milliKelvin range. This transmission line is also compact since the Nb metal is "printed" on a flexible dielectric thin film with a small cross-section area as demonstrated in Figure 1.14.

Nb transmission line is limited by its low T_c (9.3 K) [96], which means that the coaxial wire will still be needed in the higher temperature range. As a high-temperature superconducting material, REBCO can operate over a much broader temperature range of up to 92 K [97]. Hence, the signal loss in the cable could be minimized since most of the transmission lines could be made of REBCO filaments.

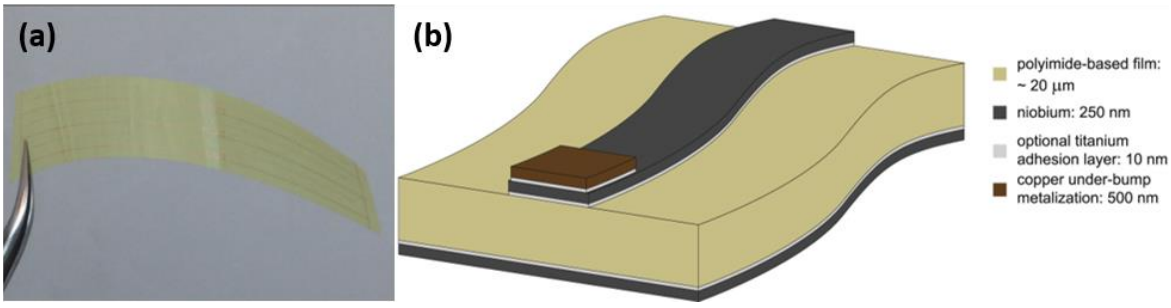

Figure 1.14 (a) thin-film niobium resonator with signal trace (b) Cross-section of the film structure [95].

In general, developing REBCO and related buffer layers on a non-metallic flexible substrate could bring new opportunities in RF and microwave applications. In chapter 4, flexible substrate selection and related buffer layer processes for achieving good quality REBCO films are discussed in detail.

1.4.2 Flexible non-metallic substrate candidates for REBCO thin film

Flexible, robust, dielectric, low thermal expansion coefficient and low-temperature stable substrates are needed for potential RF applications. Two choices include low-cost polyimide (PI) and yttria-stabilized zirconia (YSZ) ribbons.

Polyimide (Kapton)

Polyimide, also known as Kapton, is a ubiquitous polymer that has been widely used in the industry since the 1960s. It is one of the best dielectric materials and is lightweight. Outstanding mechanical properties such as its high Young's modulus, good stress tolerance, low thermal conductivity, wide temperature tolerance (from milliKelvin to 600-700 K), and anti-radiation aging make it a significant material in the aerospace and semiconductor industries [98].

Figure 1.15 (a) (b) Self-standing, flexible 3mol% yttria-stabilized zirconia (YSZ) from ENrG [99]; (c) Polyimide tape (Kapton) from DuPont [100].

Kapton films are commercially available in a variety of shapes and thicknesses and are already used as a flexible substrate for circuit boards [101], batteries [102], and solar cells [103], [104] due to their excellent dielectric properties (Figure 1.15 c) .

Yttria-Stabilized Zirconia (YSZ)

Zirconia (ZrO_2) is a ceramic with ultra-high thermal stability. The monoclinic phase is the most stable crystalline form. At high temperatures, the monoclinic zirconia can transform to the tetragonal or cubic form. The cubic form of zirconia shows more advantages including thermal, mechanical, and electrical properties. The purpose of doping yttria in zirconia is to stabilize the zirconia in cubic form and prevent its transfer to the monoclinic phase. In the doping process, some zirconium ions are replaced by yttrium ions. Usually 2 to 8 mol% yttria are used as a dopant[105].

The flexible YSZ ribbon used in this work and made by ENrG contains 3 mol% yttria zirconia after sintering (Figure 1.15 a, b). This ribbon maintains the excellent thermal and dielectric behavior of zirconia ceramic. The ribbon can maintain good mechanical strength and low thermal deformation at cryogenic temperatures, which makes it better as a substrate for cryogenic applications. The high-density and high mechanical stability of YSZ over a wide temperature range make it an ideal candidate for electronic packaging for harsh environments [106]. It has already been used to fabricate flexible mixed NO_2 sensors [107], [108], high-temperature sensors [109], flexible LED substrates [110], thin-film CdTe PV modules, and solid-state battery packages [111].

Flexible YSZ ribbon is a candidate for self-standing REBCO-coated flexible ribbons. It is compatible with roll-to-roll processing due to its ultra-thin thickness (40

μm) and high mechanical strength [112]. In this case, YSZ could be used as a substrate for the roll-to-roll deposition of high-temperature REBCO and buffer layers. Compared to polyimide, YSZ ribbon offers the benefit of direct deposition of high quality, epitaxial REBCO thin films. In chapter 4, development of YSZ ribbon with an appropriate planarization layer, IBAD MgO and LMO for REBCO growth will be discussed.

1.5 Novel high bandgap semiconductors

Wide bandgap (WBG) semiconductors usually refer to semiconductor materials that have a bandgap larger than 3 eV. Unlike conventional semiconductor materials such as Ge, Si, and group III arsenide or phosphides, WBG semiconductors such as GaN and SiC can offer advantages to electronics and optoelectronics devices since they allow the device function at elevated temperatures, voltages, and frequencies [113]. Owing to these unique properties, devices such as blue light-emitting diodes, ultraviolet (UV) photodetectors, and high-power radio-frequency transistors have been successfully developed and commercialized [114], [115], [116].

Massive data exchange and communication systems have become vital nowadays. Modern military and airspace systems require high-speed datalinks between radar, guided weapons, satellite, and aircraft [117]. In addition, autonomous cars need high-speed communication between sensors, control computers, and real-time network communications [118]. Current state-of-the-art SiC and GaN power electronics may fit these new requirements [118]. However, future massive applications will require highly integrated, cost-effective, and high performance that may not be met using standard technologies.

Ultra-WBG (UWBG) semiconductors such as beta-gallium oxide (β-Ga_2O_3), aluminum nitride(AlN), diamond, and boron nitride (BN) have come into the spotlight in recent years as promising candidates for developing the next-generation high-power and high-frequency power electronics as well as solar-blind UV photodetectors [119]. Among these candidates, β-Ga_2O_3 has attracted increasing attention because of its the ultra-wide bandgap of 4.8eV, high Baliga's figure of merit (FOM), and high thermal stability. Besides that, single-crystal β-Ga_2O_3 wafer can be made by conventional solidification methods such as float zone, Czochralski, and edge-defined film fed growth, which are impossible for the growth of some WBG semiconductors such as SiC, GaN and diamond [120].

1.5.1 Crystal structure of Ga_2O_3

Although considered a very new technology, Ga_2O_3, which is known as a UWBG semiconductor, was first discovered and applied in the 1950s. The varieties of Ga_2O_3 polymorphs were determined by Roy in 1952, and the Al_2O_3-Ga_2O_3-H_2O phase equilibria system was also mapped out [121].

Ga_2O_3 was also used as an insulator on GaAs wafers in the 1970s [122]. Besides that, Ga_2O_3 has been employed as an anti-reflective coating on GaAs since it is transparent [123]. Early-stage research used Ga_2O_3 for chemical sensing [124], catalysis [125], and phosphors/electroluminescent devices [126]. There are five different polymorphs of Ga_2O_3, denoted as α, β, γ, δ, and ε. Table 1.1 summarizes the crystalline properties of different Ga_2O_3 polymorphs [127]. The β phase is the most stable phase of Ga_2O_3 with a monoclinic structure. All other phases can convert to the β phase by

different heat treatments, as demonstrated in figure 1.16. Since other phases require high free energy to form and are unstable at room temperature, the melt growth method is only applicable to the bulk β-Ga_2O_3 because of its ultra-high melt point (1793 ºC) [128].

Table 1.1 Crystalline properties of Ga_2O_3 polymorphs [127]

Polymorph	Lattice parameters (Å)	Refractive index, n	Optical dielectric constant	Volume expansion at 1200 K	Bulk modulus (300 K, GPa)	Comment
α	a, b = 4.98–5.04, c = 13.4–13.6	1.74–1.95	3.03–3.80	0.035	~185	Corundum, rhombohedral structure, space group $R\bar{3}c$, bandgap larger than all other polymorphs (~5.2 eV)
β	a = 12.12–12.34, b = 3.03–3.04, c = 5.80–5.87	1.68–1.89	2.82–3.57	0.024	~150	Monoclinic structure, space group C2/m
γ	a = 8.24–8.30					Defective spinel, cubic structure, space group $Fd\bar{3}m$
δ	a = 9.4–10.0			0.04	160	Possibly bixbyite. Suggested to be a nanocrystalline form of ε-Ga_2O_3
ε	a = 5.06–5.12, b = 8.69–8.79, c = 9.3–9.4	1.6		0.028	160	Orthorhombic structure, space group $Pna2_1$

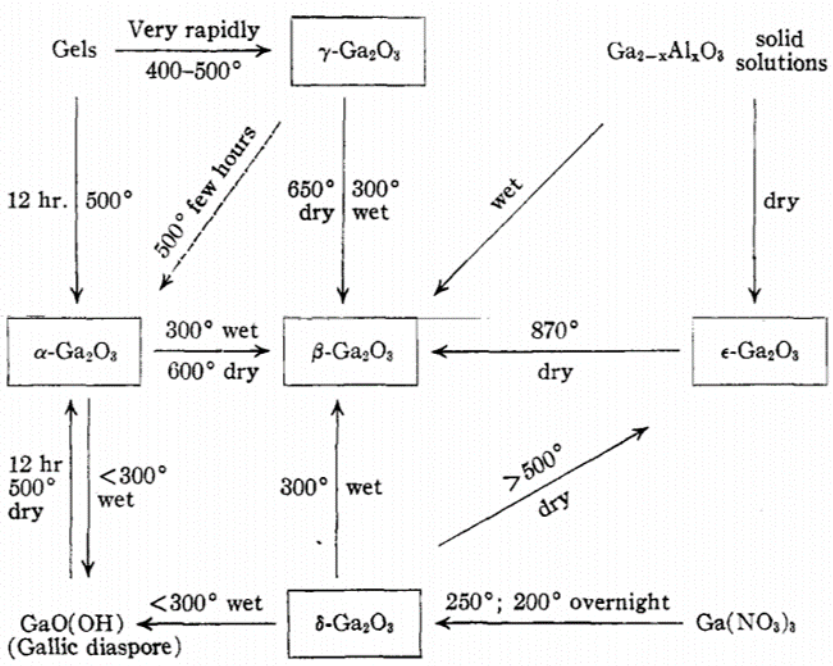

Figure 1.16 Transformation relations between different phases of gallium oxide (Ga_2O_3) and their hydrates [121].

The corundum structure α-Ga_2O_3 may have an even higher bandgap (around 5 eV) than the β phase [129]. Some researchers grew α-Ga_2O_3 on a sapphire (α-Al_2O_3) substrate by exploiting the fact that sapphire shares a similar corundum structure and small lattice mismatch with α-Ga_2O_3 [130]. Different deposition methods have been applied, such as halide vapor phase epitaxy (HVPE) [131] and mist-chemical vapor deposition (mist CVD) [132], and Schottky barrier diodes (SBDs) have already been demonstrated [133]. The ε phase is the second-most stable form of Ga_2O_3 with a similar bandgap as the β phase. This hexagonal Ga_2O_3 shares a similar structure with GaN and SiC [134].

Figure 1.17 (a) provides a 3D view of the β-Ga_2O_3 (ICDD card. 00-043-1012) unit cell structure, which illustrates a monoclinic structure with a C2/m space group. The X, Y, and Z in the figure correspond with the lattice constants a, b, and c, respectively (a=12.21Å, b=3.03Å, and c=5.79Å). The related angles are α=90º, β=103.8º, and γ=90º. There are four formula units of β-Ga_2O_3 in one unit cell with three different O sites and two different Ga sites. The O1 and O2 sites in the unit are 3-fold coordinated, and O3 is 4-fold coordinated. Gallium can also be divided into two kinds crystallographically, including the tetrahedral Ga1 and octahedral Ga2. This unique crystal structure results in β-Ga_2O_3 showing anisotropy on physical properties such as thermal conductivity [135].

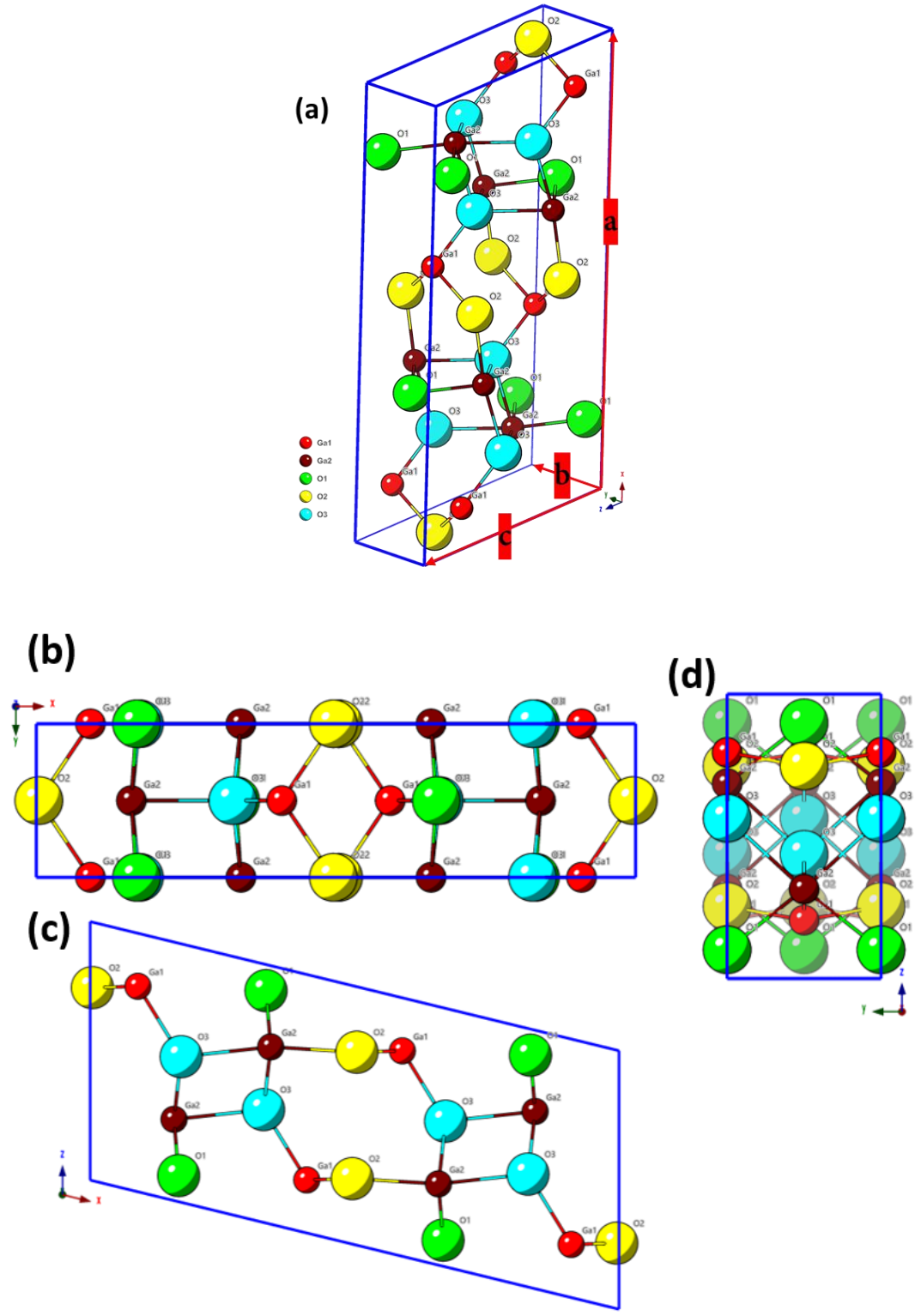

Figure 1.17 Crystal structure of β-Ga_2O_3 (a)3d view; (b) projection of the unit cell along the c direction; (c) projection of the unit cell along the b direction; (d) projection of the unit cell along the a direction.

1.5.2 Physical Properties of β-Ga_2O_3

The ultra-high bandgap is the most attractive feature of β-Ga_2O_3. The physical properties of Si, WBG semiconductors, and diamond are compared with β-Ga_2O_3 in table 1.2. The 4.9-eV bandgap endows the β-Ga_2O_3 with many special abilities. A β-Ga_2O_3-based photodetector can exclusively respond to light of wavelengths shorter than 280 nm [136], [137]. This indicates a deep UV coverage range and that it is solar-blind. Besides that, the next generation of high-frequency and high-power devices require that semiconductors have high breakdown fields, large bandgaps and high electron mobility, which align with β-Ga_2O_3 when appropriate doping is employed [138].

Table 1.2 Physical properties of β-Ga_2O_3 and some regular semiconductors. Few common figure-of-merits also listed [127].

Materials parameters	Si	GaAs	4H-SiC	GaN	Diamond	β-Ga_2O_3	Comments
Bandgap, E_g (eV)	1.1	1.43	3.25	3.4	5.5	4.85	Bandgap of Ga_2O_3 reported in range 4.6–4.9 eV
Dielectric constant, ε	11.8	12.9	9.7	9	5.5	10	
Breakdown field, E_C (MV/cm)	0.3	0.4	2.5	3.3	10	8	Experimental values for Ga_2O_3 have reached ~0.5 times the theoretical maximum
Electron mobility, μ (cm^2/Vs)	1480	8400	1000	1250	2000	300	
Saturation velocity, v_s (10^7 cm/s)	1	1.2	2	2.5	1	1.8-2	1.8 ⟨0 0 1⟩ and ⟨0 1 0⟩, 2.0 ⟨0 1 0⟩
Thermal conductivity λ (W/cm K)	1.5	0.5	4.9	2.3	20	0.1–0.3	0.13 ⟨1 0 0⟩, 0.23 ⟨0 1 0⟩
Figures of merit relative to Si							
Johnson = $E_c^2 \cdot V_s^2/4\pi^2$	1	1.8	278	1089	1110	2844	Power-frequency capability
Baliga = $\varepsilon \cdot \mu \cdot E_c^3$	1	14.7	317	846	24 660	3214	Specific on-resistance in (vertical) drift region
Combined = $\lambda \cdot \varepsilon \cdot \mu \cdot V_s \cdot E_c^2$	1	3.7	248.6	353.8	9331	37	Combined power/frequency/voltage
Baliga high frequency = $\mu \cdot E_c^2$	1	10.1	46.3	100.8	1501	142.2	Measure of switching losses
Keyes = $\lambda \cdot [(c \cdot V_s)/(4\pi \cdot \varepsilon)]^{1/2}$	1	0.3	3.6	1.8	41.5	0.2	Thermal capability for power density/speed
Huang HCAFOM, $\varepsilon\mu^{0.5} E_C^2$	1	5	48	85	619	279	Huang chip area manufacturing FOM

The breakdown field, also called the dielectric strength, is an essential index to evaluate the capabilities of a semiconductor for power device application. Basically, when an electrical field is applied to a semiconductor with a potential barrier, a depletion region forms and increases with increasing voltage. When the applied voltage reaches a certain critical point, an avalanche breakdown can occur, since the free electrons are sufficient to cause the chain reaction. This critical point depends on material properties

and quality of the material. The unit is usually given as volts per centimeter, derived from the impact ionization coefficient, and which indicates the difficulty of initiating the avalanche [139]. The breakdown field of β-Ga_2O_3 and diamond are each higher than 8 MV/cm, since they behave more like insulators when compared with Si and GaAs. This ultra-high dielectric strength ensures that a β-Ga_2O_3 power device can work at an ultra-high voltage.

Another method to evaluate the performance of a power device is the figure of merit (FOM). Different FOM have different evaluation standards [140]. For example, the Baliga's figure of merit (BFOM) is to estimate the conduction losses in the low-frequency unipolar transistor:

$$BFOM = \varepsilon \mu E_c^3$$

where ε is the dielectric constant, μ is the electron mobility, and E_c is the breakdown field.

Table 1.2 list a few kinds of FOM values. All the numbers in the chart were normalized to Si for comparison purposes. The high breakdown field benefits the FOM of β-Ga_2O_3. The BFOM of β-Ga_2O_3 is almost four times higher than GaN. Owing to its high saturation velocity, Johnson's figure of merit (JFOM) of β-Ga_2O_3 is the highest among these semiconductors, which makes this material good for high power-frequency devices. The Huang's chip area manufacturing figure of merit (HCAFOM) provides information about the manufacturability and cost of the semiconductor device. This number is still much higher compared to 4HSiC and GaN since β-Ga_2O_3 is still in the early research stage; however, this value may drop with the increased feasibility of bulk β-Ga_2O_3 melt growth [141].

Also, the thermal conductivity of β-Ga_2O_3 is extremely low, which can cause severe self-heating if it is used for power device applications [142]. Since most of the power is dissipated in the channel of a high-power device, the resulting localized joule heating could significantly increase the channel temperature and cause degradation of device performance and even device breakdown [143].

Device-level thermal management of β-Ga_2O_3-based devices is one of the open issues in Ga_2O_3 research. Since GaN electronic devices have been systematically studied for many years, researchers have tried to transfer efficient thermal management of β-Ga_2O_3 from previous GaN work. Both active and passive cooling solutions such as air-jet impingement [144], flip-chip heterointegration [145], device-level microchannel cooling [146], and several bottom-side cooling methods [147], [148] have been investigated for thermal management in Ga_2O_3 devices. Researchers have also proposed a few ways to transfer the device layer to a high thermal conductive substrate, such as diamond, Cu, and SiC [149], [150]. However, these methods increase the difficulty and complexity of device manufacturing and also hardly fit with future scale-up processes.

1.5.3 Motivation

Although β-Ga_2O_3 has many advantages as the material candidate for next-generation electronics, there are only a few reports of flexible β-Ga_2O_3 devices, such as a deep UV detector on flexible polyimide [151] and muscovite mica [152]. The possibilities and feasibilities of realizing β-Ga_2O_3 devices on flexible substrates have not been fully investigated and exploited yet, although the flexibility requirements demanded in future applications such as biomedical detection sensors of skin disease,

military communication, and astro-surveillance exist. Besides that, flexibility can expand the applications of power devices to higher integrated electronics. In chapter 6, heteroepitaxial β-Ga_2O_3 growth on flexible single-crystal-like IBAD MgO buffered Hastelloy by roll-to-roll RF sputter deposition are discussed.

1.6 Outline

This dissertation aims to realize different single-crystalline-like buffer architectures on both Hastelloy and non-metallic substrates, using an IBAD system, for different applications.

Chapter 3 discusses a simplified IBAD TiN buffer layer that is directly deposited on Hastelloy. This conductive buffer structure can provide benefits in both superconductor and semiconductor applications. During the IBAD process, surface ion-bombardment by an assist beam is the critical step to realize biaxially textured TiN directly on polished Hastelloy.

Chapter 4 discusses the method used to produce a REBCO LMO/MgO buffer structure on a non-metallic flexible substrate. HTS on non-metallic flexible substrate shows a very promising application for improving the signal to noise ratio (SNR) of state-of-art biomedical Magnetic resonance imaging (MRI) system or high SNR transmission lines in the cryogenic quantum computing system.

Chapter 5 is on optimization of the texture of conventional LMO/homoepitaxial MgO/IBAD MgO on Hastelloy tape by introducing a silver (Ag) and TiN intermediate layer. Different buffer architecture designs with Ag and TiN will be discussed.

Chapter 6 proposes a way to produce ultra-wide-bandgap beta-gallium oxide (β-Ga_2O_3) on IBAD MgO-capped flexible Hastelloy tape. This is the first time growth of biaxially-textured β-Ga_2O_3 on low-cost, flexible, highly thermally conductive Hastelloy using a roll-to-roll PVD process has been demonstrated.

CHAPTER 2 METHODS OF MATERIAL FABRICATION AND CHARACTERIZATION

2.1 Systems for thin film deposition

2.1.1 System for biaxially textured IBAD layer growth

Roll-to- roll IBAD system

All biaxially-textured templates fabricated in this dissertation were processed by a roll-to-roll IBAD system. The configuration of the IBAD system is exhibited in Figure 2.1. Each subsystem will be discussed in detail.

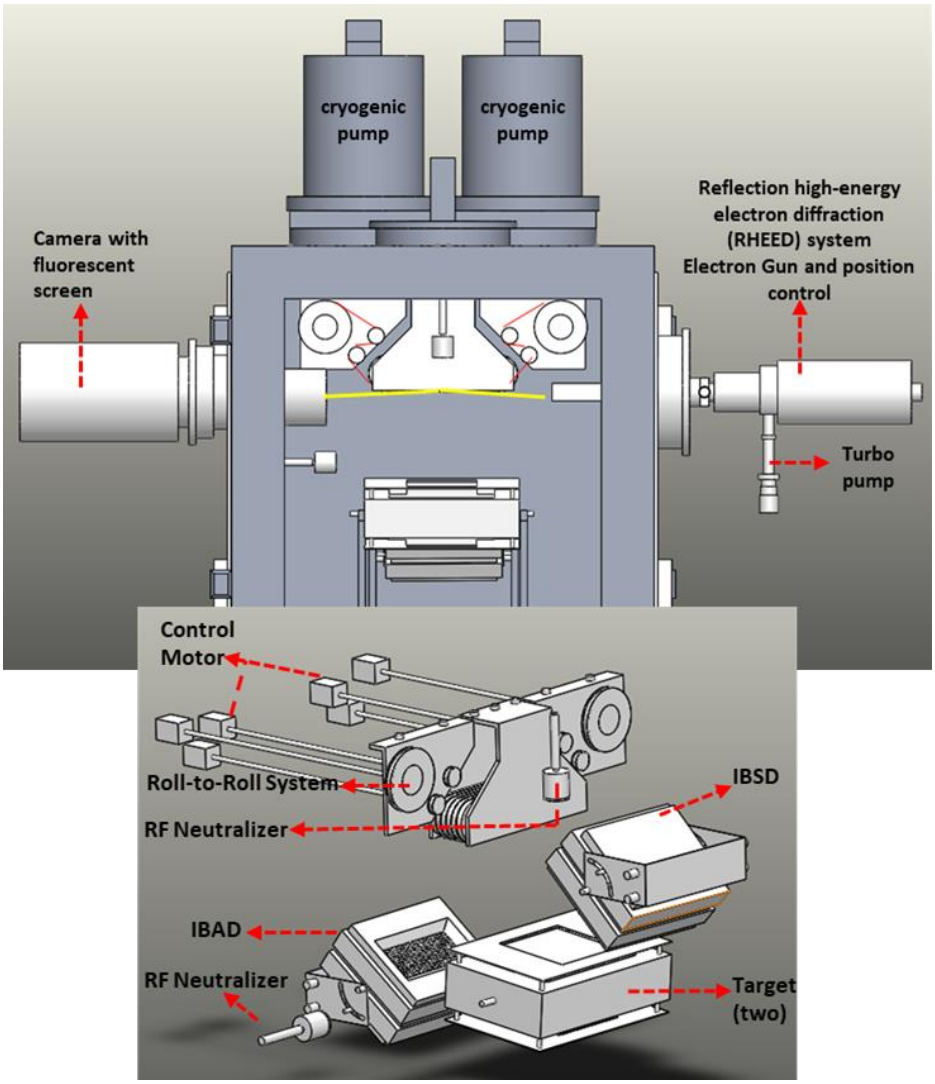

Figure 2.1 Schematic of IBAD system, front view and 3D view of selected parts.

In-situ monitor system: A reflection high energy electron diffraction (RHEED) system (STAIB Instruments, EK-35-R) integrated with the chamber was used for monitoring the evolution of IBAD film texture during the deposition process. Several components are included in this system: a high voltage electron gun with a point-shifting control system, a phosphor screen to reveal the electron diffraction pattern, a camera, and a real-time display program with an image recording function. A shutter is present in front of the phosphor screen to prevent unintentional damage to screen's coating. The electron beam position can be controlled by a beam navigator program during the whole process. During the monitor process, the energy level of the electron gun is usually maintained between 20 and 21 keV.

Ion source: Two 6 cm × 22 cm ion sources (Kaufman-type broad-beam sources) with a maximum 1500 V accelerating voltage and 100 mA beam current were used for the sputter and assist beams. High purity (99.99%) argon (Ar) was used as the gas source. Grids inside the ion source were separated by ceramic insulators to extract the Ar ion beam. There are also two neutralizers, one for each ion source. The neutralizers can provide electrons from a RF source and balance the Ar ions of the beam as well as prevent the charge build-up on the target and susceptor. The position of the assist beam its angle with the normal direction can be adjusted.

Vacuum System: The vacuum system can be divided into two parts. The first is a pumping system, and the second is a pressure monitor system. The main chamber uses a mechanical pump to reach a low vacuum (5×10^{-2} Torr) and cryogenic pumps to reach a high vacuum ($<10^{-5}$ Torr). The cryogenic pump temperature is usually maintained below 10 K by a helium compressor. The RHEED system has an individual vacuum

system that can be isolated from the main chamber when idling, by a manual valve. This vacuum system consists of a turbopump and a dry vacuum pump. The vacuum level is maintained around 10^{-6} Torr. The chamber and RHEED system have separate high vacuum convectron ion gauges to monitor the vacuum level.

Gas flow system: The Ar and reaction gas flow inside the chamber is controlled by two groups of mass flow controllers (MFC). The first MFC group services the Ar, which provides separate flow to the two ion sources and corresponding neutralizers. The second MFC group services the reaction gases such as O_2 and N_2 which are directed to the target side and susceptor.

Targets assembly: Two 40 cm × 30 cm target materials are mounted on either side of a target assembly, held with Cu plates. Both targets are surrounded by a graphite plate for better thermal conductivity. Since two films are grown in a typical IBAD process, the target can be flipped over after the first film is deposited. The flip move is controlled by a step motor and two proximity switches.

Roll-to-Roll system: A substrate is mounted between the delivery and take-up spool of a roll-to-roll system. Torque and stepper motors control the tape tension and tape motion, respectively. The motion of the tape is controlled by a Matlab-controlled encoder. The whole tape motion system is covered by shields during the deposition to prevent contamination.

Cooling system: A cooling system with a chiller provides water cooling to the ion sources, target, susceptor, and cryogenic pump helium compressor. Each subloop has a flow meter for flow monitoring purposes.

Control system: An integrated programmable logic controller (PLC) control system is used to control all the vacuum valves in the system with built-in interlocks. A metal shutter between the target and susceptor is used to control the start and end of the deposition process.

2.1.2 System for epitaxial buffer layers growth

Two magnetron sputtering systems were mainly used for thin-film buffer layers fabrication in this dissertation. The first one used a roll-to-roll dual-chamber magnetron sputter deposition to grow the MgO and LMO thin films. The second was a co-sputtering system with a rotational sample stage for an Ag, TiN growth process.

Roll-to-roll dual-chamber magnetron sputter system

This system was used to grow the homoepitaxial MgO film and the LMO film as the REBCO cap layers on the flexible IBAD buffer. The details of the system are presented below.

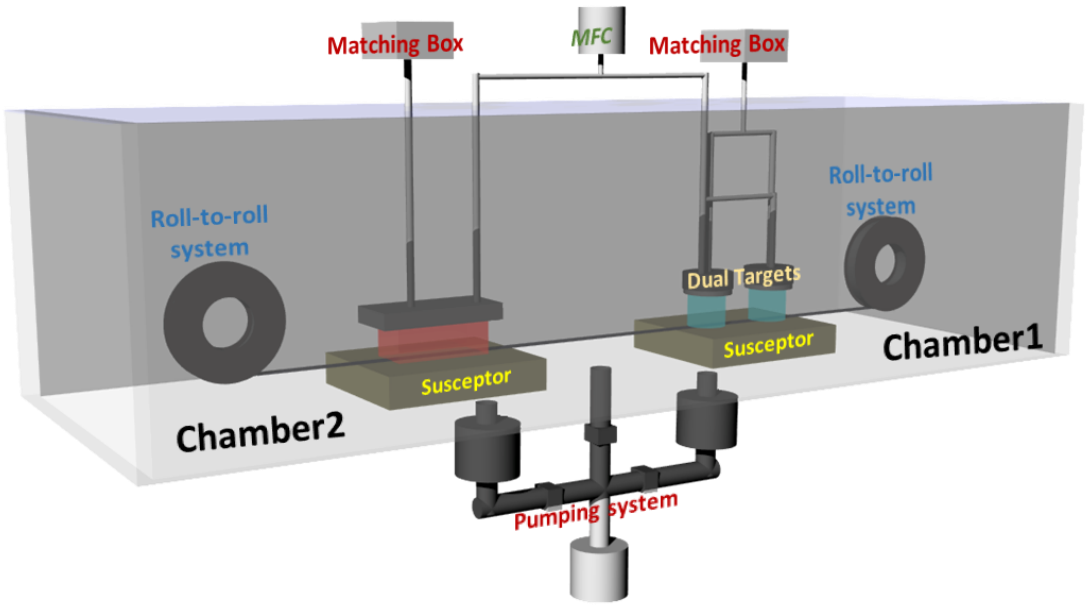

Figure 2.2 Schematic of the roll-to-roll dual-chamber magnetron sputtering system.

Sputter system in chamber 1: The dual-target assembly system in chamber one is used for the MgO sputter deposition. This system uses a mid-frequency (40kH- 300kHz) sputtering system with two magnetron cathodes. Two identical magnesium targets were used along with O_2 supply during the reactive sputtering process. Up to 2000-W MF power can be delivered in this system for a high-speed, high-rate MgO deposition process on flexible tape. Since the reactive O_2 partial pressure could significantly influence the deposition rate, an oxygen (lambda) sensor was used to provide real-time O_2 partial pressure feedback to the MFC for O_2 flow control. The normal O_2 partial pressure with 100 sccm Ar flow during the MgO deposition is approximately 1.5E-4 mbar. Higher O_2 flow should be avoided to prevent target poisoning.

Sputter system in chamber 2: The sputtering system in chamber 2 is equipped with a LaMn alloy target for the LMO deposition process. The alloy target can endure a high deposition rate during the process. A maximum 1500W radio frequency (RF) power supply and corresponding matching box (RF at 13.56 MHz) are used. The Ar and O_2 flow during the LMO deposition is controlled by a multi-channel gas flow controller and related MFCs.

Vacuum system: The system base pressure can reach 5×10^{-6} Torr using two turbopumps and a corresponding mechanical pump. The turbopump can begin to operate when the chamber pressure reaches 5×10^{-2} Torr. During the deposition process, the chamber pressure is usually maintained at 3×10^{-2} Torr with a 100sccm Ar supply.

Roll-to-roll system: Similar to the IBAD system, the deposition time and film thickness is controlled by the tape speed. The roll-to-toll system can provide tape tension and control the tape speed and moving length during the deposition.

Heating system: Each chamber has an individual heating stage. The heating system contains five K-type thermocouples, twelve halogen heating lamps, and a cooling channel. The cooling channel is covered with gold to enhance heat reflection. A 20 cm × 5 cm susceptor stays on top of the cooling channel/lamps to transfer heat to the samples.

Cooling system: A chiller provides cooling water to the heating, sputtering, and turbo systems.

Co-sputtering system

The co-sputter system is an RF sputter system with the capability of depositing several materials simultaneously or sequentially. This system was used to process the TiN and Ag thin films described in this dissertation. As illustrated in figure 2.3, four different target positions with corresponding magnetrons can be divided into two groups, and each group has an individual RF power supply and matching box. The height of the target assembly and the sputtering angle are adjustable. In this case, a multi-layer structure by different sputter sources can be processed continuously without unloading the sample during the process.

The sample is loaded into the chamber through a load lock, so the main chamber does not need to be vented during the sample loading/unloading process. Also, the compact load lock has an exclusive turbopump, so the loading/pumping process can be very quick. The main chamber also has a separate turbo/mechanical pump system to maintain the chamber base pressure at 3.0×10^{-7} Torr. The sample is mounted on the heater susceptor and is rotated during the deposition process. A shutter is used to control

the start/end of the process. The thickness of the film is monitored by a quartz thickness monitor.

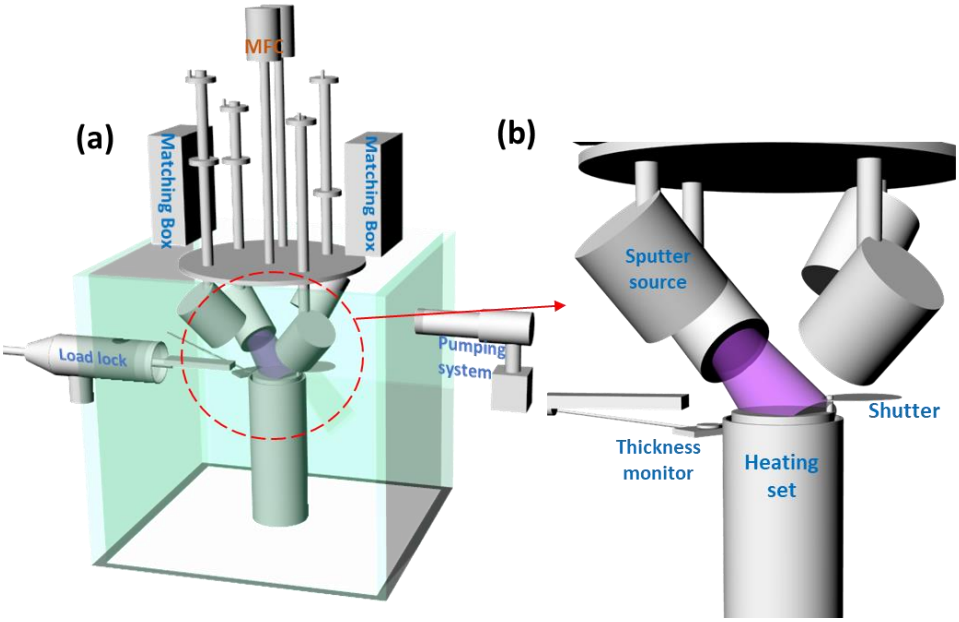

Figure 2.3 Schematic of co-sputtering system

2.2 Methods of materials characterization

IBAD layers and different cap layers deposited on top of the IBAD film were analyzed by different methods. Besides the in situ RHEED system introduced before, X-ray diffraction (XRD) was used for crystallographic analysis. The surface morphology of the film was examined using a scanning electron microscope (SEM) and atomic force microscope (AFM). The cross-section of the sample was studied using transmission electron microscopy (TEM) to examine the structural quality of the different thin films in the architecture.

Three different XRD systems were used for different purposes. A Rigaku Smartlab system was used for θ-2θ scan in Bragg-Brentano (BB) continuous mode and rocking curve measurements. Before the measurement, the sample was aligned in an automatic

mode with a 5mm slit. The scan range is 20º to 75º for the Hastelloy-based sample. The step width was set to 0.05º and 10º/min as the speed/duration time. The rocking curve scan range is decided by the peak position, and 0.05 º/step with a 5º/min scan resolution was applied. The full-width-half-maximum (FWHM) ($\Delta\omega$) of the targeted peak can be collected from the rocking curve scan.

A Bruker D8 system was used to conduct a (-180º to 180º) Phi scan of the thin film at different chi (χ) angles. 0.01 º/step with 1 s/step was selected to ensure the scan accuracy. The final FWHM ($\Delta\phi$) of each peak could be calculated from the corresponding Leptops 7 XRD analysis program.

A Bruker D8 Discover General Area Detector Diffraction System (GADDS) with a two dimensional (2D) detector was used for the θ-2θ scan and pole figure measurement. A laser/camera system was used for sample alignment before the measurement. The rocking curve mode was used to collect the diffraction pattern (frame). Each frame was scanned for 240 s at a specified theta angle in 18º increments. In the pole figure mode, phi scan type was selected with a 7 s/step scan speed. In total, 720 steps were performed for a 360º scan. The final pole figure image can be plotted by integrating all the frames with a selected 2-theta and χ range. All the diffraction patterns can be processed using the Bruker DIFFRAC.EVA program and corresponding texture information ($\Delta\omega$ and $\Delta\phi$) can be obtained.

LEO 1525 SEM system was used to check the surface morphology. Another SEM system (JEOL JSM-6330F) equipped with energy-dispersive X-ray spectroscopy (EDS) system was used for surface elemental analysis. Each area is scanned for 50 seconds with a 15kV beam, and the working distance is typically set to 15 mm.

An Oxford Instrument MFP-3D Origin+ AFM system was used to examine the surface morphology. The measurement was performed in AC air topography mode with HQ:NSC15/Al BS AFM tip from MikoMasch (325 kHz tapping frequency). The scan rate was set to 1 Hz with 512 × 512 pixels per image. The final image and roughness data were processed by the Gwyddion program.

A FEI-235 focus ion beam (FIB) system was used to prepare the TEM cross-section samples. Ion milling was done using gallium ions at different beam current levels. The TEM images were collected by a JEOL JEM-2010 system, and the images were processed by the ImageJ program.

CHAPTER 3 SINGLE CRYSTALLINE-LIKE IBAD TIN CONDUCTIVE BUFFER LAYER DIRECTLY ON METAL SUBSTRATE

As discussed in session 1.3, buffer structures consisting of nonconductive oxides could limit the functionality of the top functional layers. TiN has been reported as a promising material for developing conductive buffer layer to replace oxides because of its good electrical conductivity and high thermal stability. In this chapter, development of biaxially-textured IBAD TiN on polished Hastelloy by a continuous roll-to-roll IBAD process is discussed.

3.1 Development of IBAD TiN on Hastelloy structures with different pre-etching times

The electro-polished Hastelloy C-276 (EPH) structure was used as the substrate. The electropolishing process can assure a substrate surface roughness <1 nm (root mean square [RMS]), which is a prerequisite for IBAD biaxial texture growth. All EPH substrate segments (12 mm wide × 50 μm thickness) were cleaned ultrasonically before IBAD. Ultra-high purity (99.999%) argon (Ar) and N_2 (99.999%) were used as the carrier and reactive gases respectively in the IBAD process. A TiN target (40 cm × 30 cm) fixed with a water-cooled copper plate was used as the sputter source. The angle between the assist beam and the substrate was normally maintained at 45º. Details of the IBAD system follow the description in chapter 1. An in situ reflection high-energy electron diffraction (RHEED) system was used to monitor the texture evolution of TiN during the deposition process.

Figure 3.1 shows the real-time RHEED pattern of the EPH surface. No prominent peaks or polycrystalline rings were observed on EPH before the deposition (Figure 3.1

a). Both sputter and assist beams were used in the next IBAD step; however, only-random oriented diffraction spots and rings slowly emerged (Figure 3.1 c).

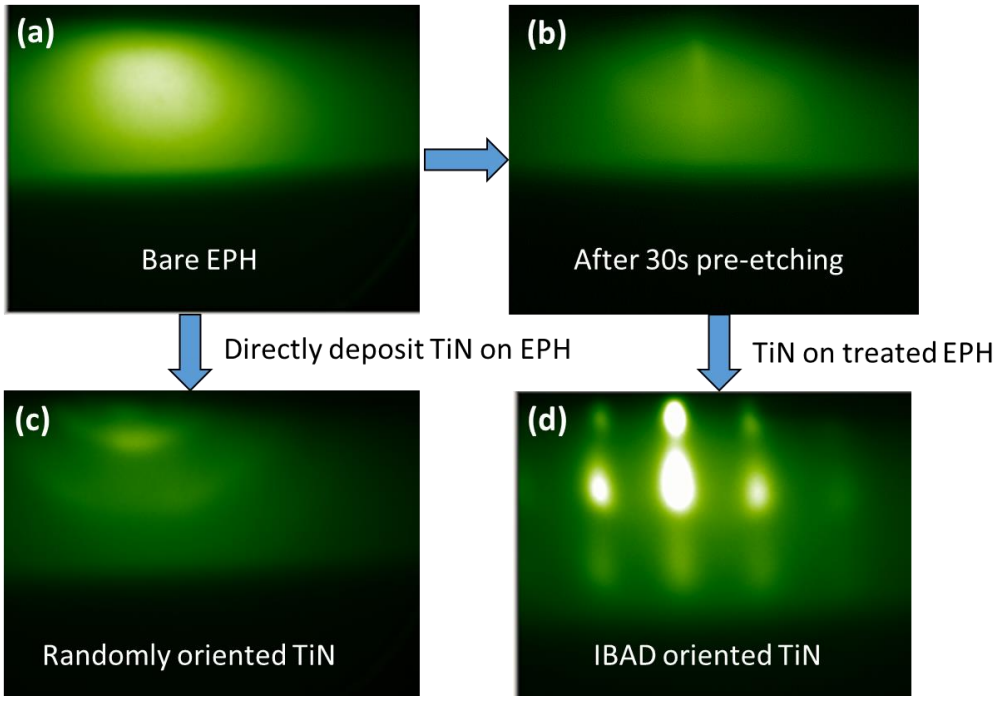

Figure 3.1 Reflection high-energy electron diffraction (RHEED) patterns for (a) bare electro-polished Hastelloy structure (EPH), (b) 30 s pre-etched EPH by assist beam, (c) randomly oriented titanium nickel (TiN) on bare EPH, and (d) biaxially-textured IBAD TiN on pre-etched EPH.

The same IBAD process was repeated on the EPH with an extra step before the deposition consisting of bombardment of the sample surface with the assist ion beam for 30 seconds. The result was quite different and showed a sharp electron diffraction pattern of cubic structure TiN (Figure 3.1 d). The surface bombardment before the IBAD process could create a surface structure to benefit nucleation of biaxially-textured TiN. Improved adatom adhesion and surface energy level altered by ion beam could be possible reasons, but the detailed principle is not clear yet (Figure 3.1 b).

To investigate the effect of ion beam pre-etching on the EPH surface, samples with different ion bombardment times were prepared by following the same pre-cleaning procedures. IBAD TiN was deposited on these samples with identical beam settings

with a constant tape moving speed. The detailed steps and parameters are given in Table 3.1. A thick homoepitaxial TiN was deposited on top of all samples at 700 ºC by radio frequency (RF) magnetron sputtering to preserve the texture for the purpose of performing X-ray diffraction (XRD) analysis. All XRD measurements were performed with a Bruker D8 Discover General Area Detector Diffraction System (GADDS). The EPH surface morphology and roughness were also checked by atomic force microscopy (AFM) after the pre-etching process.

Table 3.1 Growth conditions for IBAD TiN with different EPH surface ion etching times.

	N_2 flow	Sputter Beam (IBSD)	Assist Beam (IBAD)	Time Duration
Surface Pre-etching	No	None	800V, 80mA	3s to 420s
TiN	Yes	950V, 240mA	1000V, 40mA	120s

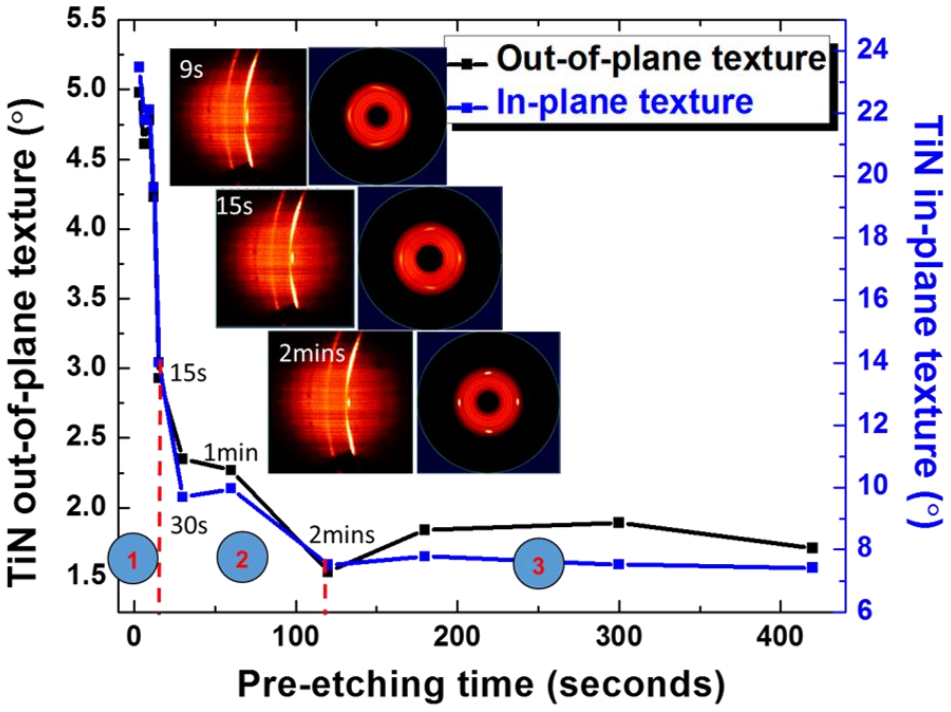

Figure 3.2 Biaxial TiN film texture as a function of ion pre-etching time.

Figure 3.2 shows the evolution of the TiN biaxial texture as a function of surface pre-etching time. Both out-of- and in-plane textures show remarkable improvements with longer surface pre-etching. For a better understanding, the texture evolution in Figure 3.2 is divided into three zones. The first zone includes EPH samples with 0 to 15 sec pre-etching time. In this zone, the TiN texture showed a sharp improvement, the $\Delta\omega$ value decreased from 5.0º to 2.8º, and the $\Delta\phi$ value decreased from 24.0º to 14.0º. GADDS diffraction patterns and TiN (220) pole figures of the 9 and 15 s pre-etched samples, are also shown in the figure. The TiN (200) peak narrowed in the χ direction indicating a full-width-at-half-maximum (FWHM) improvement. The four-fold symmetry peaks in the (220) pole figure also become more apparent. This improvement may be attributed to surface cleaning and the energy change caused by the ion bombardment, which can modify the surface chemistry by removing foreign particles or local terminal oxides.

The texture improvement became moderate in zone 2, and the $\Delta\omega$ and $\Delta\phi$ values dropped 1.2º and 6.5º, respectively. The EPH surface was treated at different pre-etching times ranging from 15 to 120 s in this zone. A distinct and sharp TiN (200) peak was observed in the GADDS diffraction patterns, and four distinct and sharp (220) symmetry peaks were also observed in the pole figure of the 120 s pre-etched sample. This evidence suggests that the good biaxial textured IBAD TiN (1.6º of $\Delta\omega$, 7.5º of $\Delta\phi$) can be achieved directly on the EPH without adding any foreign seed layer. In zone 3, in which all EPH samples were pre-treated with at least 120 s ion bombardment, stabilization of the texture tended to occur, and no significant texture changes were observed. The final TiN texture stabilized at $\Delta\omega$ (1.5º–2.0º) and $\Delta\phi$ (7º–8º).

The surface morphologies of different EPH samples after the pre-etching process are shown in Figure 3.3 with corresponding roughness information listed in Figure 3.4. At the beginning of surface ion bombardment, particles were still observed (3 s pre-etching EPH). The surface morphology of the sample pre-etched for 30 s became smooth, and foreign particles were removed. At the early stage of surface bombardment, the ion beam removed particles on the EPH and then started to modify the EPH surface, which could benefit TiN nucleation. This dynamic process also coincides with fluctuation of the roughness of the 0 to 30 s ion bombarded samples in Figure 3.4. In zone 3 (figure 3.3), all three surface morphologies were similar indicating that the surface condition became stable and correlates with the stabilized IBAD TiN texture after the 30 s ion bombardment (Figure 3.2, zone 3).

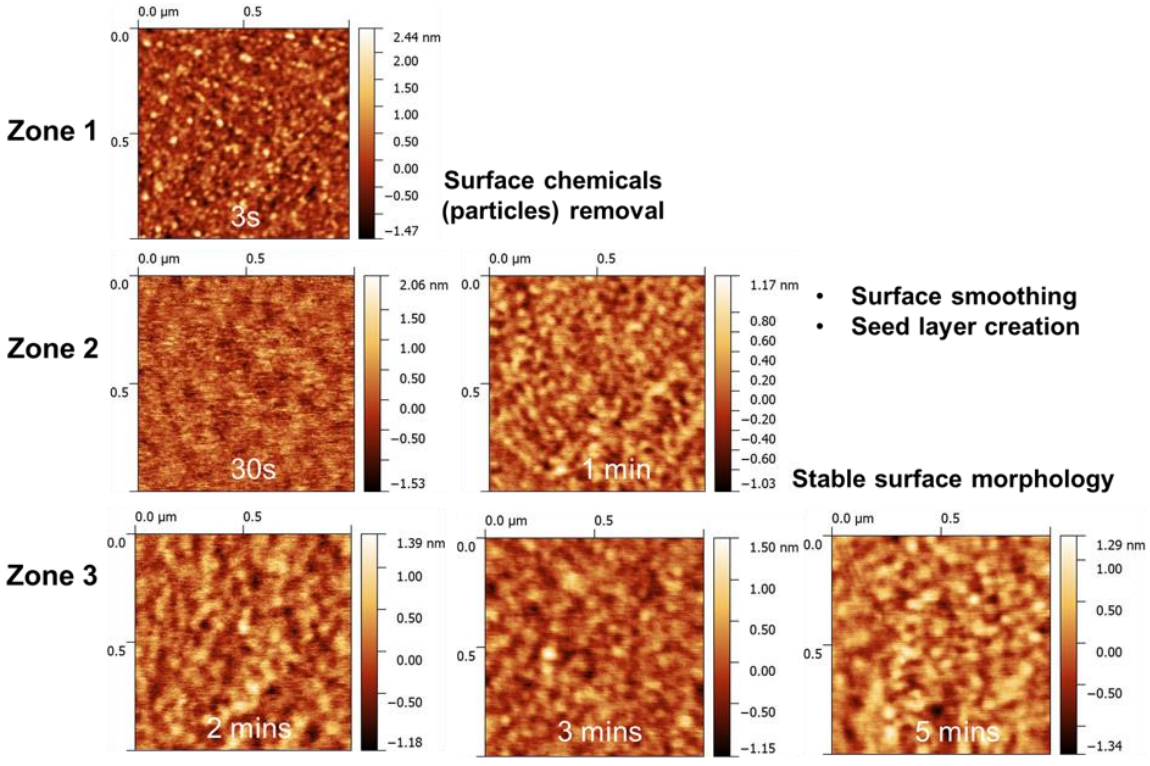

Figure 3.3 Atomic force microscopy (AFM) surface profiles of EPH with different ion pre-etching times.

The *in situ* RHEED images of the EPH surface with different ion bombardment times are shown in Figure 3.5. The polycrystalline ring of the Hastelloy substrate could be identified in both 0 and 30 s pre-etched samples. The RHEED pattern shifted when 15 s etching was applied. Multiple rings start to develop, which suggests a surface feature started to form, corresponding to samples of zone 2 in Figure 3.2 and 3.3. The "surface feature pattern" became apparent when the etching time reached 120 s and remained stable when the etching time reached 300 s. This finding is also consistent with texture stabilization in zone 3 as shown in Figure 3.2.

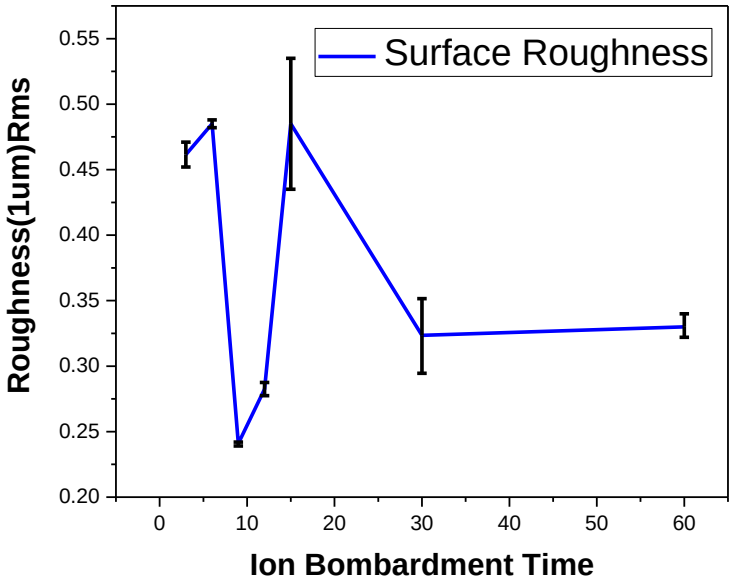

Figure 3.4 Surface roughness profile of EPH as a function of ion pre-etching time.

The surface morphology of IBAD TiN-coated EPH with different pre-etching times was also investigated using AFM (Figure 3.6). Many trenches and randomly-oriented TiN grains could be observed on the 3 s pre-etch samples and may be attributed to insufficient surface pre-etching before deposition. The samples processed with 180 and 300 s pre-etching show notable differences in which larger grains are more dominant

since the lower surface energy of ion bombarded EPH can benefit both the TiN nucleation and growth processes.

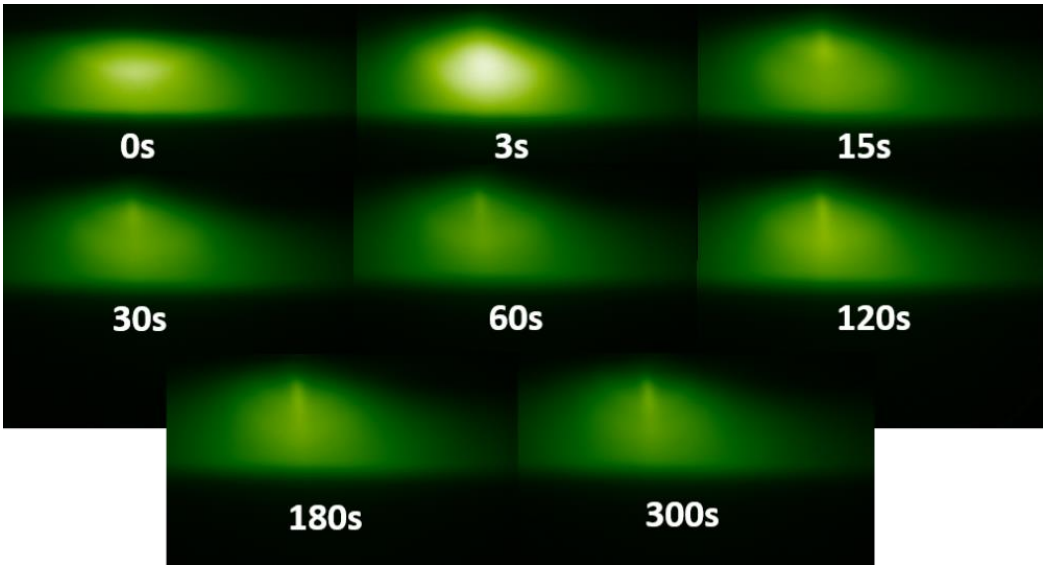

Figure 3.5 RHEED images of EPH as a function of surface pre-etching time.

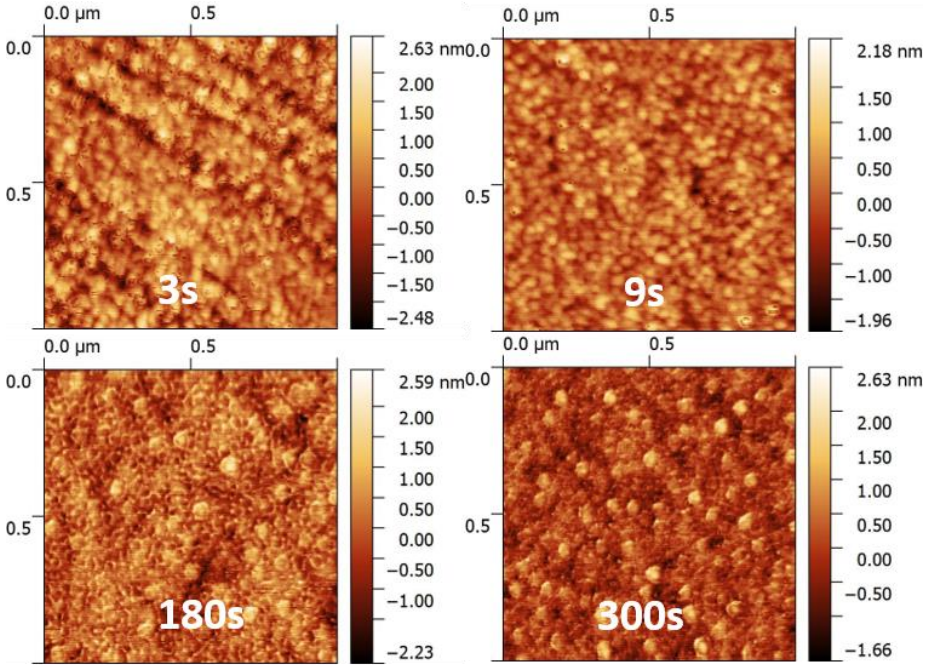

Figure 3.6 AFM surface profile of IBAD TiN with different surface pre-etching times.

In conclusion, the EPH surface profile has a significant influence on IBAD TiN nucleation and growth, and ion bombardment before the IBAD could significantly

improve the EPH surface condition that contributes to the IBAD TiN texture. Pre-etching by assist beam for an appropriate time could improve the adatom adhesion and also lower the surface energy of EPH. A time of 120 s was selected as the pre-etching time for the next steps in ion beam optimization.

3.2 Optimization of IBAD-TiN texture with different assist beam parameters

In this section, the optimization of TiN texture using different assist beam current and voltage is discussed in detail. All EPH samples were treated with 120 s ion bombardment which corresponds to 1.67 mm/s tape moving speed. The IBAD TiN process proceeded with the identical beam settings as described in section 2.2. Homo-epitaxial TiN also was deposited on top to improve the IBAD TiN texture.

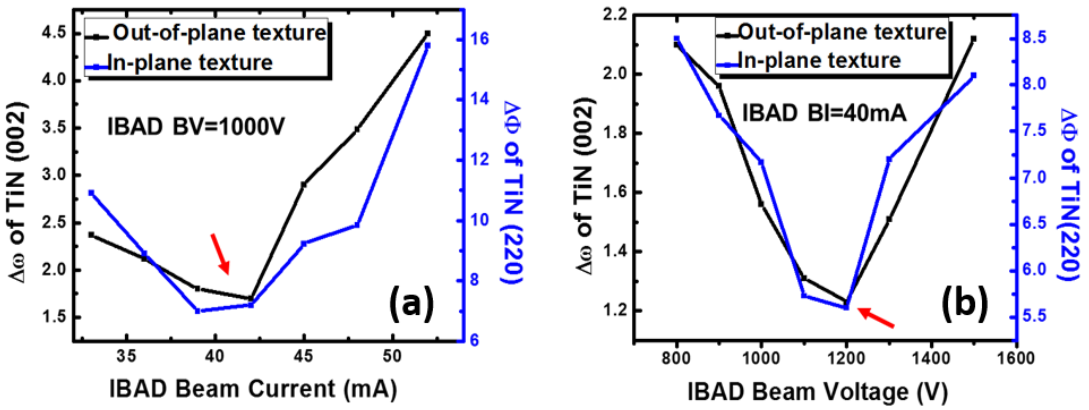

Figure 3.7 Biaxial TiN film texture as a function of (a) assist beam current; (b) assist beam voltage.

Figure 3.7 (a) shows the biaxial texture of TiN with different assist beam currents. In general, both in- and out-of-plane textures concurrently changed in the same manner. The texture improved when the beam current rose from 32 to 42 mA and started to degenerate rapidly when >42 mA current was applied. The texture reached the best value when the beam current was around 38 to 42 mA. At lower beam current level, the

assist beam energy is not capable of sputtering away enough adatoms, which means the grains in the non-channeling direction could still grow. On the contrary, a higher current could sputter away most of the adatoms and suppress the growth process; thus, the texture degraded quickly (particularly the out-of-plane texture) when the current higher was >42mA. The texture could reach Δω of 1.7º and Δφ of 7.2º when the beam current was maintained at 40 mA at 1000 V assist voltage.

An assist beam current of 40 mA was used to optimize the assist beam voltage value in the following step. As shown in Figure 3.7 (b), the TiN texture could reach a Δω of 1.2º and Δφ of 5.6º when the beam voltage was set at 1200V. Increasing the beam voltage from 800 to 1200 V provided enough energy to achieve good in-plane alignment since the ion beam traveled along the <110> direction from the nucleation step. However, if the beam voltage exceeds the appropriate level, the excessive assist beam energy will not only remove the misaligned grains but also suppress the growth, which means the IBAD film will not reach the critical thickness. In short, both beam current and voltage needed to be at an appropriate level to maintain the capability of the "orientation selection" by the assist beam until the IBAD film reached the critical thickness [28]. Assist beam parameters of 1200 V and 40 mA were selected for the next step.

3.3 Optimization of IBAD TiN texture with different ion exposure time

Since TiN has the same rock-salt cubic structure as MgO in which (100) is the preferred out-of-plane growth direction, very rapid texture evolution also could be observed in the IBAD TiN growth. The effect of ion exposure time on the TiN texture

was studied by using the optimized assist beam parameters described above. Figure 3.8 illustrates the RHEED images of IBAD TiN with different ion exposure times. At the beginning stage, the RHEED pattern of cubic TiN can be recognized from 30 s onwards after which the pattern became intense when the texture was gradually evolved. The changes in the RHEED pattern from 100 to 123 s indicates the deterioration of IBAD TiN texture in this step. Polycrystalline tails can be identified on in-plane (022) spots of RHEED image when 123 s deposition was reached. The middle out-of-plane spot also shifted to a broader shape, which illustrates the degradation of the out-of-plane texture. A fully polycrystalline ring-shaped RHEED pattern emerged when the IBAD TiN film reached 150 s growth [153].

Unlike YSZ, the biaxial texture formation of rock-salt cubic material only required a short time since the grains only needed to be aligned along the in-plane axis by the assist beam. In Figure 3.8, the texture evolution curve can be seen to perfectly fit with the changes in the corresponding RHEED patterns. Both $\Delta\omega$ and $\Delta\phi$ reached the best value at 110 s processing time (1.82 mm/s tape speed). At the beginning of the nucleation step, the grains start to become aligned by the assist beam along the channeling direction and then gradually grow larger and coalesce until they fully covered the substrate. Once the film thickness reached a critical level, the texture of the IBAD TiN degrades quickly. Thus, in general, the IBAD TiN could reach and maintain the best texture at its critical thickness when 1.82 mm/s was selected as the tape moving speed.

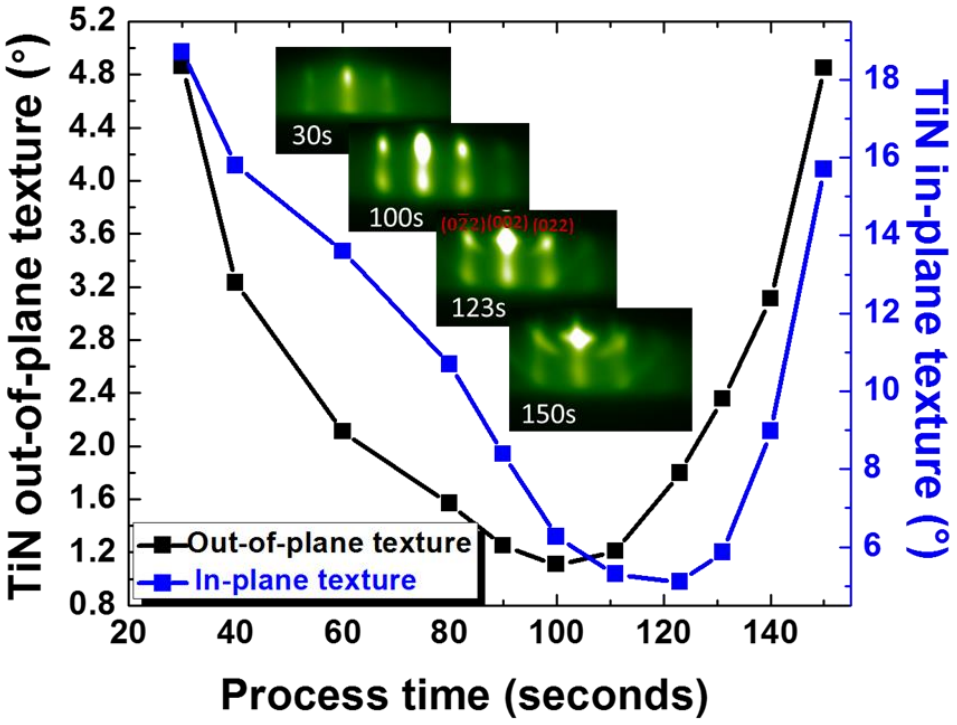

Figure 3.8 Biaxial TiN film texture with different IBAD ion exposure times (Corresponding RHEED images are also included)

3.4 Texture summary by XRD analysis of TiN buffer layer

Based on the previous discussion, the pre-etching time, assist beam parameters, and tape ion exposure time were fully optimized to achieve a highly biaxially-textured TiN film. The final process parameters are summarized in table 3.2.

Figure 3.9 (a) shows the theta-two theta scan of homo-epitaxial TiN growth on biaxial-textured IBAD TiN, which was processed with the previously described optimized parameters. Only the high-intensity TiN (200) peak was observed at $2\theta = 42.21^{o}$ in addition to the peak next to the Hastelloy peak (marked with a cross). The rocking curve (ω-scan) of the TiN (200) peak in Figure 3.9 (b) demonstrates an excellent out-of-plane texture since the FWHM was only 1.8^{o}. Figure 3.9 (c) and (d) provide the in-plane texture quality of the homo-epitaxial TiN film. The four-fold symmetry of the

peaks in TiN (220) pole figure confirmed the excellent alignment of the TiN in-plane texture, and the phi scan of these four peaks revealed an average FWHM ($\Delta\phi$) of 5.6º.

Table 3.2 Optimized growth conditions of IBAD TiN

	N_2 flow	Sputter Beam (IBSD)	Assist Beam (IBAD)	Time Duration
Surface Pre-etching	No	None	800V, 80mA	120s (1.67mm/s)
TiN	Yes	950V, 240mA	1200V, 40mA	110s (1.82mm/s)

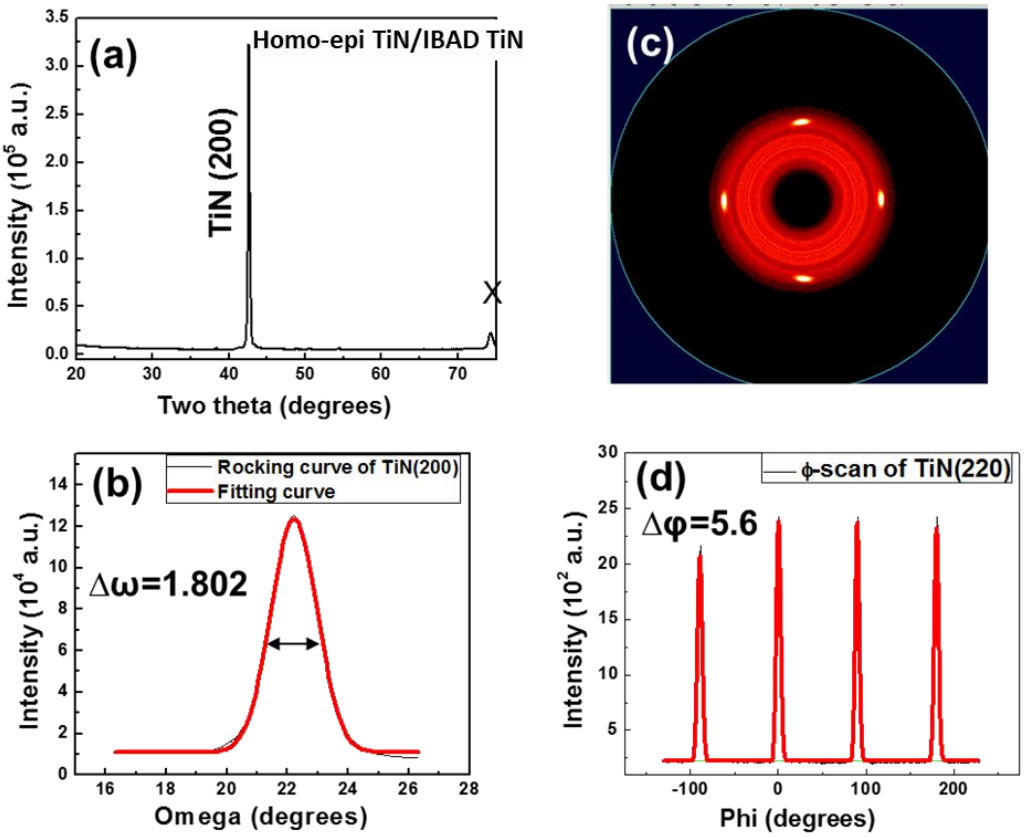

Figure 3.9 (a) θ–2θ X-ray diffraction (XRD) scan of homo-epitaxial TiN film grown on optimized IBAD-TiN/EPH; (b) Rocking curves of TiN (200) peak from(a); (c) (220) Pole figure of TiN (220); (d) Phi scan of four-fold symmetric TiN (220).

3.5 Summary

In conclusion, biaxially-textured TiN was successfully deposited on a polished Hastelloy substrate without using any foreign seed layer. Out-of-plane and in-plane textures ($\Delta\omega$ of 1.8º and $\Delta\phi$ of 5.6º, respectively) could be reached after optimizing the pre-etching time, assist beam parameters, and ion exposure time. The surface pre-treated with Ar ion bombardment was very crucial for realizing the IBAD TiN biaxial texture on the EPH. A more micro-level smoothed EPH surface was realized that improved adatoms adhesion for IBAD TiN.High-temperature sputter deposited homo-epitaxial TiN on top preserved the IBAD layer texture, so a fully-conductive buffer was achieved on the polished Hastelloy substrate without the use of any oxide buffers.

CHAPTER 4 BIAXIALLY-TEXTURED BUFFER GROWTH ON A NON-METALLIC FLEXIBLE SUBSTRATE

4.1 Surface Planarization for YSZ ribbon

As a non-metallic flexible ribbon, YSZ meets several requirements for a substrate for HTS tapes for high-frequency applications as discussed in chapter 1. However, as a powder-sintered ceramic, the original roughness of the YSZ ribbon could be very high. Growth of biaxially-textured thin films by the IBAD process requires a very low surface roughness (<1nm) substrate. So surface planarization of the YSZ ribbon is necessary to be used as the substrate in the IBAD process [154], [155]. Conventional mechanical polishing process may not satisfy the surface roughness requirement and is also expensive. A suitable surface planarization method has been developed in this work and IBAD MgO and LMO layers were successfully grown on this planarized YSZ ribbon.

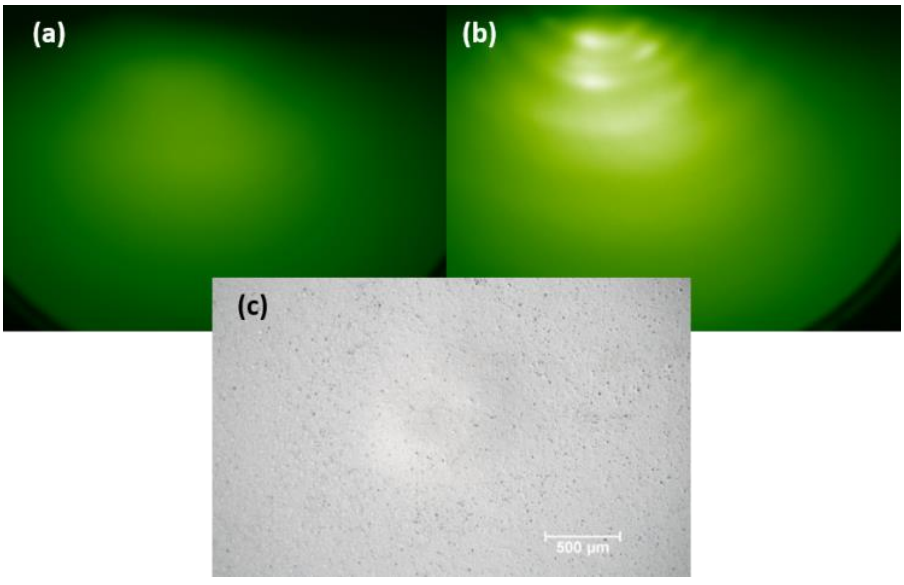

Figure 4.1 (a) Real-time RHEED pattern of as-received YSZ (b) IBAD MgO/Y_2O_3 growth on as-received YSZ (c) optical image of the ENrG YSZ surface.

Figure 4.1 (c) shows an optical image of the surface of an as-received YSZ ribbon. The dense YSZ shows a very rough surface as received which was confirmed by AFM morphology measurements (Figure 4.1 a). No peak was seen in real-time RHEED images (Figure 4.1 a) for as-received YSZ, which indicates the translucence property of the YSZ ribbon. IBAD MgO/Y_2O_3 buffer was directly grown on as-received YSZ, and the resulting RHEED pattern is shown in Figure 4.1 (b). Misoriented polycrystal peaks and rings in the RHEED image could be due to the rough YSZ surface that could have hindered biaxial texture growth. Therefore, surface planarization is a prerequisite for epitaxial growth of the buffer layer on YSZ.

4.1.1 Material selection for surface planarization

In the semiconductor industry, surface planarization is critical due to the requirements for sophisticated micro-level multilayer stacking structure of the modern integrated circuit (IC) [156]. In contrast to traditional chemical-mechanical polishing for ultra-flat surfaces of a wafer via mechanically abrasive and chemically corrosive slurries, a sol-gel coating method is used to planarize the surface. The sol-gel usually contains the desired precursor and a specific solvent. It could be coated on a surface by spinning, dip coating, blade coating, ink printing, or any other roll-to-roll method [157]. Large-scale surface coating can be achieved with appropriate surface pre-treatment.

Spin-on glass (SOG) is a very common sol-gel used in the semiconductor industry for surface planarization, diffusion doping, or dielectric layer coating [158]. It contains different silicon-based precursors and specific solvent. The choice of SOG mainly depends on the coating application.

Commercial SOG is classified as silicates, dopant silicates, organic silicon compounds, and dopant-organic compounds [159]. For example, phosphosilicates are silicate-type SOG for phosphorous doping. Methylsiloxanes and methyl silsesquioxane are two types of SOG with organic silicon compounds that are better for surface planarization.

Filmtronics 700B spin-on glass was used for YSZ ribbon surface planarization in this work. 700B is silicate-based SOG that densifies into a SiO_2 film after the high-temperature curing process [160]. All YSZ ribbons used in this work were cleaned before the coating process. The surface roughness of the YSZ ribbon is reduced from 51.89 nm to 3.23 nm by two-layer coating at 3000 rpm for 60 seconds (Figure 4.2) (a) (b). However, surface was observed to be cracked after the two-layer coating process as shown in Figure 4.2 (c). The reason for cracking may be due to the SOG itself. The silicate-based 700B SOG exhibits high shrinkage (15%). This shrinkage could induce high tensile stress at the interface between film and substrate and give rise to a crack.

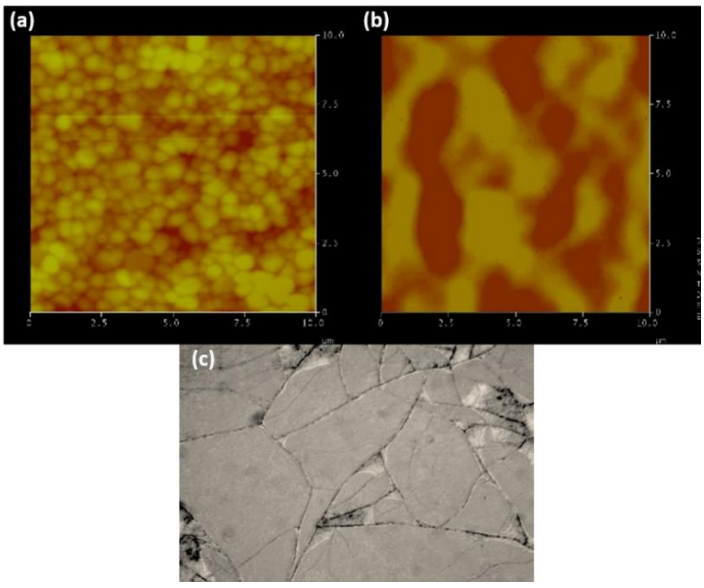

Figure 4.2 AFM surface profile of (a) as-received YSZ ribbon (10 μm x 10 μm); (b) YSZ surface planarized with Filmtronics 700B SOG (10 μm x 10 μm); (c) optical image of YSZ surface after coating.

Another kind of SOG has been studied in this work is IC1-200 which is a polysiloxane based SOG with lower shrinkage. The same spin coating process was applied used for the planarization process with IC1-200 [161]. In contrast to the 700B SOG, the film maintains integrity after three layers of spin coating. The coated YSZ surface becomes densified and glossy after the curing process. Only at a micrometer level cracks are seen on very edge sides due to sharp thickness gradients.

In summary, low shrinkage and low tensile stress organic silicon-based SOGs are appropriate surface planarization materials for YSZ ribbon. A detailed coating process will be discussed next.

4.1.2 YSZ ribbon surface planarization by multilayer SOG

IC1-200 Spin-on Glass from Futurrex Inc. was used here for the coating process. The YSZ ribbon used for spin coating here was laser cut to a 10 mm × 20 mm size to fit the spinner. Pre-treatment procedures include:

30 minute furnace baking at 600 ºC with N_2 flow to remove the organics on as-received YSZ.

Ultrasonic cleaning using acetone and water, and ozone cleaning occurred in sequence for ten minutes each to remove any contaminants from the handling process. All the cleaning and coating process were performed in a class 100 cleanroom.

The spinning coating processing recipe consisted of multiple steps of coating each layer:

- 3000 rpm, 40 seconds spin coating with PDMS-made YSZ ribbon holder
- 100ºC bake, 60 seconds, 200ºC bake, 60 seconds

This recipe was repeated multiple times to achieve a low roughness surface on the YSZ ribbon. The baking process evaporates the solvent and stabilizes the polysiloxane gel.

After the multilayer coating process, all samples were baked in a furnace at 400ºC with N_2 flow. The organic compounds in SOG are decomposed and condensed to a silicon dioxide film after this curing process.

Figure 4.3 (a) is an optical microscope image of the YSZ surface after the planarization process. a uniform surface was observed on the entire surface area without any cracks. Figure 4.3 (b) demonstrates that the YSZ ribbon maintains its flexibility after the coating process. A 150 cm long YSZ ribbon was coated with multilayers of SOG via a specially-designed holder and is also shown in Figure 4.3 (c).

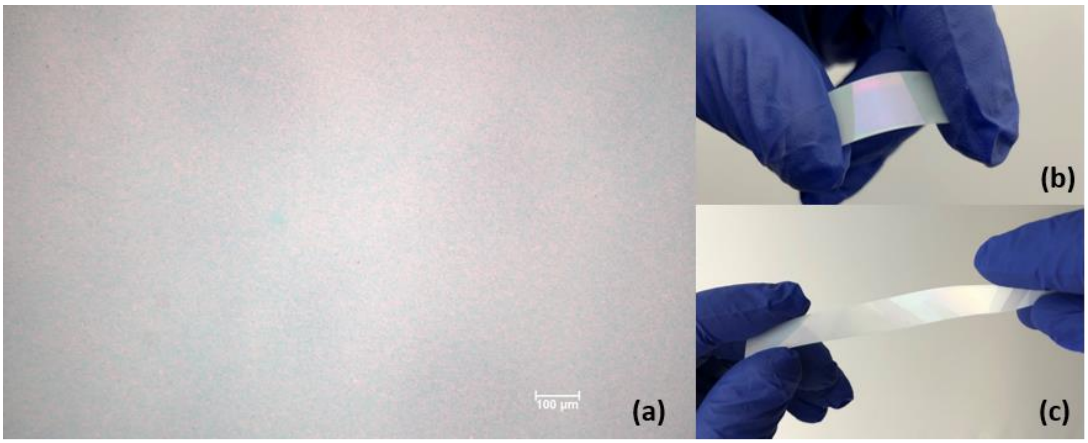

Figure 4.3 (a) Optical image of the YSZ surface with SOG coating film; (b) Photograph of 10mm × 20mm SOG coated YSZ ribbon; (c) Photograph of 10mm × 150mm SOG coated YSZ ribbon.

4.1.3 Characterization of YSZ surface morphology after multilayer planarization

The surface morphology was checked on uncoated as well as two, three, and four SOG layer coated YSZ ribbons. All measurements were done by AFM (Oxford Instrument MFP-3D Origin+ Atomic Force Microscope) in air tapping mode.

Roughness data was averaged from three points of analysis to ensure accuracy. Figure 4.4 shows the surface morphology of the as-received YSZ ribbon in dimensions of 5μm × 5μm and 20μm × 20 μm. The roughness (RMS) for these two scales is 28.35 nm and 28.45 nm, respectively. Large grains with a few pits were observed on the surface. A similar roughness at different scales indicates that the surface is uniform. Some deep pits on the surface may have been from the sintering process of the YSZ ribbon.

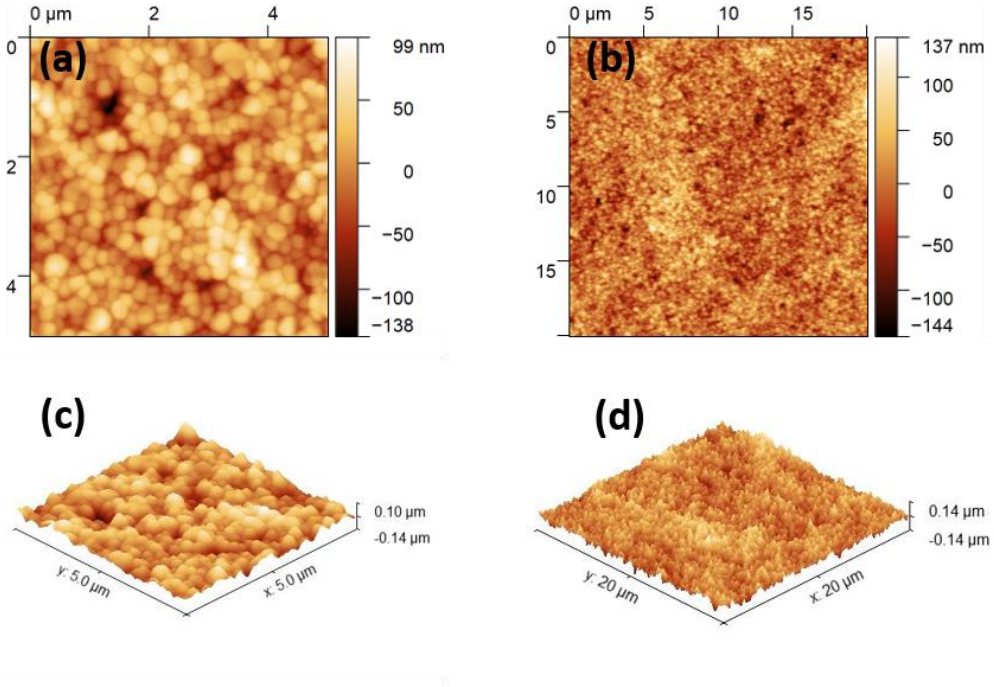

Figure 4.4 AFM surface profile of (a) as-received YSZ ribbon surface in 5 μm × 5 μm scale, Rq (RMS) is 28.35 nm; (b) as-received YSZ ribbon surface in 20 μm × 20 μm scale, Rq (RMS) is 28.45 nm; (c) 3D view of as-received YSZ ribbon surface in 5μm × 5μm scale surface; and (d) 3D view of as-received YSZ ribbon surface in 20 μm × 20 μm scale.

The surface morphologies of two, three, four layers SOG-coated YSZ ribbons in 5 μm × 5 μm scale are shown in Figure 4.5. No apparent asperities and particles observed, and the surface becomes flatter after the coating process. Some shallow dents were also noted on both two layer and three layer coated samples, which may be the remaining pits in the as-received YSZ. The R_q (RMS) roughness drops to 6.17 nm for the two-

layer coating sample and 1.84 nm for the three-layer coating samples. The average R_q (RMS) on four layer coated YSZ becomes 1.07 nm which is the same level as electropolished Hastelloy tape used to for IBAD TiN buffer layers. This implies that the YSZ ribbon after planarization should be qualified for the IBAD buffer growth.

Figure 4.6 summarizes the roughness change with an increasing number of SOG coating layers. The average roughness drops to 5 μm after two layers of coating. However, the large error range of the two-layer-coated film roughness indicates the uniformity of the surface cannot be guaranteed since pits exist on as-received YSZ even after two layers of coating. The surface roughness dropped to 1-2 nm after three to four layers of coating, which indicates low roughness and uniform surface morphology can be achieved after at least three rounds of SOG planarization process. In conclusion, three layers of SOG coating on the YSZ ribbon are necessary to ensure the surface roughness in an acceptable range for IBAD biaxial texture film growth.

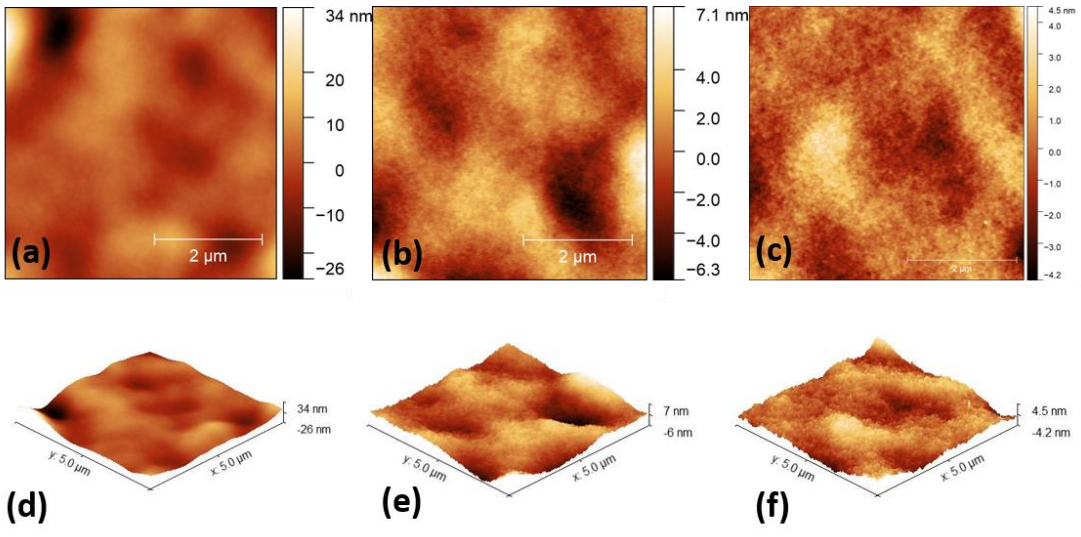

Figure 4.5 AFM surface profile of (a) two layer SOG coated YSZ ribbon surface in 5 μm × 5 μm scale, average R_q (RMS) is 6.17 nm; (b) three layer SOG-coated YSZ ribbon surface in 5 μm × 5μm scale, average R_q (RMS) is 1.84 nm; (c) four layer SOG-coated YSZ ribbon surface in 5 μm × 5 μm scale, average R_q (RMS) is 1.07 nm; (d),(e),and (f) are 3D views of two, three, four layer SOG-coated YSZ, respectively.

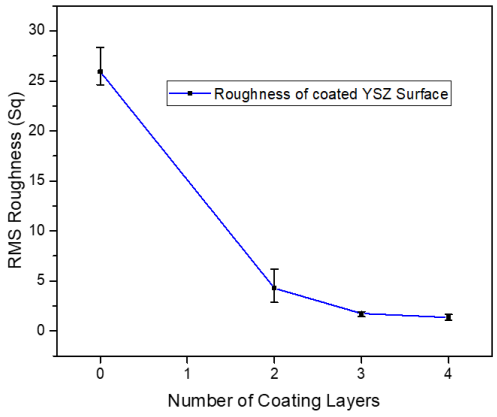

Figure 4.6 Summary of SOG-coated surface roughness with increasing number of coating layers. Roughness data is an average of three points of each sample.

4.1.4 IBAD MgO texture with different number of planarization layers

In order to study the relationship between YSZ surface roughness and the buffer's biaxial texture quality, IBAD MgO/Y_2O_3 was deposited on planarized YSZ ribbons. The parameters are detailed in Table 4.1. An in situ RHEED system was used to check the quality of IBAD MgO during the IBAD process.

Table 4.1 Growth condition for IBAD Y_2O_3/MgO.

	O_2 flow	**Sputter Beam (IBSD)**	**Assist Beam (IBAD)**	**Time Duration**
Surface Pre-etching	No	None	800V, 80mA	5s
Y_2O_3	Yes	1100V, 400mA	None	60s
MgO	Yes	1100V, 400mA	900V, 100mA	40s

Figure 4.7 shows the RHEED pattern for IBAD MgO on the YSZ ribbon with a different number of planarization layers. All the in situ RHEED pictures were captured after the deposition process using the same aperture and focus parameters. The RHEED diffraction pattern of IBAD MgO/YSZ shows similar features as IBAD MgO/Hastelloy,

so indicating that (100)-oriented biaxially-textured IBAD MgO was successfully achieved on the flexible YSZ substrate as well. The diffraction spots of biaxially textured MgO become brighter and sharp when using more planarization layers which indicates that the texture is better developed. All of the texture figures discussed in the next sections refer to MgO (200) and $LaMnO_3$(LMO) (002) as out-of-plane orientations MgO (220) and LMO (110) as in-plane orientations.

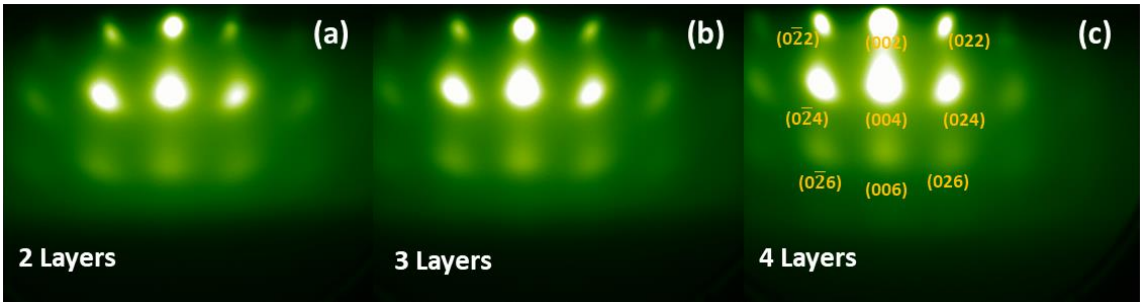

Figure 4.7 RHEED pattern of IBAD MgO on YSZ ribbon with different numbers of planarization layers.

In order to quantify the texture quality of IBAD MgO, 150 nm homoepitaxial MgO and 150 nm LMO thin films were deposited on IBAD MgO film at heater susceptor temperatures of 850ºC and 900ºC respectively with a roll-to-roll PVD system. The O_2 partial pressure was maintained at 1.5 E-4 mbar for MgO deposition and 4 sccm O_2 and 100 sccm Ar were used for LMO process. Out-of-plane and in-plane texture information of the MgO layer and LMO layer were collected from XRD data (Figure 4.8). Multiple repeat samples were performed in this experiment.

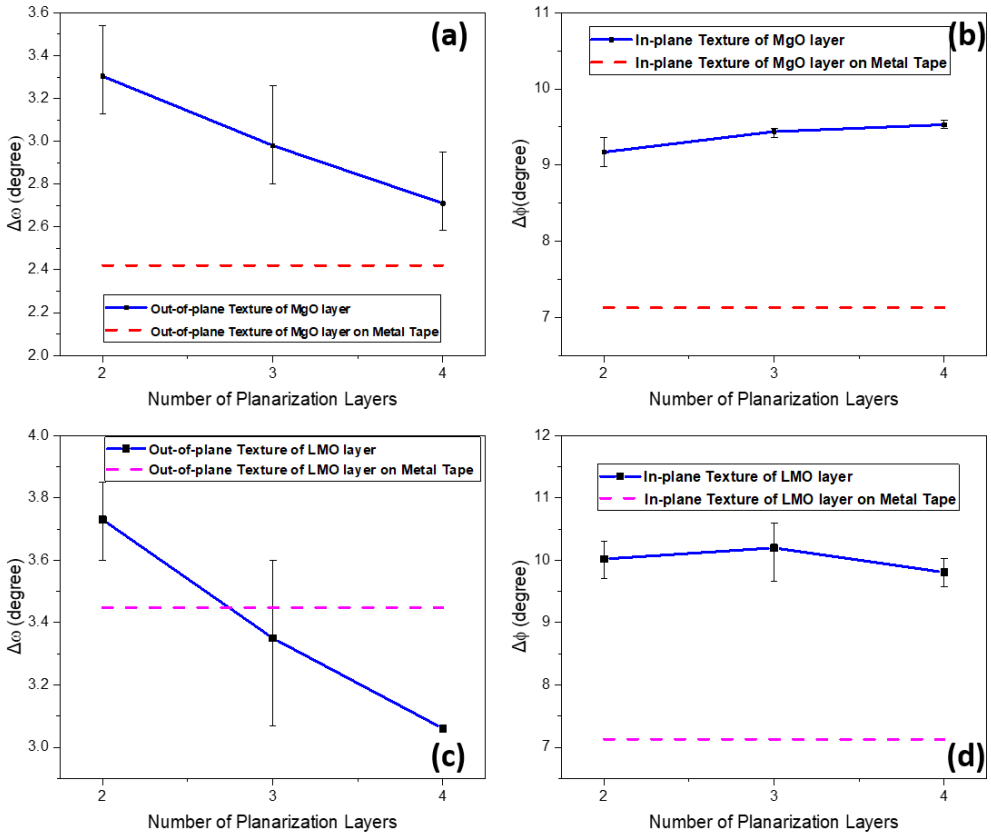

Figure 4.8 Biaxial film texture as a function of planarization layers number. (a) (b) Out-of-plane (Δω) and in-plane (Δϕ) texture of MgO layer, respectively; (c) (d) Out-of-plane (Δω) and in-plane (Δϕ) texture of LMO layer, respectively.

In Figure 4.8 (a) (c), the full-width-at-half-maximum (FWHM) of the omega scan (Δω) of the MgO/LMO layer decreases when more planarization layers are used. The RHEED diffraction pattern also indicates that the Δω improved. The (002)/(004) spots gradually narrow in width direction and extend in the height direction, and become close to the tear-drop shaped diffraction spots of homoepitaxial MgO. However, the in-plane texture (Δϕ) (Figure 4.8 b, d) obtained from phi scans are broad: around 9º for MgO and 10º for LMO layer. The in-plane texture did not show too much change when more coating layers were added. The shape of the (024) and (02$\bar{4}$) diffraction spots did not change much when more coating layers were added. A low roughness surface is crucial

for the IBAD biaxial texture formation since the growth orientation selection in the IBAD process mainly relies on the ion channeling direction. If the normal direction of the substrate is locally tilted, then the misoriented MgO could get more chances to grow, which means that the MgO could be tilted both in-plane and out-plane. The MgO (002) growth could be suppressed due to the high ion bombardment rate caused by misalignment. The chance for misoriented MgO grain growth is less when the surface roughness decreases, which is also indicated by the smaller $\Delta\omega$ of the thin film. As noted in Figure 4.8 (a) (c), the MgO and LMO buffer structure on flexible YSZ already reached the same level as the out-of-plane texture of a standard buffer on metal tape.

4.2 Biaxially-textured MgO buffer on flexible YSZ via the IBAD process

Besides the surface roughness, the IBAD buffer layer process conditions were optimized for texture improvement. The investigated IBAD parameters include assist beam voltage (V_A) and assist beam current (I_A). In situ RHEED systems were also used here to check the quality of IBAD MgO. To verify the texture quality from in situ RHEED, homoepitaxial MgO and LMO layers were grown on these YSZ samples by roll-to-roll PVD methods using the same conditions as described before.

4.2.1 Buffer texture optimization with IBAD-assisted beam voltage

Based on the previous findings, four layers of SOG coating were applied to the YSZ ribbon. In the IBAD deposition process, the SOG film surface was pre-etched for 5 seconds to remove any possible contamination and homogenize the entire surface. The Y_2O_3 seed layer was then deposited using the parameters listed in Table 4.1. Next, IBAD MgO was grown using different V_A conditions and constant I_A (100 mA); the

sputtering beam parameters are also listed in Table 4.1. 40 seconds of deposition was performed for all samples.

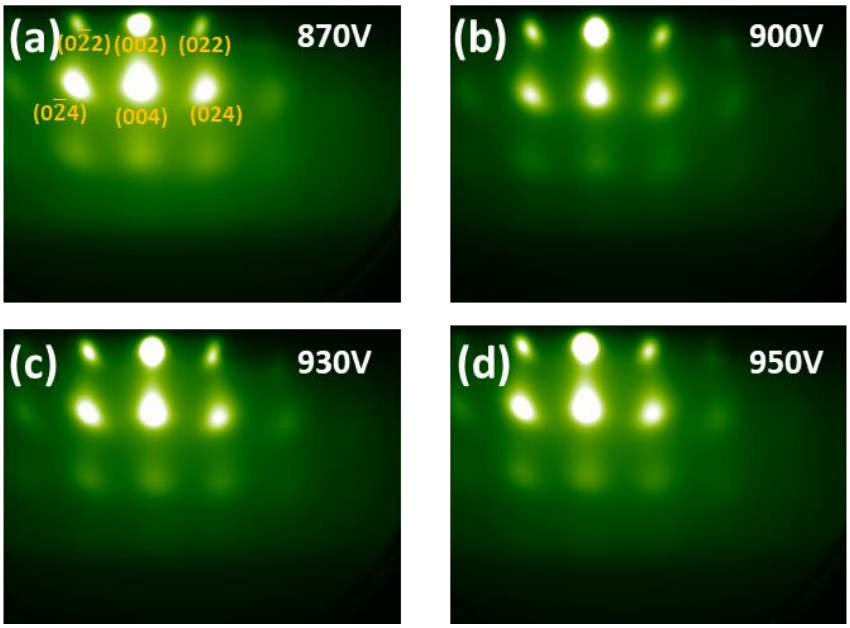

Figure 4.9 RHEED pattern of IBAD MgO with different assist beam voltage on four layers planarized YSZ (a)870V, (b)900V (c)930V (d) 950V.

Figure 4.9 shows the RHEED pattern images for IBAD MgO on YSZ when the assist ion beam voltage is increased from 870 V to 950 V. The diffraction spots become sharper at 930 V. So, a higher assist ion beam voltage may benefit the IBAD MgO texture. However, the MgO films deposited at 930 V and 950 V are difficult to distinguish from the RHEED image. The high voltage likely ensures that the grain is aligned at the early nucleation stage. However, the in-plane orientation (022) spot is still not as sharp as the middle out-of-plane (002) spot. This weak in-plane peak indicates that the assist ion beam energy is still insufficient to obtain a strong in-plane alignment.

150 nm thick MgO and 150 nm thick LMO were deposited on the IBAD MgO film of these YSZ samples. XRD texture analysis for both in-plane and out-of-plane texture is shown in Figure 4.10.

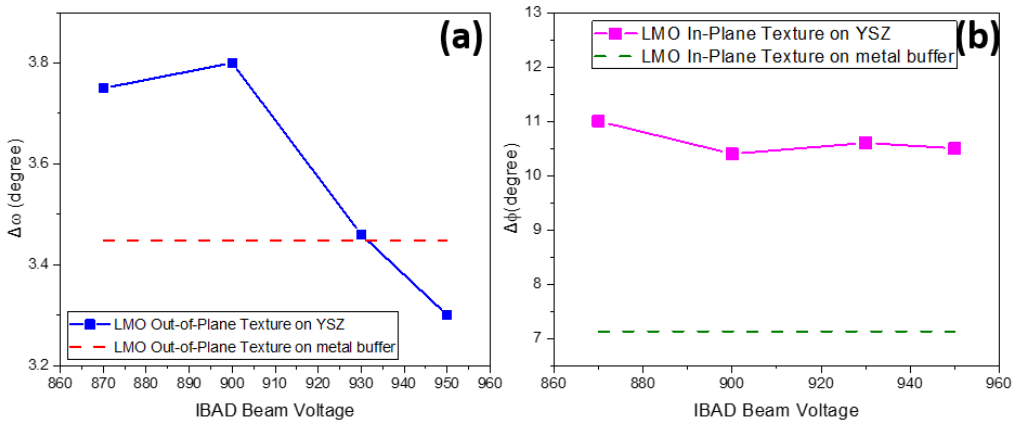

Figure 4.10 Biaxial LMO texture change with different assist ion beam voltage (VA). (a) Out-of-plane (Δω) of LMO layer; (b) In-plane (Δϕ) texture of the LMO layer.

The XRD results also reflect the same trend as the RHEED patterns. The out-of-plane texture (Δω) drops from 3.8º to 3.4º at the highest assist beam voltage, and it is already lower than the Δω of LMO texture on metal tape. However, the 10º level in-plane Δϕ is still much higher compared to LMO in-plane texture on metal tape. The beam current was investigated in the next step.

4.2.2 Buffer texture optimization with IBAD-assisted beam current

To investigate the influence of assist beam current on the buffer layers texture, the YSZ ribbon with four layers of surface planarization was used for the IBAD buffer growth process. All samples had the same IBAD Y_2O_3 layers and the same sputter beam parameters as before. An assist beam voltage V_A = 950V was selected from the optimization in the previous step.

The RHEED patterns are very different at different assist ion beam current I_A used in the IBAD MgO growth process. Figure 4.11 shows that the RHEED pattern becomes more explicit when I_A shifts to a higher level. However, this trend changed when the

current level reaches 120mA. The in-plane spots and surrounding pattern become blurry, and polycrystalline features start to appear in the RHEED pattern. The MgO texture has degenerated when a I_A higher than 140mA is used. In the low I_A range (90 mA), the ion beam energy cannot control the orientation of MgO in the nucleation process, and parts of the grains become misoriented. The deposition rate should fit with the assist beam energy for balance. If the deposition rate is too high (using a higher sputter beam voltage and current) and the assist beam energy is relatively low, then the orientation cannot be adequately controlled before reaching the critical thickness of IBAD MgO. In contrast, if a high assist beam energy is applied here, then the ion bombardment will be more active instead of orientation selection. The blurry RHEED pattern images of 120 mA and 140 mA I_A samples could be similarly explained.

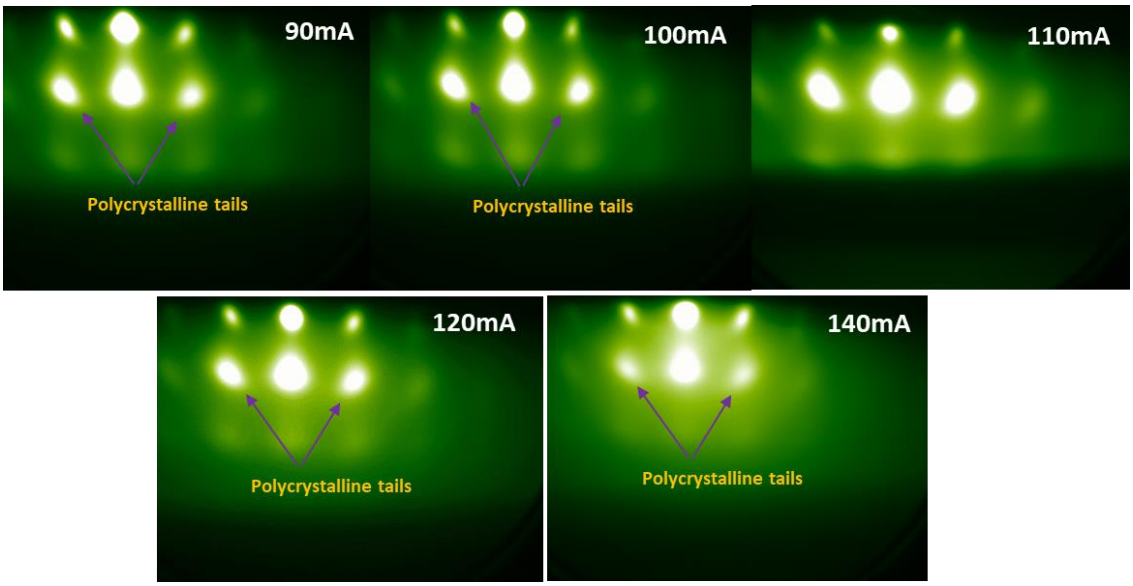

Figure 4.11 RHEED images of IBAD MgO with different assist beam currents on four layers of planarized YSZ.

The texture details were also studied by XRD of the homoepitaxial MgO and LMO grown under the same conditions as used before. The texture of both the MgO and LMO

are shown in Figure 4.12. The dashed line in the figure indicates an optimized standard buffer layer texture on Hastelloy tape.

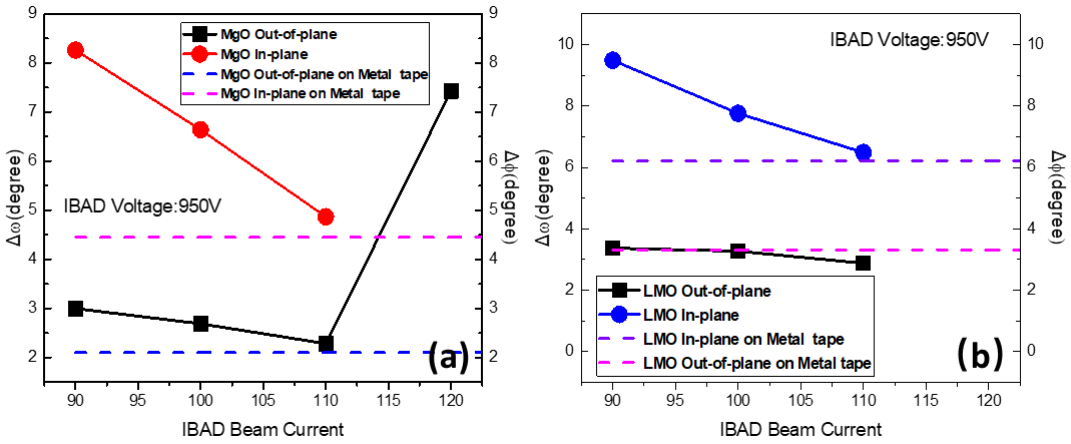

Figure 4.12 Biaxial LMO and MgO texture changes with different assist ion beam current (IA) (a) Δω and Δϕ of MgO layer; (b) Δω and Δϕ of LMO layer.

In Figure 4.12 (a), the Δω of MgO drops from 3.1º to around 2.2º when the beam current is increasing from 90 mA to 110 mA. It suddenly increases to 7.4º when the I_A reaches 120 mA. The 140-mA sample does not have any data points in the figure because no peaks were observed in the XRD scan. The deterioration of the Δω is due to the excessive surface ion-bombardment and is consistent with the RHEED analysis. The Δω of LMO also decreases from 3.37º to 2.87º when I_A increases. This slight change indicates that there is not too much room left for out-plane texture optimization. In general, both MgO and LMO texture reach the same level as the optimized standard buffer on Hastelloy metal tape when 110 mA I_A and 950V V_A were used.

The in-plane texture shows significant improvement when the I_A is raised in the IBAD MgO deposition process. No MgO (220) peak was observed in XRD when 120 mA and 140 mA I_A are applied in the IBAD MgO process. The in-plane texture trend of MgO in Figure 4.12 (a) suggests that the in-plane texture suddenly degenerated after the texture reaches the best at 110 mA I_A. This might indicate a slight change of I_A at a

high V_A level could significantly alter the energy density of the assist ion beam. This possible reason could also be used to explain the significant difference of IBAD MgO RHEED images between different I_A levels.

Since the MgO $\Delta\phi$ decreased from 8.2º to 4.8º when higher I_A was applied, a good LMO $\Delta\phi$ was also expected. In Figure 4.12 (b), the $\Delta\phi$ of the LMO sample processed at 100 mA beam current and 950V beam voltage is 7.8º, which is significantly lower than the previous 10.5º. All texture values in Figure 4.12 are better partly because the measurements were conducted with a new GADDS XRD tool which has a higher resolution. Besides that, the data shown in Figure 4.12 were obtained from samples processed with new targets and accordingly a higher O_2 flow during homoepitaxial MgO growth, which could have influenced the in-plane texture too. With the increase of ion beam current, the LMO in-plane texture decreases from 9.5º to 6.4º at 110 mA I_A. A higher I_A at this assisted beam voltage level can only damage the texture; thus, no XRD data are available when I_A is beyond 110 mA. In conclusion, 110 mA is the best assist ion beam level for achieving good biaxial buffer layer texture on top of the planarized YSZ ribbon when a 950 V ion beam voltage applied.

4.2.3 Buffer texture optimization with IBAD MgO deposition time

Biaxial texture MgO on the amorphous Y_2O_3 needs time for the nucleation and growth process. As illustrated in chapter 1, the IBAD biaxial film texture will improve until it reaches a critical thickness after a specific deposition time. The in situ RHEED system be used to monitor this texture development during the growth process. The IBAD MgO RHEED pattern growth on YSZ starts to emerge at around 7 s to 10 s when the sample surface is exposed to both assist beam and sputtering beam. A MgO

polycrystalline ring is usually observed after 50-60 s of exposure time. This timeline is not constant since this growth process is mainly controlled by the energy level of the sputtering beam and assist beam. For example, a higher assist beam energy could intensify the ion bombardment, and this can cause the biaxial RHEED pattern to emerge slowly.

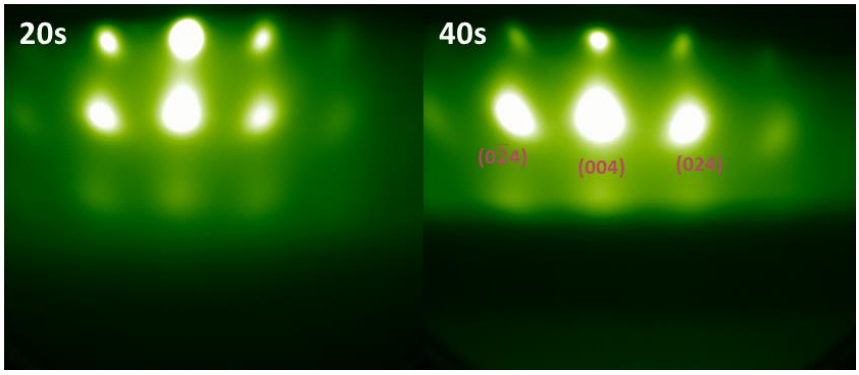

Figure 4.13 RHEED pattern of IBAD MgO with different MgO deposition times on four-layer planarized YSZ.

The influence of ion exposure time on biaxial IBAD MgO texture quality was studied. Two deposition times lengths were examined: 20 s and 40 s. The Y_2O_3 deposition followed Table 4.1 parameters, and 950 V V_A and 110 mA I_A were used as the assist beam settings for the IBAD MgO process. Figure 4.13 shows the RHEED patterns of both samples after the IBAD process. The shape of MgO (004) spots remain identical in both RHEED patterns. The (024) in-plane peak becomes brighter and sharper in the 40 s sample. This is attributed to the cubic structure of MgO; the c-axis <100> out-plane direction is aligned at the very beginning of MgO nucleation. The assisted beam has a 45º angle with the normal direction of the substrate and is mostly used for in-plane <110> direction alignment after the initial nucleation step. In this case, the in-plane orientation needs a longer time to achieve the preferred orientation. The homoepitaxial MgO and LMO texture are listed in Table 4.2.

The slight changes in both MgO and LMO Δω confirm that the out-of-plane alignment may reached the ceiling level at the beginning step during the IBAD MgO growth. The Δϕ keeps decreasing with more protracted process time. For achieving better IBAD MgO texture on YSZ, the IBAD MgO deposition time should be investigated with different sputter/assist beam energy level.

Table 4.2 Homoepitaxial MgO and LMO texture summary -YSZ samples with different time of IBAD MgO deposition.

	MgO Out-of-plane Δω	**MgO In-plane Δϕ**	**$LaMnO_3$ Out-of-plane Δω**	**$LaMnO_3$ In-plane Δϕ**
20 seconds Sample	2.4º	5.4º	3.1º	6.63º
40 seconds Sample	2.2º	4.8º	2.87º	6.48º

In general, the biaxial LMO/MgO buffer structure texture quality can reach a level same as the texture quality of LMO/MgO/Hastelloy. The optimized assist beam voltage, current, and deposition time parameters, as well as details of the XRD pattern, will be summarized in the next section.

4.2.4 Summary of growth condition and texture of biaxially-textured MgO/$LaMnO_3$ buffer on surface-planarized YSZ ribbon

Based on the discussion in the previous sections, the optimized condition to achieve a biaxial texture of films on YSZ ribbon has been summarized in table 4.3. The texture quality of functional layers such as REBCO on YSZ ribbon will depend on the optimized buffer texture.

Table 4.3 Optimized conditions for achieving biaxially-textured IBAD MgO on a YSZ ribbon.

	O_2 flow	Sputter Beam (IBSD)	Assist Beam (IBAD)	Time Duration
Number of planarization layers	4 layers with SOG			
Surface Pre-etching	No	None	800V, 80mA	5s
Y_2O_3	Yes	1100V, 400mA	None	60s
MgO	Yes	1100V, 400mA	950V, 110mA	40s

4.3 Homoepitaxial layer buffer layers on YSZ ribbon

All samples were processed with homoepitaxial MgO and LMO as the buffer structure for REBCO growth. The condition for these two layers' growth was already optimized and discussed in previous studies. The details of XRD analysis described next are these buffers on YSZ ribbons with optimized IBAD MgO.

4.3.1 XRD analysis for the homoepitaxial buffer layer on surface planarized YSZ

XRD analysis was performed on the homoepitaxial LMO and MgO buffer layers with the optimized IBAD MgO condition on the YSZ ribbon. The same XRD measurement was also conducted on the standard buffer on Hastelloy with the same buffer layer structure. All measurements were performed by the GADDS system.

Figure 4.14 (a) shows the 2D GADDS XRD scan of the standard buffer layers on the Hastelloy. The peak intensity is shown by the colored log scale. The background contrast was adjusted in the Bruker GADDS image process program (EVA) to reach a clear and sharp picture. The scan range is 1º to 58º in two theta direction and 18º in χ

direction. The polycrystalline diffraction rings from Hastelloy and YSZ are marked in (a) and (b), respectively. The peak intensities are relatively low in Hastelloy buffer structure, which means that the film thickness is less than that of the buffer films on YSZ. Figure 4.14 (b) shows a χ direction shift between LMO and MgO; this may because of the quality issue with the as-received YSZ. Micro-sized pits were observed on as-received YSZ, which could cause film nonuniformity in a local region. Only slight twins of LMO (001) exist, and these do not affect the texture quality. No peak was observed for the densified SOG layer.

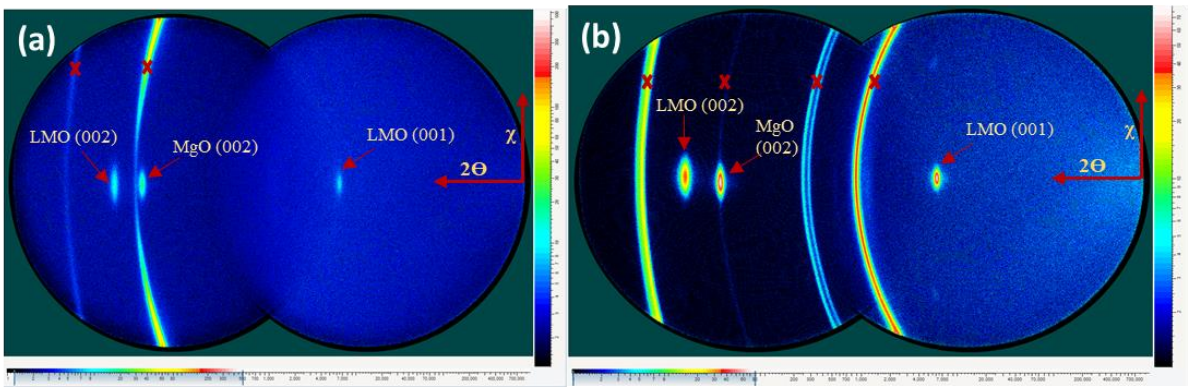

Figure 4.14 GADDS diffraction patterns for (a) LMO/MgO/IBAD MgO/Hastelloy buffer structure; (b) LMO/MgO/IBAD MgO/SOG/YSZ buffer structure.

YSZ with a homoepitaxial MgO buffer was also checked by the RHEED system (Figure 4.15 a, b). The image in Fig 4.15 (b) is slightly tilted due to the mounting. Nevertheless, bright, sharp uniform diffraction spots were seen, which suggests that the MgO layer texture been strengthened after the high-temperature homoepitaxial layer growth. Figure 4.15 (c) shows that the YSZ has excellent flexibility after all the buffer layers deposition process. The surface is glassy and uniform, which means the underneath SOG film maintains its density and is still intact after all the high-temperature roll-to-roll deposition processes.

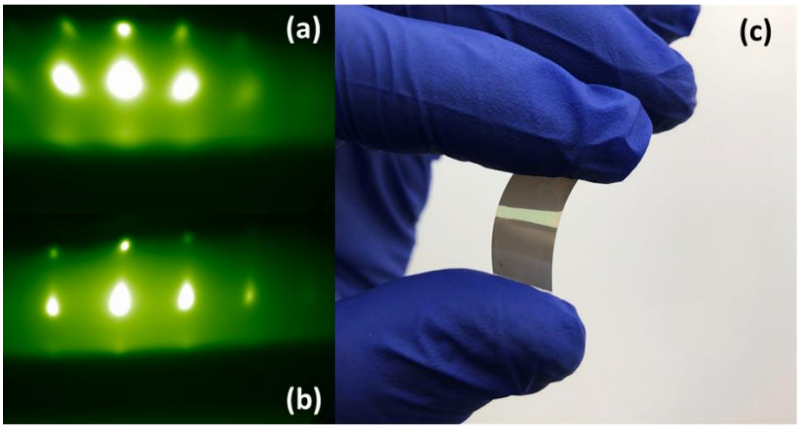

Figure 4.15 RHEED images of (a)IBAD MgO/YSZ and (b) homoepitaxial MgO/IBAD MgO/YSZ; (c) photo of flexible YSZ ribbon after the buffer process.

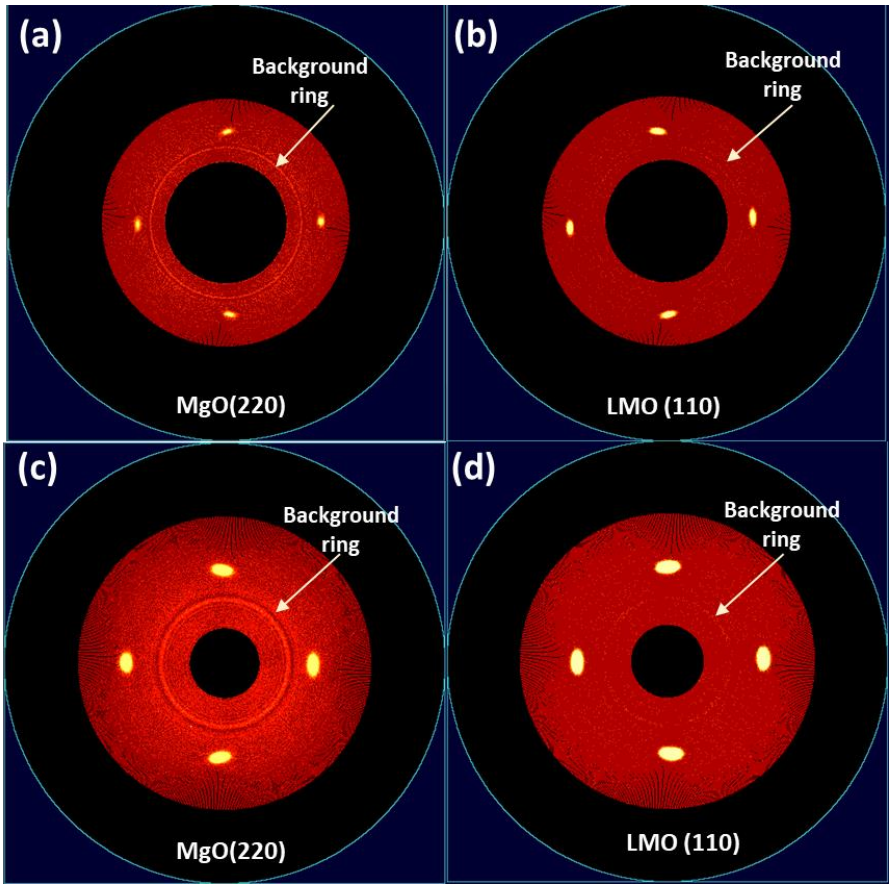

Figure 4.16 Pole figure analysis of epitaxial LMO (110) and MgO (220) on different substrates (a) MgO/IBAD MgO/Hastelloy, (b) MgO/IBAD MgO/YSZ, (c) LMO/MgO/IBAD MgO/Hastelloy, and (d) LMO/MgO/IBAD MgO/YSZ.

Figure 4.16 shows the pole figures of each epitaxial film on different substrates. The pole figures clearly show four symmetry peaks. The peak intensity is also lower for the films grown on the Hastelloy substrate. The background ring may come from the GADDS system since it has been observed in every measurement. No twins were observed. This also indicates excellent film quality.

4.3.2 Investigation of uniformity of buffer layer on surface-planarized YSZ

The uniformity of the buffer layer texture has been checked for quality control purposes. The out-of-plane texture was checked at multiple points via the GADDS. As illustrated in Figure 4.17, multiple points of out-of-plane texture were measured with an XRD system with a 0.5-mm wide shutter. The position of measurement is controlled via a high-resolution 3-axis step moving stage and related laser position indicator.

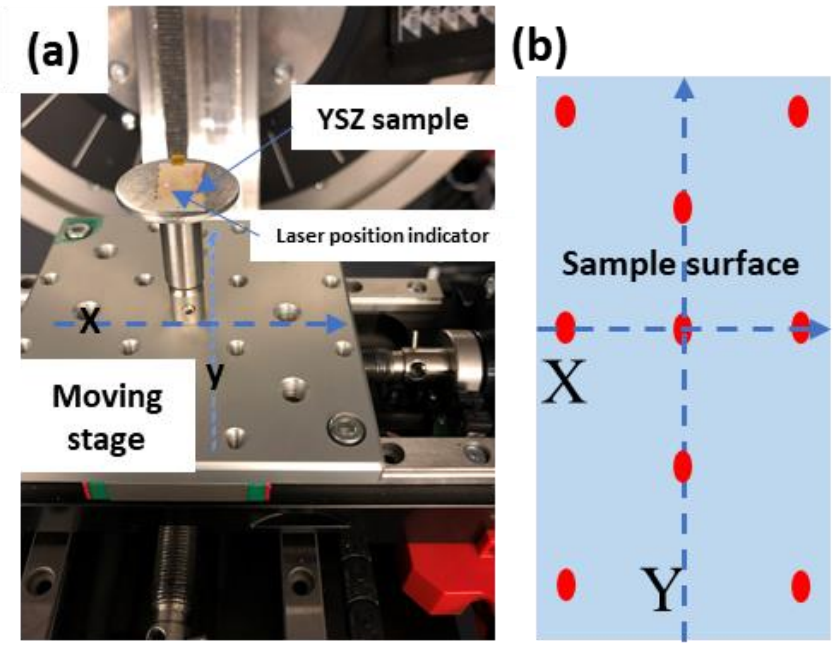

Figure 4.17 (a) XRD moving stage setup, the YSZ sample is place on the sample holder with a XY moving stage; (b)Schematic of the position mark with same coordinate axis on YSZ sample (red dots are XRD measure positions).

A virtual coordinate axis was constructed on the 10 mm × 20 mm YSZ ribbon. The central point and near edge points (2 mm from the edge on X-axis, 5 mm from the center on Y-axis, and four corner positions) were selected for the out-of-plane 2theta scan. The sample used is a 4-layer SOG-planarized YSZ ribbon with homoepitaxial MgO. All the FWHM values of the MgO (200) peaks are summarized in Table 4.4. The sample shows a similar strong texture on all the points. The maximum error is only 3.1%. The uniform buffer on the YSZ surface proves that it qualifies for the REBCO growth.

Table 4.4 Homoepitaxial MgO texture summary on multiple positions on YSZ ribbon.

X axis Position (mm)	MgO (200) Δω	Y axis Position (mm)	MgO (200) Δω	Corner Position (mm)	MgO (200) Δω
0,0	2.365°			4,-9	2.370°
-3,0	2.346°	0,-5	2.397°	-4,9	2.318°
3,0	2.291°	0,-5	2.293°	-4,-9	2.340°
				4,9	2.328°

4.4 Summary

In this work, a biaxially-textured buffer thin-film structure was developed on YSZ ribbon with multiple layers of planarization. A low surface roughness critical for IBAD biaxial texture formation was demonstrated using an appropriate spin-on-glass and an optimized number of coating layers. The assist beam voltage, beam current, and ion exposure (deposition) time were optimized. The optimized parameters of the assist beam during the IBAD MgO growth was found to be V_A=950 V and I_A=110 mA with 40 s of deposition time. Homoepitaxial MgO on this YSZ sample can reach (200) Δω of 2.2º and (220) Δϕ of 4.8º, and the heteroepitaxial LMO texture can reach (001) Δω

of 2.87º and (110) Δϕ of 6.48º. The YSZ remains in good shape after all the buffer layer coating process and is very uniform throughout the entire area.

CHAPTER 5 TEXTURE IMPROVEMENT BY USING HIGH-ORIENTED AG/TIN LAYERS ON IBAD BUFFER

As described in section 1.3.3, Ag is a suitable candidate to improve the texture of biaxially-textured buffer for better single-crystal-like top functional layers. However, there is no report yet on the use of an Ag layer to improve the texture of an HTS REBCO tape. In this chapter, different buffer architecture designs and optimization using Ag/TiN intermediate layers for achieving highly textured REBCO film will be discussed.

5.1 Epitaxial growth of $LaMnO_3$/MgO cap layers on the IBAD MgO substrate with an Ag intermediate layer

A Hastelloy-based IBAD single-crystal-like MgO with a homoepitaxial layer was used as the substrate for Ag and related layer growth. All TiN/Ag layers were grown in an RF magnetron co-sputtering system (co-sputter) with Ag and Ti metal targets. The Ag layer was deposited on the IBAD MgO tape with 100 W RF power at 500 ºC for 15 min. The sample was then annealed at 700 ºC for two hours to remove possible surface pits. The same Ag process for multiple samples was repeated and coated with TiN for the next step. The TiN layer was deposited at 700 ºC with 250 W RF power for 30 min. The final thickness of the Ag and TiN was 320 and 160 nm, respectively. The MgO and $LaMnO_3$ (LMO) films were then deposited on both the Ag/IBAD MgO (AM) and TiN/Ag/MgO (TAM) samples as buffer layers for rare-earth barium copper oxide (REBCO) in the roll-to-roll magnetron sputter deposition system (PRB). The deposition conditions for the TiN and Ag layers were optimized in a previous study [77], so the cap layer texture is the focus of this chapter.

The deposition conditions of the MgO and LMO layer were chosen according to the previously-optimized parameters for oxide buffers [162]. The MgO film was processed at 820 ºC with 1200W MF power and 5 sccm oxygen flow. The tape speed was kept at 3 cm/min during MgO deposition. The LMO film was processed at 850 ºC with 600 W RF power, 4 sccm oxygen, and 2 cm/min tape feed speed. Figure 5.1 shows the XRD θ-2θ scan of the IBAD MgO substrate, Ag/MgO (AM), TiN/Ag/MgO (TAM), and samples after LMO/MgO (LM) buffer layer growth (marked as LM, LMAM, and LMTAM, respectively). The "X" peaks belong to the Hastelloy tape.

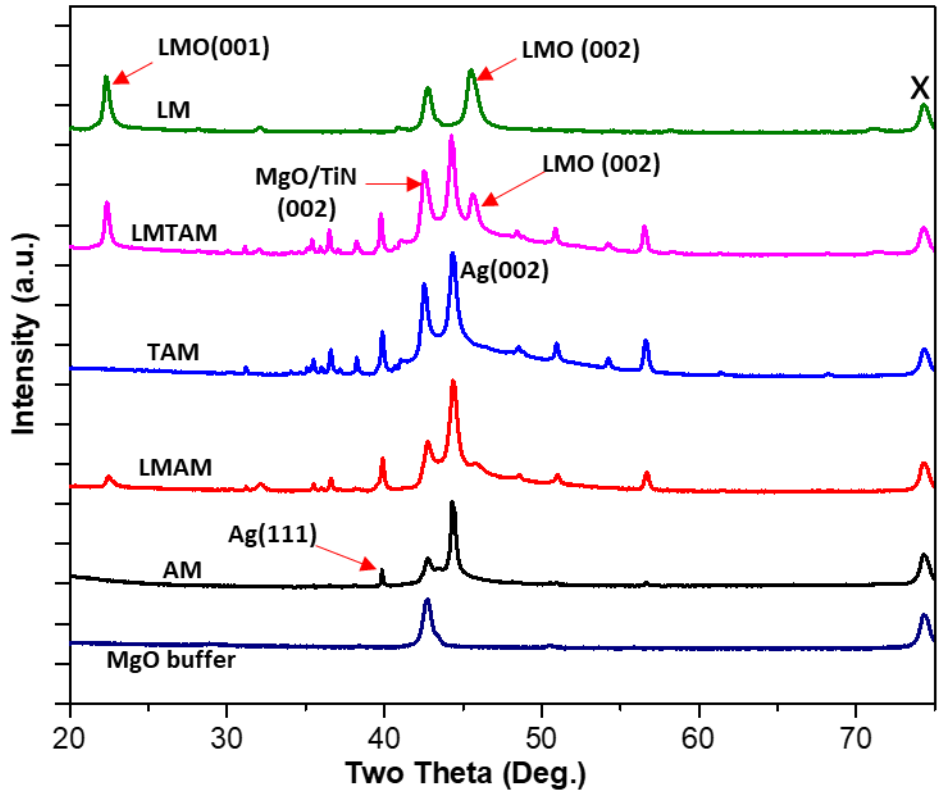

Figure 5.1 XRD θ-2θ scans of LMO/MgO cap layers on different kinds of buffer: MgO, Ag/MgO(AM), TiN/Ag/MgO (TAM). XRD curves of the different buffers are also included.

Both AM and TAM samples showed high-intensity Ag (002) and MgO/TiN (002) peaks. However, the LMO (001) and (002) peaks are very weak when LMO/MgO was

directly deposited on the AM structure. For the LMTAM sample, distinct LMO (001) and (002) peaks were observed, which indicates good epitaxial growth of LMO and MgO was achieved on the Ag with the TiN layer. The top TiN film could have acted as a protective layer for the underneath Ag by blocking possible O_2 diffusion and providing mechanical support during the high-temperature deposition of MgO and LMO.

Several other peaks were also observed in the XRD scan of AM, MAM, TAM, and LMTAM samples. The peak at 38º 2theta angle appeared, which could be Ag (111) since it was observed for the AM sample. Many strained peaks, such as the peaks around 35º, also appeared after TiN/MgO was deposited on the AM sample. Since these peaks were observed only when the Ag layer was introduced (compared with LM XRD curve), the strain in the TiN/MgO films could be due to a large thermal expansion mismatch with the highly-oriented Ag film with a large thermal expansion coefficient. This finding suggests that the growth condition and buffer structure still require further optimization.

5.1.1 TiN/Ag/IBAD MgO (TAM) buffer architecture

The TiN/Ag/MgO (TAM) buffer structure, processed by co-sputter was used for the LMO/MgO cap layers growth. Figure 5.2 (a) and (b) provides the GADDS diffraction patterns of IBAD MgO buffer. The individual MgO (002) peak indicates the c-axis growth of the IBAD MgO buffer, and four-fold symmetric peaks in the MgO (220) pole figure demonstrates the good in-plane alignment of biaxial texture. The (002) out-of-plane texture of 2.34º FWHM and a (220) in-plane texture of 6.42º FWHM, are in the normal texture range of standard IBAD MgO. In the GADDS diffraction pattern of the TAM sample (Figure 5.2 c), both MgO/TiN (002) and Ag (002) peaks showed a narrow

shape along the 2θ and χ direction as a “dot shape”. In a similar manner, four-fold symmetric “dot” shaped peaks were observed on the Ag (220) and TiN (220) pole figures. This finding indicates that the texture spreads of Ag and TiN are extremely small in both the out- and in-plane directions. Also, no ϕ direction rotation was observed from the Ag and TiN pole figures, which indicates that Ag and TiN growth followed the c-axis of MgO buffer. The orientation relationship of TAM buffer architecture can be concluded to be (001)⟨100⟩TiN || (001)⟨100⟩Ag || (001)⟨100⟩MgO.

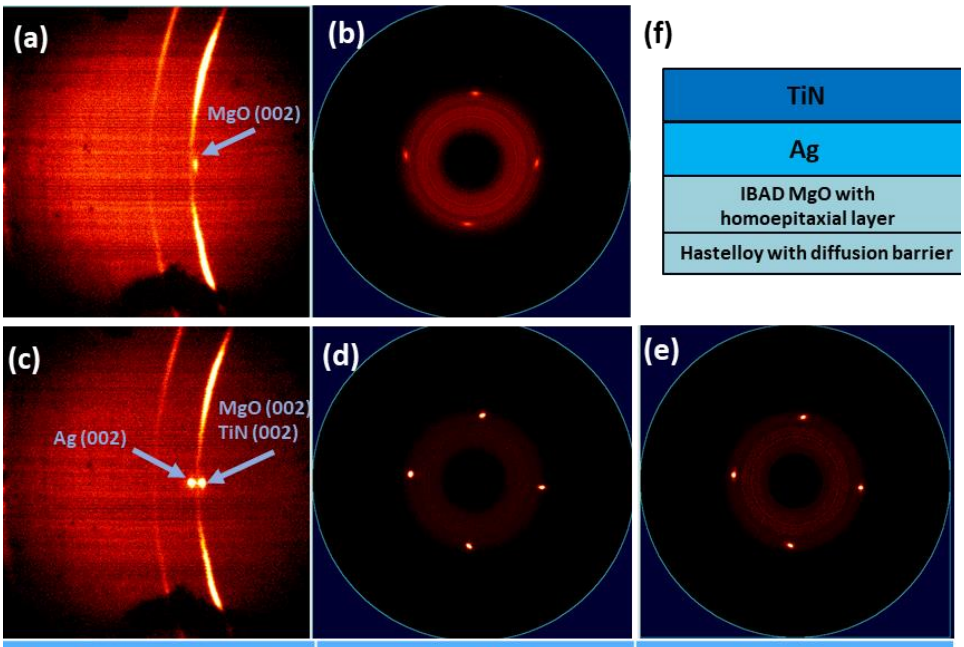

Top layer texture (°)	Δω (002)	Δφ (220)
MgO	2.34	6.42
Ag/MgO	0.56	1.15
TiN/Ag/MgO	0.81	1.69

Figure 5.2 (a) General Area Detector Diffraction System (GADDS) diffraction pattern of MgO buffer; (b)Corresponding MgO (220) Pole figure; (c)GADDS diffraction pattern of TAM; (d)corresponding Ag (220) Pole figure; (e)corresponding TiN (220) Pole figure;(f) TAM architecture and the corresponding texture data.

The TiN texture data listed in Figure 5.2 consists of an overlap of top TiN and bottom MgO since (002) peaks of both films are located at the same diffraction angle.

Nevertheless, both Δω and Δϕ of TiN already reached 0.81º and 1.69º, respectively, which are very small compared with the normal buffer. In general, Ag films coated on IBAD MgO buffers show significant texture improvement, and the TiN layer can duplicate the high-quality texture of the Ag layer.

5.1.2 Epitaxial growth of LMO/MgO cap layers on the TAM buffer architecture

The texture of MgO and LMO cap layer-coated TAM samples is discussed in this section. First, the MgO texture on the TAM samples (MTAM) was investigated as a function of as-deposited MgO thickness. All samples were welded with bare Hastelloy tape and moved during the deposition process at a constantly speed. The deposition conditions followed the same steps as the previous experiment. Two kinds of tape feed speed were applied: (1) 1 cm/min and (2) 5 cm/min, corresponding to approximately 300 and 40 nm in top MgO thickness, respectively. Figure 5.3 shows the GADDS diffraction pattern and in-plane MgO (220) pole figures of the MTAM samples processed at the two tape moving speeds. There is no evident difference observed in the GADDS diffraction patterns of two samples. The Δω of MgO (002) of the 1 cm/min tape and MgO (002) of the 5 cm/min tape are 1.11º and 1.13º, respectively. The Δϕ of MgO (220) is around 1.85º for both samples. There was no significant texture degradation when the MgO film thickness was increased.

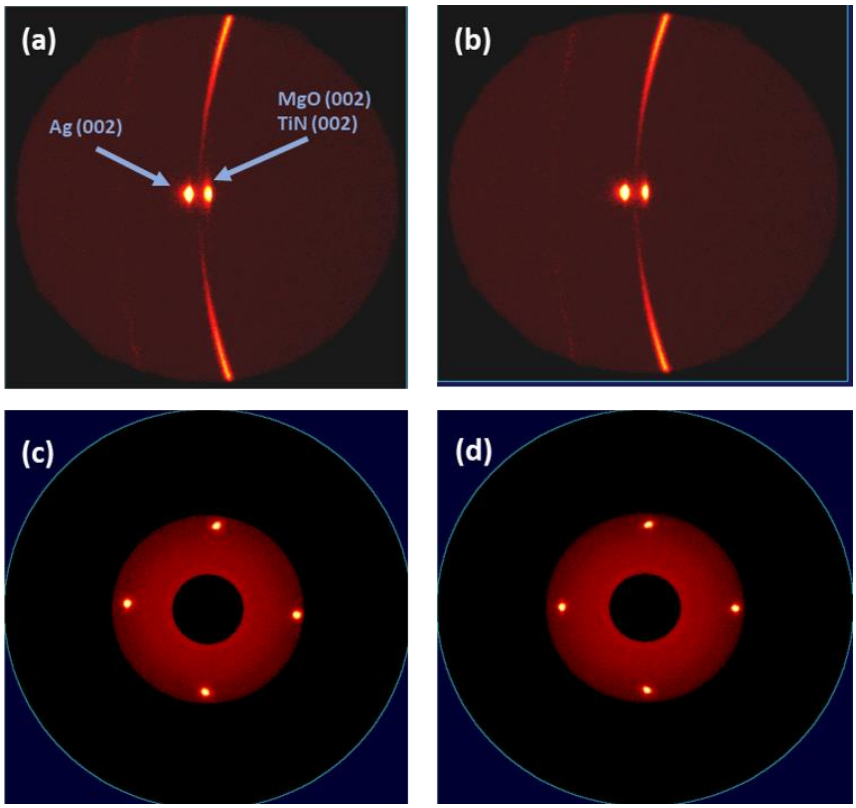

Figure 5.3 GADDS diffraction patterns & MgO (220) Pole figure images of MTAM samples with different thickness of MgO on top: (a) (c) MgO deposited with 1cm/min tape moving speed; (b) (d) MgO deposited with 5 cm/min tape moving speed.

The influence of O_2 flow on the MgO texture was also investigated. Two levels of O_2 partial pressure were used during MgO deposition: (1) 1.5E-4 mbar and (2) 1.2E-4 mbar corresponding to 6.5 and 4.5 sccm O_2 flow, respectively. All samples were processed with a 1cm/min tape moving speed. The sample which was deposited with a higher oxygen flow showed an evident (002) peak spread along the χ direction of the GADDS diffraction pattern (Figure 5.4 a). Larger values of MgO (002) $\Delta\omega$ and MgO (220) $\Delta\phi$ were observed for the MTAM sample, which was processed with high O_2 flow. The high O_2 flow may have affected the TAM surface by forming titanium oxides layers before the MgO growth. In this case, the O_2 flow would need to be limited for roll-to-roll deposition of MgO on the TAM structure. This texture spread was also observed

later on the roll-to-roll-processed MgO on the Ti/MgO (TM) structure samples where no Ag layer was used.

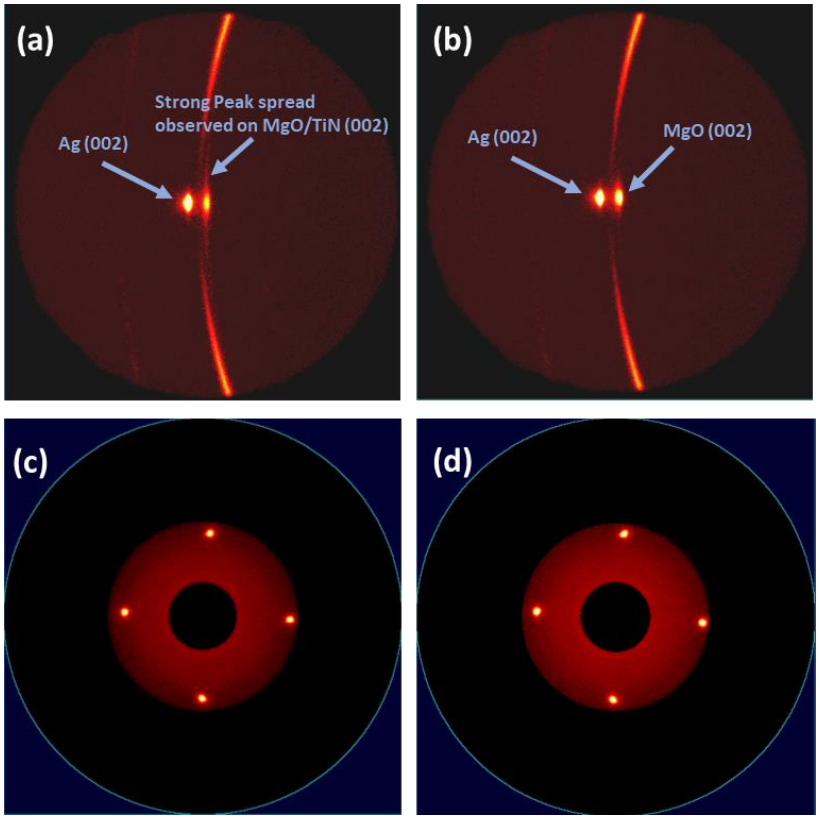

Figure 5.4 GADDS diffraction patterns and MgO (220) pole figure images of MTAM samples with different O_2 flow: (a) (c) MgO deposited with 6.5 sccm O2; (b) (d) MgO deposited with 4.5 sccm O_2

The LMO cap layer texture for the MTAM structure with different MgO thicknesses was investigated in the next step. The previous MgO (process speed 5 and 1cm/min)/TAM was used as the substrate. All LMO layers were processed at 600 W, 850 ºC, and the tape moving speed was maintained at 2 cm/min. In figure 5.5 (b), the GADDS diffraction pattern of the LMTAM sample with a thicker MgO cap layer demonstrated a clear χ direction polycrystalline spread of LMO (002) peak adjacent to the Ag (111) and TiN (111) twins. Since the Ag (111) twins were previously observed in the GADDS diffraction pattern of the annealed AM sample, it is possible that the twin defects originated from the interface between the Ag layer and bottom MgO buffer and

influenced the top layers. On the other side, the 2theta scan of the LMTAM sample with the thinner MgO cap layer also showed a slight LMO (200) peak spread, which indicates the LMO texture was mostly decided by the underneath MgO conditions, such as texture and roughness.

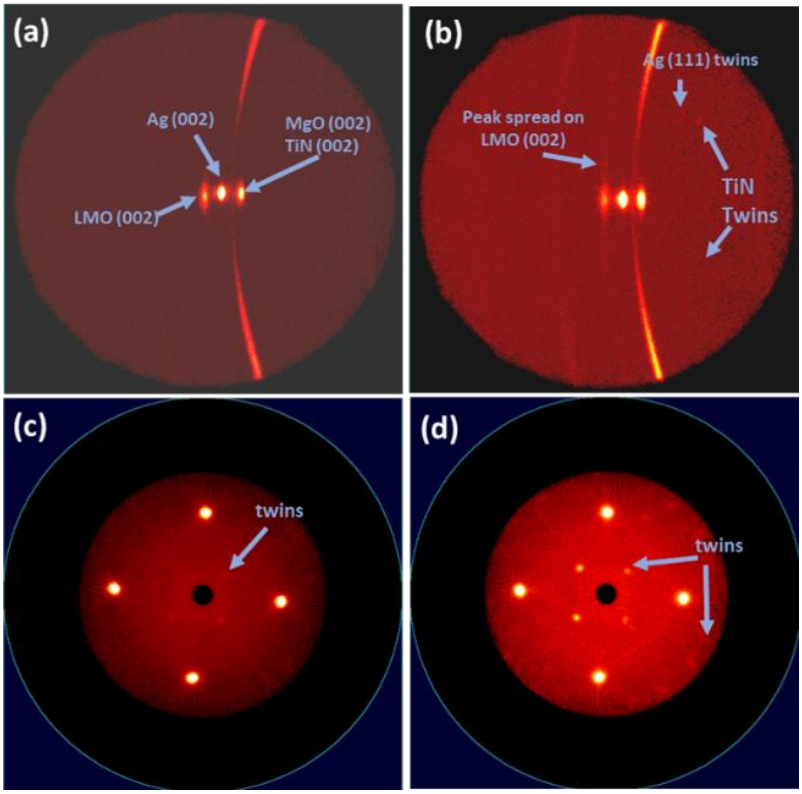

Figure 5.5 GADDS diffraction patterns and lanthanum manganite (LMO) (110) pole figure images of the LMTAM samples with different thicknesses of upper MgO: (a) (c) MgO deposited with 1 cm/min tape moving speed; (b) (d) MgO deposited with 5 cm/min tape moving speed.

Multiple twin peaks were also identified in the LMO (110) pole figures of both samples (Figure 5.5 c and d), and more twins were observed in the LMTAM sample with a thicker MgO cap layer. This finding shows that the LMO texture degraded when a thicker MgO was used. The twin defects that arise from the interface of Ag and IBAD MgO propagated during top layer growth and appeared on the XRD pattern when the MgO cap layer reached a certain thickness.

The texture of LMTAM architecture is summarized in table 5.1 and shows that the LMO on the TAM can still maintain the narrow texture of the Ag layer. Compared with standard LMO on the IBAD MgO buffer layer, the Δω improved from 3.62º to 1.7º, showing a 53% improvement. The Δϕ decreased from 6.64º to 2.807º, showing a 58% improvement. The LMTAM sample with thicker MgO only showed a slight texture deterioration (Δω of 2.15º, Δϕ of 3.04º), but the substantial twin defects could cause problems in REBCO growth.

Table 5.1 Texture data summary of IBAD MgO, AM, TAM, MTAM, LMTAM, and standard LMO

Top layer texture (º)	Δω (002)	Δφ MgO(220)/LMO(110)
MgO	2.34	6.42
Ag/MgO	0.56	1.15
TiN/Ag/MgO	0.81	1.69
M(5cm/min)/TAM	1.13	1.85
LMO/MgO(5cm/min)/ TAM	1.70 (with background spread)	2.81
Standard LMO (No Ag)	3.62	6.64

REBCO deposited by the metal-organic chemical vapor deposition (MOCVD) method requires a higher temperature than that used in the buffer process. Based on this concern, a heat test in the roll-to-roll MOCVD chamber was performed to verify whether the LMTAM structure could survive the REBCO deposition process. The LMTAM sample was loaded into the roll-to-roll MOCVD chamber (M1) and passed through the heating zone at 955 ºC at a speed of 2.1 cm/min.

The sample was checked by optical microscopy and energy-dispersive X-ray spectroscopy (EDS) measurements after the heat test. T

he optical image and corresponding scanning electron microscope (SEM) images are shown in Figure 5.6 (a) and (b). Many bubble-like delaminated regions were observed in the optical and corresponding SEM images. Figure 5.6 (c) exhibits a high magnification image of a delaminated region. The middle layer became unbound from the bottom and humped up during the heating process, which caused cracking of the top layer. EDS measurements were performed on these three points (Figure 5.7).

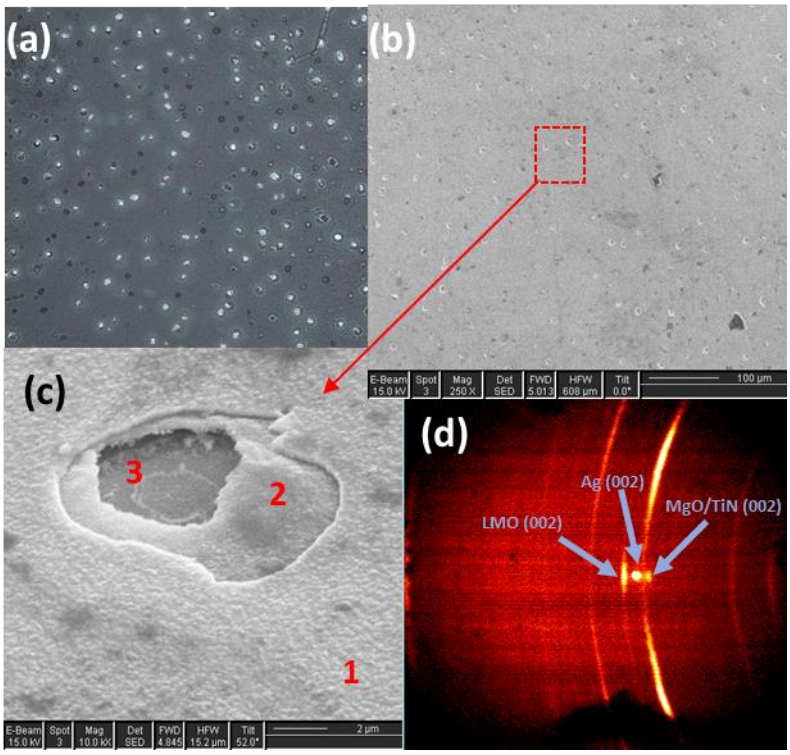

Figure 5.6 (a) optical microscope image of LMTAM sample after heating test; (b) corresponding scanning electron microscopy (SEM) image; (c)high magnification image of the delaminated region; (d)GADDS diffraction pattern of the LMTAM sample after heating test

All elements from the buffer layers could be identified on position one. This finding indicates that the complete LMTAM buffer structure still existed at position one. The swollen middle layer on position two only showed Mg, Ag, and Ti, indicating it may have been the Ti/Ag layer. Position three mostly showed the elements from the Hastelloy substrate (Ni, Mo, Cr, Fe) and Mg, so it could have been the IBAD MgO

substrate. In this case, it is highly possible that the Ag/TiN layer underwent deformation first followed by delamination from the underneath IBAD MgO during the heating process and caused breakage of the top layers due to mechanical deformation. The GADDS diffraction pattern of the sample after the heating test shows a broad peak spread and multiple polycrystal curves, which also confirms that the texture was fully damaged by mechanical delamination (Figure 5.6 d).

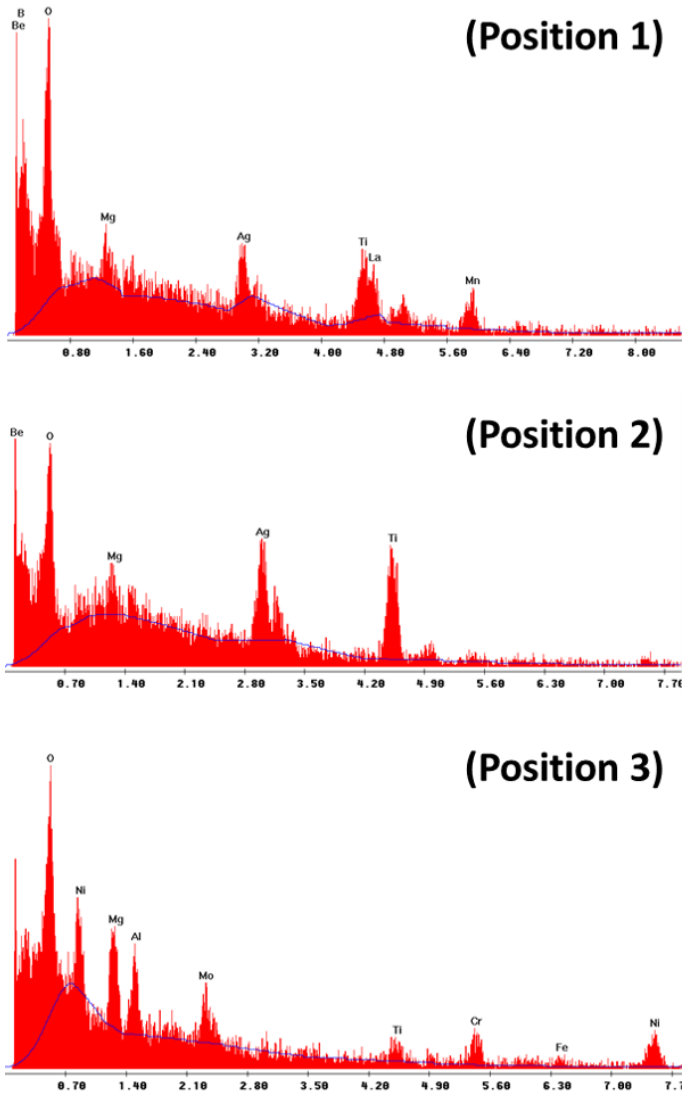

Figure 5.7 Energy-dispersive X-ray spectroscopy (EDS) spectra of three scanned positions as mentioned in figure 5.6.

In summary, the TiN/Ag/IBAD MgO buffer structure could ensure the top LMO and MgO cap layers reached very low texture misalignment. However, a few defects still existed: (1) weak bonding between Ag and underneath MgO could not guarantee that the sample maintained good physical shape during high-temperature deposition of MOCVD REBCO. The twin defects which originated from the Ag/IBAD MgO interface could be propagated to the top layer and counteract the excellent texture by adding second phase twins. Besides that, Mg particles were previously observed on the Ag surface and may have resulted from diffusion from the IBAD MgO, which could cause deterioration of top layers.

5.2 Epitaxial growth of $LaMnO_3$/MgO cap layers on IBAD MgO substrate with an Ag/TiN intermediate layer

In this section, a possible route for optimizing the TAM buffer architecture on IBAD MgO is proposed. Ag/IBAD TiN has been established as a conductive buffer architecture and has been previously demonstrated as a substrate for epitaxial Ge layers. The Ag-TiN structure could provide very strong bonding at the interface, which would yield less chance for thermal deformation and twin formation compared with Ag-MgO structure. In this case, a TiN layer was first deposited on the IBAD MgO as the modification of TAM architecture before the Ag deposition.

A thin TiN layer (35 nm, 5 min deposition at 700 ºC) was deposited on the IBAD MgO before Ag layer deposition. The top TiN and Ag layers were still grown using the same process as the TAM sample. This TiN/Ag/TiN/IBAD MgO (TATM) architecture showed a clear GADDS diffraction pattern, which was free of twins and foreign peaks, in the 2theta range (Figure 5.8 c). Figures 5.8 (b) and (d) show the corresponding

scanning electron microscopy (SEM) surface images of the TAM and TATM with annealed Ag layers, respectively. A smooth surface was observed on the TATM samples instead of a TAM sample's rough surface.

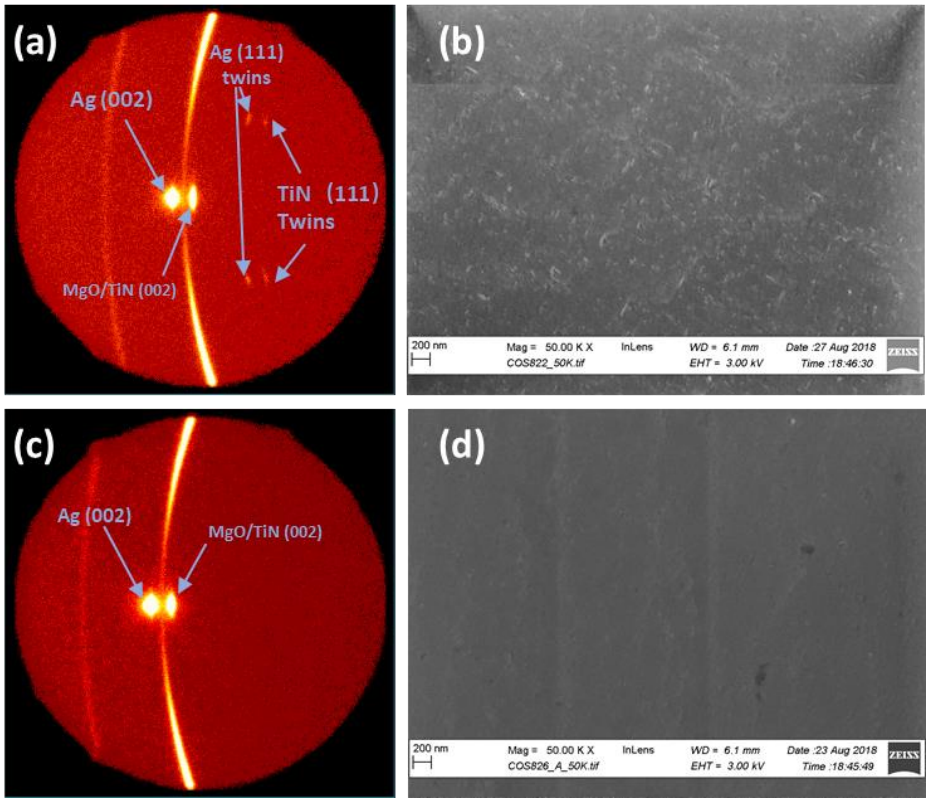

Figure 5.8 GADDS diffraction patterns and corresponding SEM surface image of (a)(b) TAM samples; (c)(d) TATM samples.

The thickness effect of this extra TiN layer has also been investigated. The LMO/MgO cap layers were deposited following previously optimized conditions on multiple TATM samples, which had different thicknesses of the bottom TiN layer. The first row in figure 5.9 shows a log scale GADDS diffraction pattern of TATM samples with 15, 35, 65, and 85 nm bottom TiN layer at the same image contrast. All samples maintained the same out-of-plane texture level as the TAM sample. The GADDS diffraction patterns of these samples after undergoing the same MgO/LMO process is illustrated in the second row of figure 5.9. Other than the normal c-axis Ag(002),

MgO/TiN (002), and LMO (001) (002) peaks, only very weak twins without any peak spread were observed on LMO (001) and (002) peaks. This proved that the a well-textured LMO still could obtained from the underneath Ag layer in the LMTATM architecture.

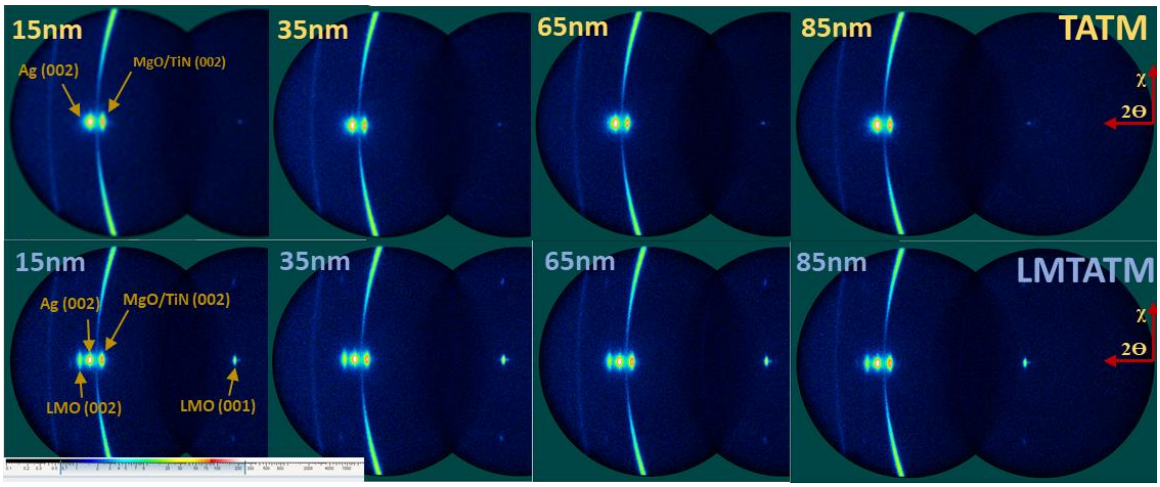

Figure 5.9 GADDS diffraction patterns of TATM and LMTATM samples with different thicknesses of the bottom TiN layer.

Figure 5.10 provides the in-plane texture details of LMTATM samples with different thicknesses of the bottom TiN layer. The first and second rows (from top to bottom) show the GADDS diffraction patterns of TATM and LMTATM samples respectively, when χ angle is set as 54.7º. Clear LMO (011) peaks can be identified after LM cap layers were deposited. Only a very weak polycrystal spread was observed for the samples with 65 and 85 nm thick bottom TiN layers. However, the LMTATM sample shows better in-plane texture since the peak spread is much less when compared with the LMTAM sample (Figure 5.10, bottom row left). This in-plane oriented spread may have been caused by the different thermal expansion coefficients between the MgO and Ag layer. The TiN layer on Ag was subjected to high strain conditions when the TAM sample cools down after deposition. This strain may be released by top films by

misoriented grains. Since the bottom TiN could improve the mechanical strength of the Ag layer and share the strain, much less misoriented grains could be expected when the top film is deposited.

The third row of Figure 5.10 exhibits the LMO (110) pole figure for all samples. An apparent four-fold symmetry can be observed in the pole figures of the LMTATM samples, which were all free of twins. Based on these findings, a 35 nm bottom TiN was employed in subsequent work since the thickness should be enough to block Mg diffusion from the bottom and mechanically support the Ag layer.

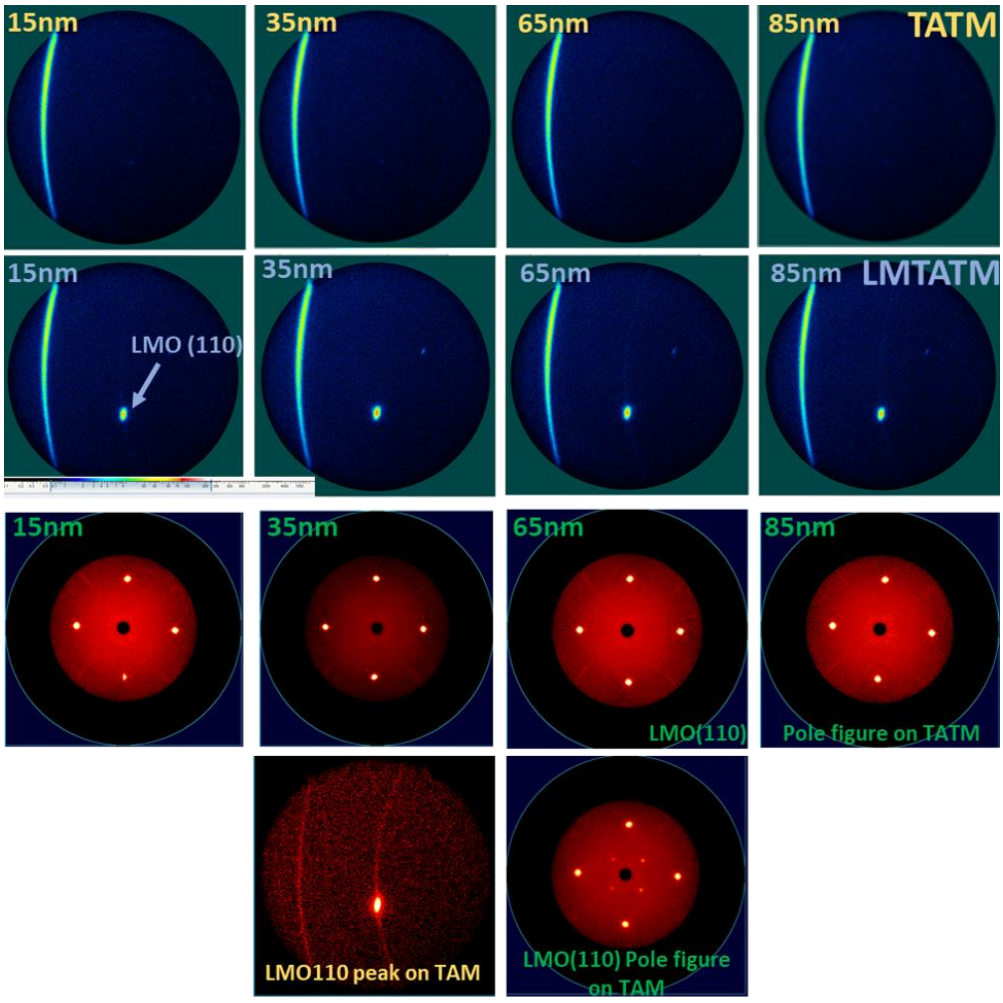

Figure 5.10 Rows 1 and 2:GADDS diffraction patterns of TATM and LMTATM (011) at 54.7° χ with different thickness of bottom TiN film; Row3:LMO(110) pole figures of LMTATM samples with different thickness of bottom TiN film; Row4: GADDS diffraction patterns at 54.7° χ and LMO(110) pole figure of LMTAM

The Δω of the LMO(002) and Δϕ of the LMO (110) in the LMTATM architecture was 1.7º and 2.45º, respectively, with 35 nm bottom TiN. This Δω matches the LMO texture on the TAM buffer. The Δϕ showed a slight improvement from 2.85º to 2.45º. The successful of use of bottom TiN is also promising for replacement of the IBAD MgO by IBAD TiN as the bottom buffer, which would simplify the structure and also maintain the good mechanical strength of the whole architecture.

5.3 Geometric optimization of TATM buffer structure for high-temperature REBCO MOCVD process

The Ag on the edge of Hastelloy tape could electrically couple to the substrate in ohmic heating in the REBCO MOCVD process which will alter the resistance and current path. So, a mask was designed and applied in the TiN/Ag deposition process to isolate the Ag layer laterally from the Hastelloy tape edge. In this way, the Ag layer could be encapsulated by the TiN/MgO film from both lateral and vertical directions. Figure 5.11 illustrates the whole deposition process of the LMTATM sample when the mask applied. A specific shape of the mask was cut with a laser from a standard LMO-buffered Hastelloy tape which was then mounted on the IBAD MgO substrate before Ag deposition. The LMO buffer side of the mask keeps faced downward on the IBAD MgO tape during the whole deposition process to ensure no metal elements of the Hastelloy diffused onto the growing film. The mask can be removed either after the Ag layer or after top TiN layer deposition since both layers were processed in the same sputter system. In method 1 (Mark as Md1) route shown in figure 5.11, the mask was removed after Ag layer deposition so that the TiN layer could encapsulate the whole Ag.

In method 2 (Mark as Md2) route, the mask was removed after the TiN process so that the TiN/Ag would not reach the edges of the MgO layer.

Figure 5.12 (d) shows the TATM sample by Md1. The TiN layer covers the edge side of this sample. The sample in Figure 5.12 (e) processed by Md2, which only has MgO on edge. Figure 5.12 (f) illustrates both kinds of the sample after the LMO/MgO process, which indicates the TATM structure buffer still maintained its good shape after all buffer processing.

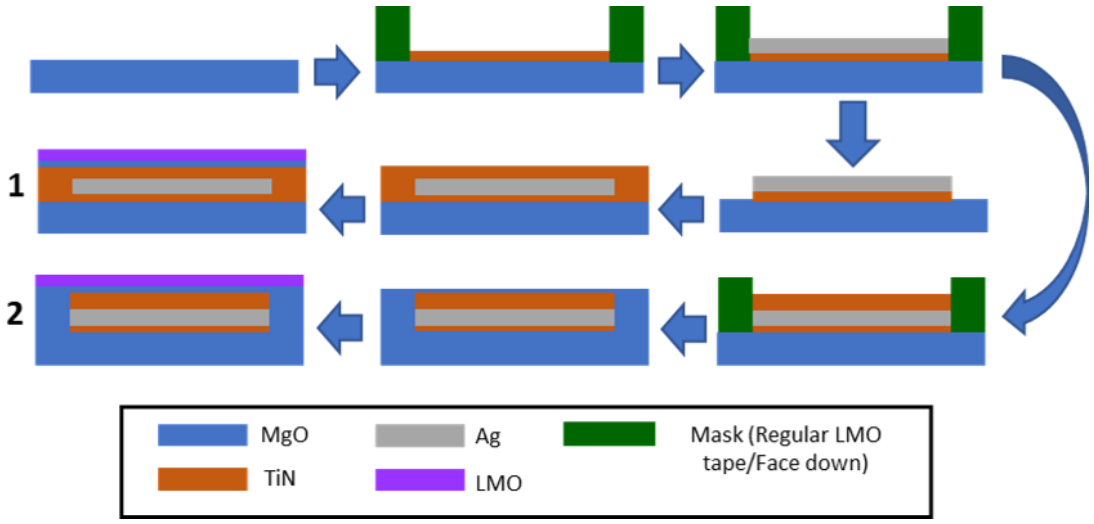

Figure 5.11 Schematic diagram showing the two fabrication routes of LMTATM sample when a mask was applied.

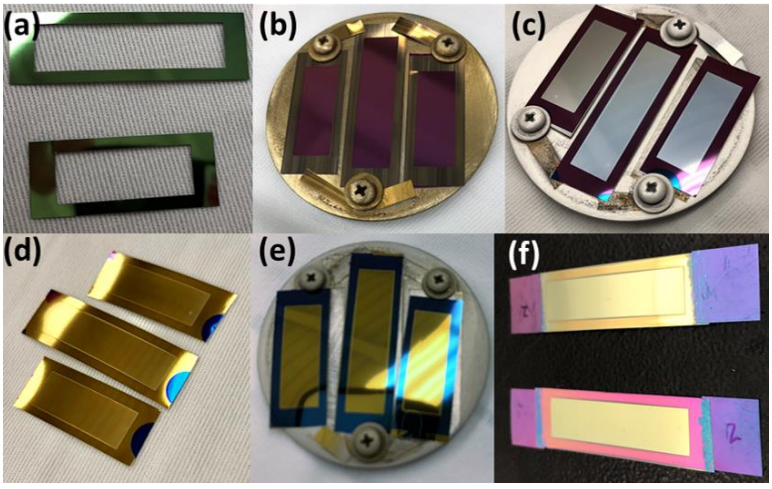

Figure 5.12 (a) Mask design for two kinds of size sample (b) IBAD MgO mounted with a mask before deposition (c) AM process when mask applied (d) TATM sample by Md1 method (e) TATM sample by Md2 method (f)top: LMTATM by Md1 method; bottom: LMTATM by the method

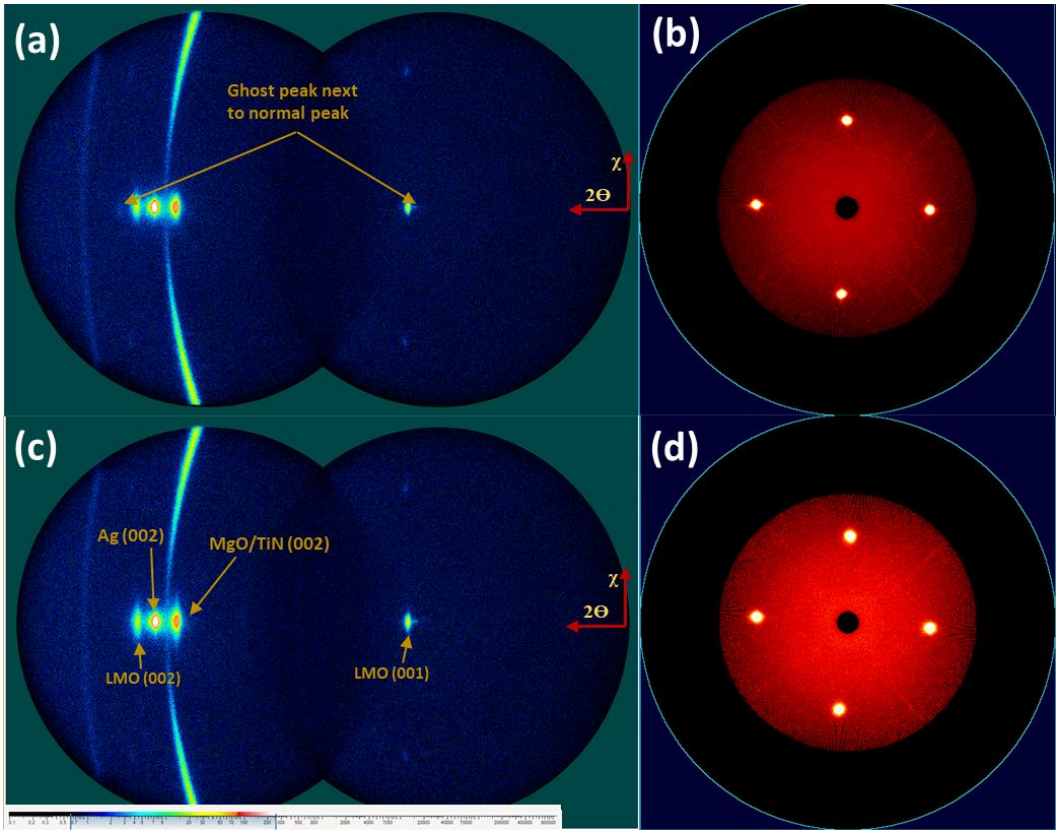

Figure 5.13 GADDS diffraction patterns and corresponding LMO (011) pole figure of (a)(b)Md1 LMTATM; (c)(d)Md2 LMTATM

The texture of both kinds of samples was also examined after cap layer deposition. Figure 5.13 shows the 2theta GADDS diffraction patterns and LMO (011) pole figures of Md1 LMTATM and Md2 LTATM. All XRD scans were performed in the middle part of the sample, where the mask did not cover the sample. All peaks showed similar texture spread compared with the regular LMTATM sample. However, dot-like ghost peaks near both LMO (001) and (002) peaks appeared. These peaks occasionally showed up before for the regular LMTATM sample (Figure 5.9). The SEM pictures in figure 5.14 provide a possible explanation for these weak peaks. Figure 5.14 (a) and (d) are SEM images of Md1 and Md2 TATM sample surfaces, respectively. Many small pits could be observed on the surface. The Ag grains grown on the TiN could not fully coalesce and left pits until the Ag film reached a certain thickness or treated with post-

deposition annealing. Figure 5.14 (c) and (e) shows both samples after the MgO deposition. It can be seen that the pits were by the secondary phase and propagated to the top of the LMO surface (Figure 5.14 c and f). These misoriented grains could have grown from the position of the pit, and are likely reflected by the ghost peaks in the GADDS pattern. The mask mounted on top could change the thermal condition of the sample surface during the TiN/Ag deposition process, which means the deposition condition developed for the normal TATM sample may not be appropriate. The TiN/Ag layer still needs to be optimized by an appropriate annealing process when a mask is applied.

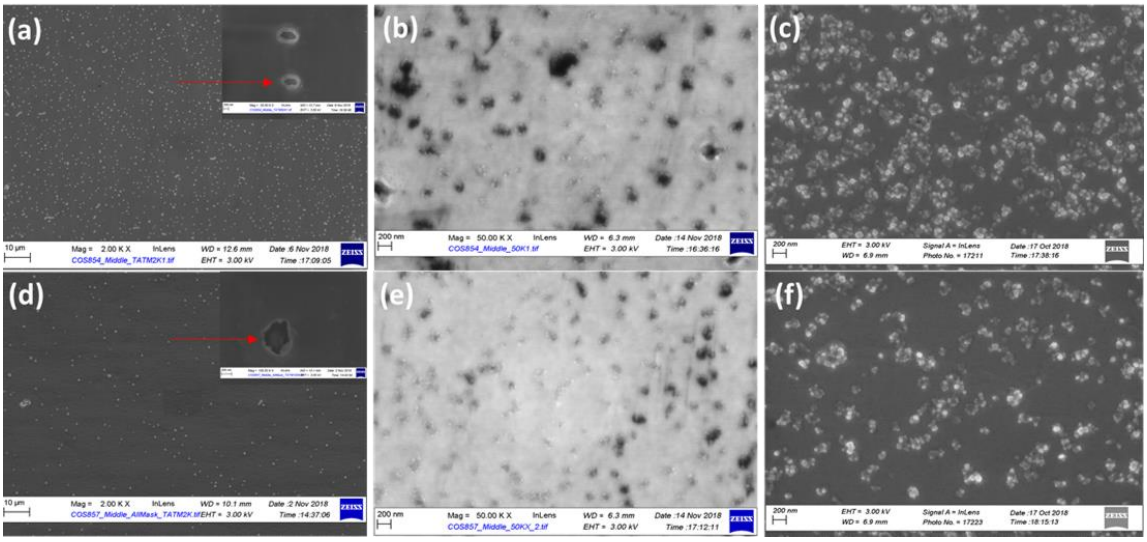

Figure 5.14 SEM images of (a)Md1TATM (b) Md1 MTATM (c) Md1 LMTATM (d) Md2TATM (e) Md2 MTATM (f) Md2 LMTATM.

Besides the texture issue, mechanical delamination still could happen when the masked LMTATM sample is used for REBCO deposition in the ohmic heating roll-to-roll MOCVD system. Both kinds of mask samples were loaded into the roll-to-roll MOCVD (PM) for REBCO deposition. The sample was heated using the ohmic heating method. Figure 5.15 (a) and (b) shows the optical and corresponding SEM images, respectively, of the Md1 LMTATM sample after the YBCO process. The cross-section

of a delaminated region prepared by focused ion beam (FIB) milling reveals that the Ag layer was split into two parts attached to the top and bottom TiN layers. Besides that, the roll-to-roll MOCVD process way could have created scratches on the LMTATM buffer structure. The delaminated region shown in figure 5.15 (c) occurred mainly along the scratch line. The scratch line on the sample surface may have caused localized Ag deformation and evolution into delamination during the heating process.

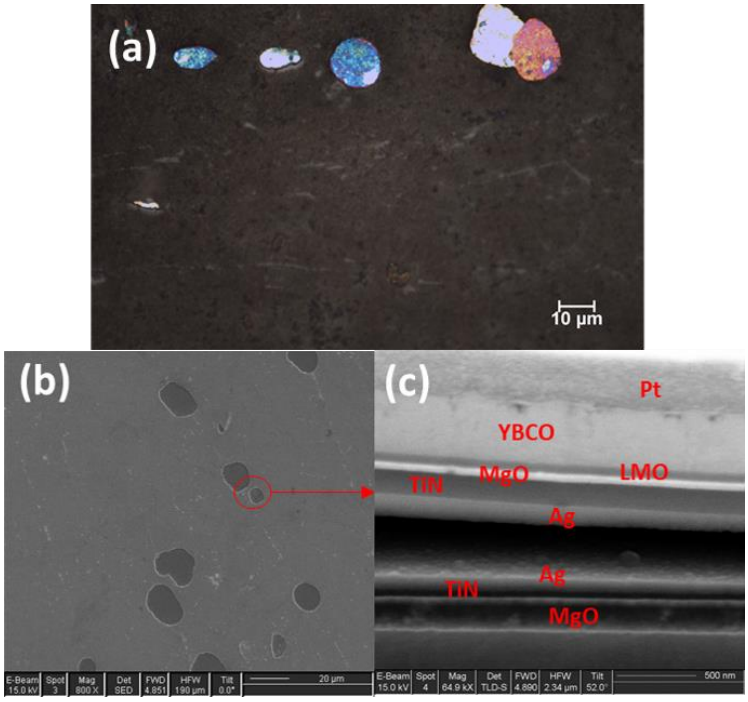

Figure 5.15 (a) Optical image of Md1 LMTATM after MOCVD YBCO process (b) SEM image of delaminated region; (c) corresponding cross-section by focused ion beam (FIB)milled region

5.4 Epitaxial growth of $LaMnO_3$/MgO cap layers on IBAD MgO substrate with a TiN intermediate layer

A single TiN intermediate layer was tested in this study for buffer texture improvement. The TiN layer was deposited on IBAD MgO in the co-sputter system using the same parameters as described previously. The thickness of the TiN was controlled at 160 nm, which was the same as the top TiN layer thickness in the TAM

sample. LMO/MgO cap layers were also processed with optimized conditions, as previously described.

The influence of the O_2 level on the quality of the top MgO layer was investigated. Figure 5.16 (b) and (c) shows SEM images of MgO/TiN/MgO (MTM). The top MgO layer was deposited with two different O_2 partial pressures: 1.5E-4 mbar and 1.2E-4 mbar O_2 (marked as MTM1 and MTM2, respectively). The TM sample surface appeared flat under low magnification and showed a wrinkle-shaped grain in a high magnification image (Figure 5.16 a). In Figure 5.16 (c), a flat surface with fine MgO grains was observed in the MTM2 sample. However, the surface became very rough, and larger grains emerged when high O_2 was used. Since both samples underwent an identical MgO deposition process, it is possible that higher O_2 flow altered the TiN surface conditions during the beginning stages and more O atoms were created for the purpose of MgO nucleation. Besides that, higher O_2 partial pressure could have caused a decrease in the mean free path of ions in the plasma, creating an excessive collision, which could have then impeded the ion migration, producing a rough surface.

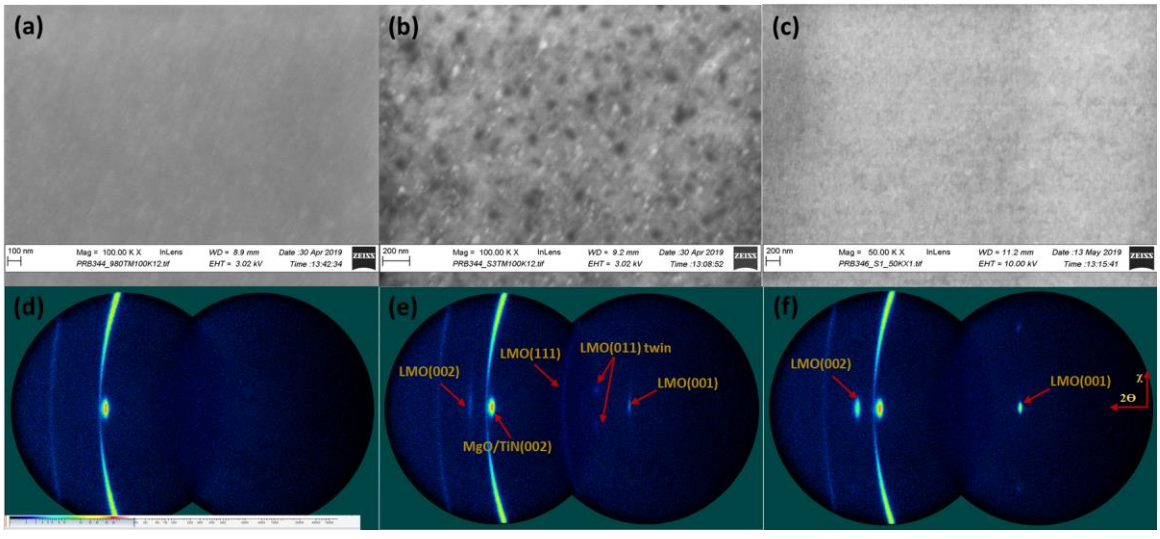

Figure 5.16 SEM images of (a) TM (b) MTM1 (c) MTM2; GADDS diffraction patterns of (d)TM; (e) LMTM1; (f) LMTM2.

Figure 5.16 (e) and (f) illustrate the GADDS diffraction patterns of both MTM1 and MTM2 after the LMO deposition, respectively. Both samples show similar texture spread of the MgO/TiN (002) peak despite the different surface morphologies, while a very different LMO texture emerged after identical LMO deposition processes on both samples. LMTM1 showed broad LMO (001) and (002) peaks with polycrystal spread but LMTM2 showed very sharp LMO peaks. Also, the LMO (011) twins at 32º and LMO (111) polycrystal ring seen in LMTM1 indicates that some LMO grains tilted and did not follow c-axis growth. In brief, LMO growth on rough MgO surface could have created more misoriented grains, which caused the deterioration in the LMO texture.

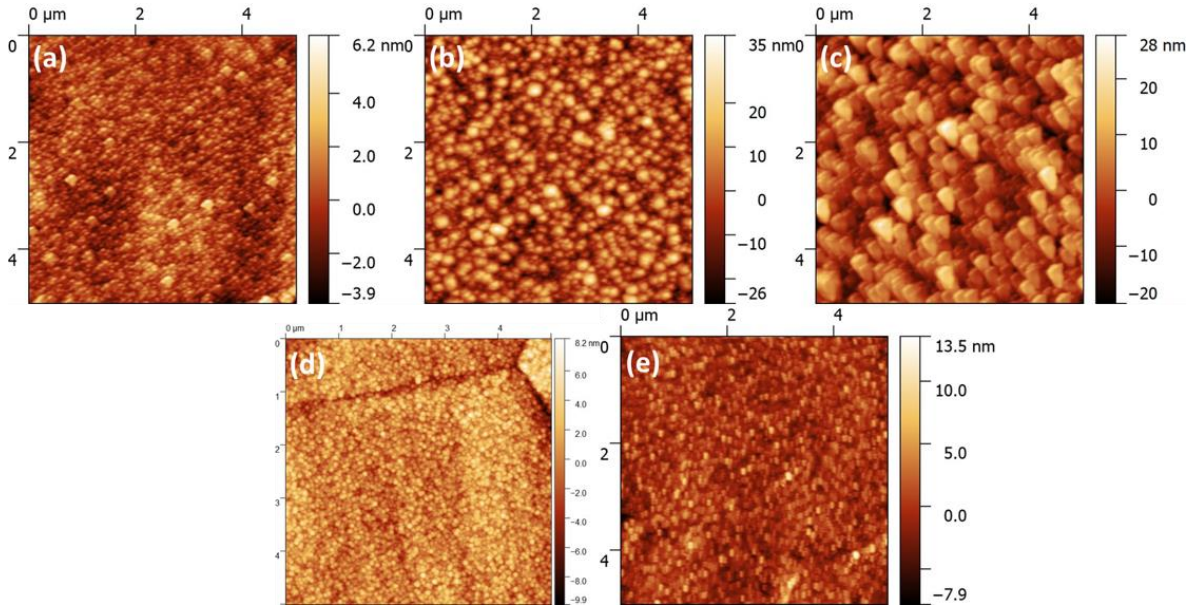

Figure 5.17 AFM surface morphology of (a)TM; (b)(c) MTM1; (d) IBAD MgO (e) homoepitaxial MgO/IBADMgO.

Figure 5.17 (a)-(c) shows the AFM surface morphologies of TM and MTM, respectively. Many small wrinkle-shaped grains and a few coalesced grains could be identified on the TM substrate (Figure 5.17 a), which fits with the SEM image (Figure 5.16 a). Two kinds of surface morphologies were identified on MTM1 sample, which was processed with high O_2 flow. Both of them show much larger grains, and the

corresponding RMS roughness values were 8.60 and 7.85 nm, respectively. Both values are much higher than the TM surface roughness (1.08 nm). A similar roof tile morphology (Figure 5.17 c) was observed by Xue [71] on the MgO surface during the IBAD process where MgO islands may have undergone tilting caused by the ion beam which is aligned at an angle to the substrate. Based on the better surface and texture quality, 1.2E-4 mbar O_2 partial pressure was used for further MgO processes.

Figure 5.17 (d) and (e) shows the surface morphology of the IBAD MgO before and after the homo-epitaxial MgO deposition, which was under the same conditions as MTM. The surface roughness was maintained at 1.8 nm, and fine MgO cubic grains can be seen. The homoepitaxial growth of MgO showed a much smaller grain size compared with the MgO/TiN process, which may have been due to the different surface energy of TiN. MgO growth on TiN may have happened more rapidly.

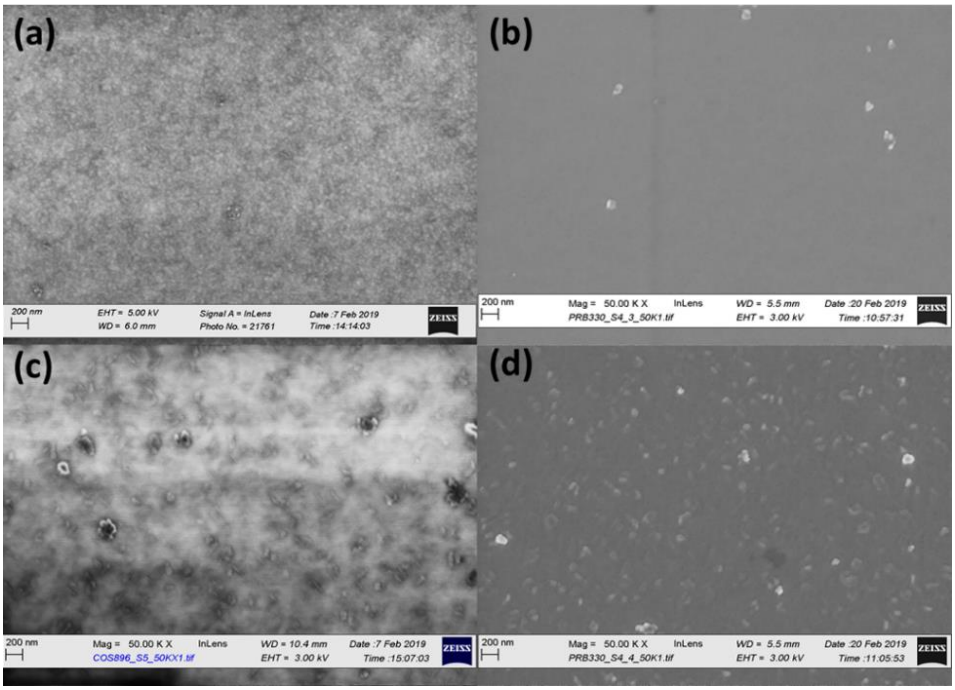

Figure 5.18 SEM images of (a)MgO on TM with 5cm/min tape moving speed; (b)corresponding LMTM; (c)MgO on TM with 1cm/min tape moving speed; (d)corresponding LMTM

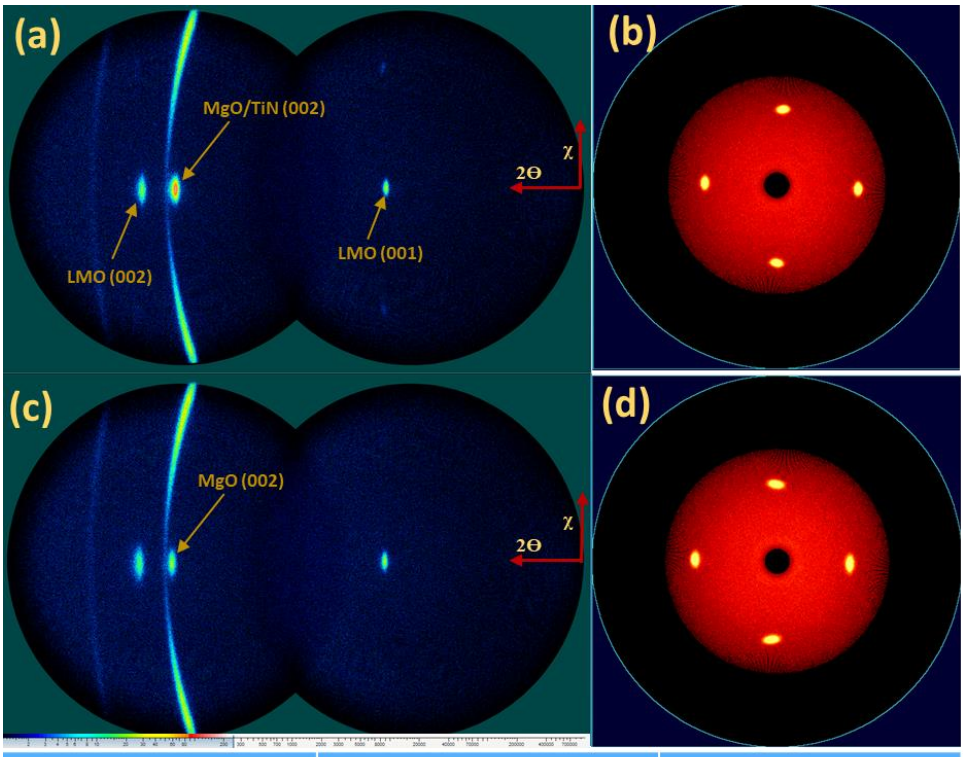

Top layer texture (°)	Δω (002)	Δφ MgO(220)/LMO(110)
IBAD MgO	2.34	6.42
TiN/MgO	1.75	5.32
LMO/MgO(5cm/min)/ TM	2.20	4.55
LMO/MgO(5cm/min)/ IBAD MgO	2.82	5.85
Standard LMO (No Ag)	3.62	6.64

Figure 5.19 (a) GADDS diffraction patterns of (a) LM(5cm/min)TM; (c) GADDS diffraction patterns of LMO/homoepitaxial MgO/IBADMgO; (b)(d)corresponding LMO(110) Pole figure respectively. All the corresponding texture data is listed below.

The surface morphology of MgO with different thicknesses was also investigated. MgO was deposited on the TM buffer at two different speeds: (1) 5 cm/min and (2) 1 cm/min corresponding to thicknesses of 55–70 and 300–400 nm, respectively. Figure 5.18 (a) and (c) shows the SEM images of both MTM samples. The surface became rough and consisted of a few misoriented grains when MgO became thicker. Abundant misoriented grains were observed after the sample was coated with LMO (Figure 5.18

d), which is consistent with the LMO polycrystalline spread in the GADDS diffraction pattern. In contrast, the LMO grown on thin MgO/TM showed a much flatter surface with only a few particles (Figure 5.18 b).

Figure 5.19 (a) and (b) shows a distinct, sharp GADDS diffraction pattern of LMTM sample with optimized MgO conditions. Figure 5.19 (c) and (d) provides texture information of the reference LM/IBAD MgO sample that was prepared via an identical LM process. The homoepitaxial MgO growth appears to provide reasonably good quality biaxial texture. However, the extra TiN layer led to an improvement of the LMO $\Delta\omega$ from 2.82º to 2.2º, a 22% improvement. The in-plane texture also changed from 5.85º to 4.55º at the same time. Besides that, LMO still can maintain a smooth surface when optimized MgO was used on the TM buffer.

5.5 Summary

In this chapter, thin film architectures using Ag and TiN to develop highly biaxially-textured REBCO buffer was described. Different buffer structures based on Ag were tested for LMO/MgO cap layer growth, and TAM was selected as the candidate because of good mechanical bonding between TiN and Ag and the similar crystal structures of TiN and MgO. The LMO/MgO cap layers deposited on the TAM buffer architecture appears to achieve an excellent texture by optimizing MgO thickness and O_2 partial pressure. The final LMO can achieve a $\Delta\omega$ of 1.7º and $\Delta\phi$ of 2.8º on the TAM architecture. However, this architecture still has flaws since LMO (002) and (110) peaks showed texture spread in two-dimensional (2D) XRD scan. Besides that, Ag (111) and TiN (111) twins were also observed, which caused film texture degradation. The

debonding of TiN/Ag from the IBAD MgO substrate during the heating test of the LMTAM structure introduced the necessity for further optimization of Ag buffer.

Another TiN layer was employed in the TAM structure before Ag deposition. The thickness of this TiN layer was optimized to ensure that a smooth top surface could be achieved and block Mg diffusion simultaneously. Ag and TiN (111) twins can be avoided, and no significant peak spread was observed on the final LMTATM GADDS diffraction pattern.

The TATM architecture was also optimized by using a mask method to prevent the Ag film from suffering lateral damage. However, the pits on the Ag layer caused second phase growth on the buffer. Further when REBCO was grown by MOCVD on the masked LMTATM sample, the Ag was found to delaminate from the middle, which suggests the stationary, low-temperature REBCO deposition method may be favorable since the mechanical strength of Ag is low.

Further, a more simplified TM architecture was tested for buffer texture improvement. The MgO layer deposited on TiN tended toward a rough surface if a higher deposition rate was used, which matched the finding from MTAM sample. Appropriate tape moving speed and O_2 level are essential for realizing smooth surface MgO on a TM structure. The final LMO texture improved by around 20% when 160 nm TiN intermediate layer was used. This good-textured LMO with a flat surface should also be a good candidate for future REBCO deposition.

CHAPTER 6 BIAXIAL-TEXTURED EPITAXIAL GALLIUM OXIDE THIN FILMS ON LOW-COST, FLEXIBLE METAL SUBSTRATE

6.1 Epitaxial growth of β-Ga_2O_3 on IBAD MgO

Single-crystalline-like MgO film made by roll-to-roll continuous IBAD process on different low-cost, flexible substrates has already been implemented in superconducting [36], photovoltaics [53], and flexible electronics applications [55]. β-Ga_2O_3 thin films grown on this low-cost, flexible, metal substrate could provide a novel possible pathway for large-scale manufacturing of low-cost UWBG devices on a flexible substrate, which could also address the thermal management issue of UWBG devices.

Epitaxial growth of β-Ga_2O_3 has been demonstrated on various kinds of substrates in the past decades—for example, differently oriented sapphire [163], differently oriented β-Ga_2O_3 wafers [164], silica glass [165], YSZ [166], and MgO wafers of different orientations [167]. Different deposition methods such as molecular beam epitaxy (MBE) [168], pulsed laser deposition (PLD) [169], atomic layer epitaxy (ALE) [170], halide vapor phase epitaxy (HVPE) [164], and chemical vapor deposition (CVD) [171] have been employed, and the specific processes /systems have been optimized to grow β-Ga_2O_3 film with better quality and less defects. However, most deposition processes mentioned above still have some issues, such as low deposition rates and high costs.

Heteroepitaxial growth of β-Ga_2O_3 on cubic MgO wafers of different orientations was demonstrated by Víllora in 2006 [172] and was later investigated in detail and confirmed by Kong [173], Mi [174], Matsuo [175], and Nakagomi [176] using different deposition methods. In these studies, (100), (111), and (110) oriented MgO wafers were

employed as substrates for β-Ga_2O_3 growth and β-Ga_2O_3 of different orientations was demonstrated. Replacing the MgO wafer with MgO-capped Hastelloy tape provides benefits such as flexibility, compatibility with low-cost roll-to-roll process, and high thermal conductivity. Hastelloy-based (100) oriented biaxial textured IBAD MgO film with the homoepitaxial layer was used as the substrate for β-Ga_2O_3 growth in this work. The crystal orientation relationship between the IBAD MgO and heteroepitaxial β-Ga_2O_3 will be discussed in detail.

6.1.1 Experiment setup

The epitaxial β-Ga_2O_3 layer was grown in a roll-to-roll RF sputter deposition system with an undoped Ga_2O_3 ceramic target (99.99% purity). A schematic of the system is shown in Figure 6.1. The system contains few subsystems, including the roll-to-roll tape moving system with tension, speed control; a pressure control system with pressure controller and throttle valve; a vacuum system with rough pump and turbopump; a gas flow system with two separate gas flow controllers for Ar and O_2, respectively; a heating system with 13 halogen lamps with power supply and temperature controller, and a K type thermocouple-integrated susceptor to transfer the heat to the substrate and provide temperature feedback; and finally, an RF sputter source with a related matching box to provide 500 W maximum power. Besides that, few sensors (e.g., ion gauge, residual gas analyzer [RGA]) were used to monitor the chamber vacuum and gas conditions.

IBAD MgO with a homoepitaxial MgO layer was loaded into the system as the substrate. The samples were processed through the 12 cm deposition zone at a certain speed. Different heater temperatures, tape moving speeds, and deposition pressures have been investigated for β-Ga_2O_3 texture optimization. Besides that, the IBAD MgO

substrate with different thicknesses of homoepitaxial layers have also been tested for β-Ga_2O_3 growth. The specific growth conditions will be illustrated in each section. All samples were processed with at least 4 hours of pre-sputter. The RF power is maintained at 300 W for the entire deposition process. After the deposition and cooldown, the samples are removed for the next characterization step.

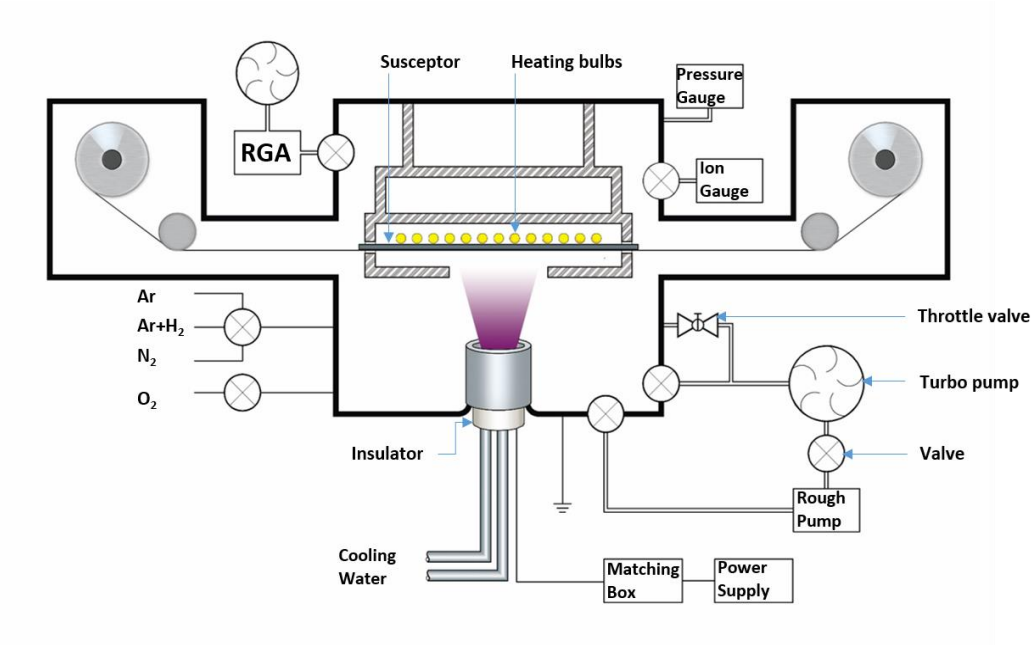

Figure 6.1 Schematic of roll-to-roll radio frequency (RF) magnetron sputter deposition system

6.1.2 Epitaxial growth of β-Ga_2O_3 on IBAD MgO as a function of the deposition temperature

The growth of β-Ga_2O_3 has been studied at deposition temperatures of 500 ºC, 600 ºC, 700 ºC, and 800 ºC. All samples were processed with 1.15 sccm O_2 flow within an Ar atmosphere. The chamber pressure was maintained at 31 mTorr during the deposition process. The samples passed the 12-cm deposition zone at a speed of 1.4 cm/min.

The tape remains flexible and has a shiny surface after the deposition process, as illustrated in figure 6.2 (c). The XRD θ-2θ scan of β-Ga_2O_3/IBAD MgO with different deposition temperatures has been demonstrated in Figure 6.2 (a). The β-Ga_2O_3 (400)

peak, which is located at a 30º two-theta angle, shows ascending intensity when the deposition temperature increases. The peaks labelled "X" belong to the Hastelloy tape. The (400) peaks match with previous reports from other research and demonstrate that out-of-plane (100)-oriented epitaxial growth of β-Ga_2O_3 could be achieved on the biaxially-textured IBAD MgO buffer. The (400) peak intensity is nearly doubled when the deposition temperature reaches 800 ºC. Besides that, the knee at the MgO (002) peak may indicate the development of the β-Ga_2O_3 (600) peak, which also confirms (100)-oriented epitaxial growth of β-Ga_2O_3 on MgO (100) plane. However, the peak intensity remains low compared with MgO, which means the growth process needs further optimization.

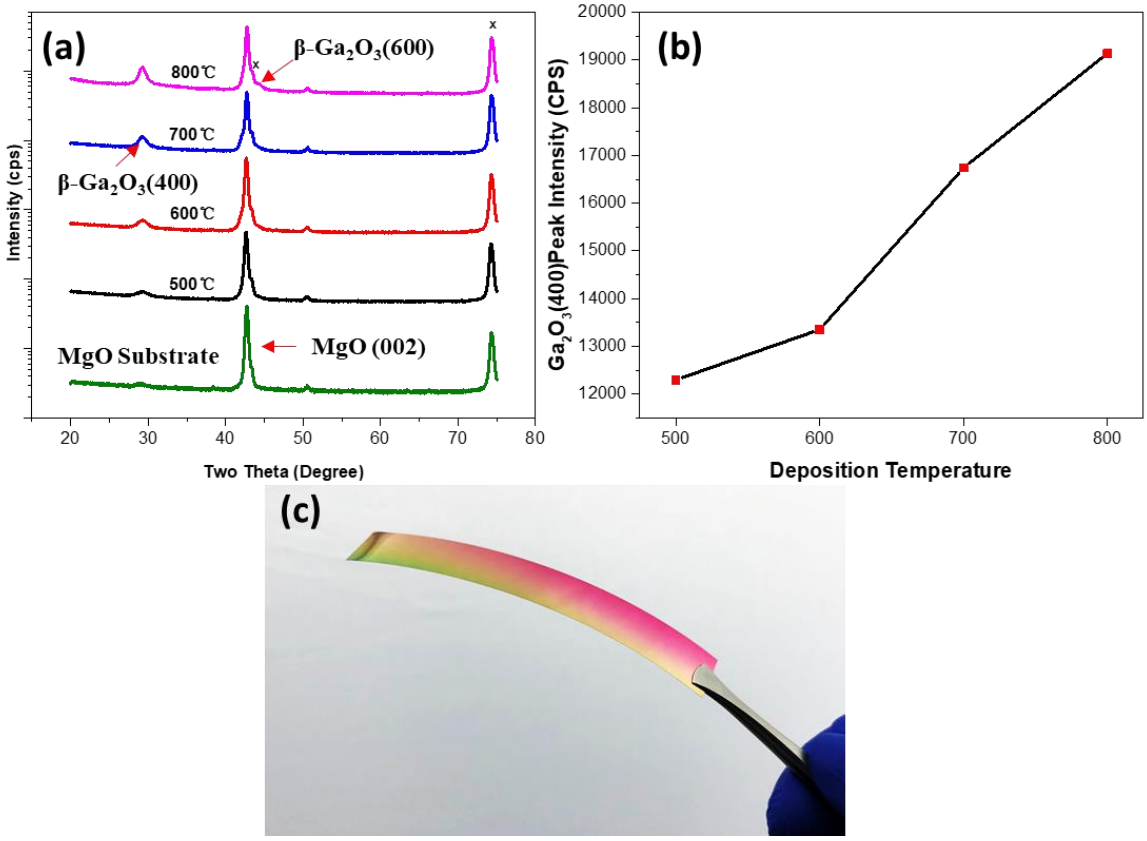

Figure 6.2 (a) XRD θ-2θ scan of β-Ga_2O_3 deposited on IBAD MgO at different temperatures; (b) β-Ga_2O_3 (400) peak intensity changes with temperature; (c) Photograph of β-Ga_2O_3 coated IBAD MgO on flexible Hastelloy tape.

Further experiments of β-Ga_2O_3-deposited on MgO shows that the higher temperature is more favorable for achieving a better-textured β-Ga_2O_3 film. Figure 6.3 shows the rocking curve of the β-Ga_2O_3 (400) peak of samples processed at 820 ºC, 840 ºC, and 860 ºC. The corresponding FWHM (Δω) values of the (400) peak are 3.5º, 3.22º, and 2.78º, which illustrate that the highly crystalline β-Ga_2O_3 could be achieved if a higher temperature is used in the RF sputter deposition process.

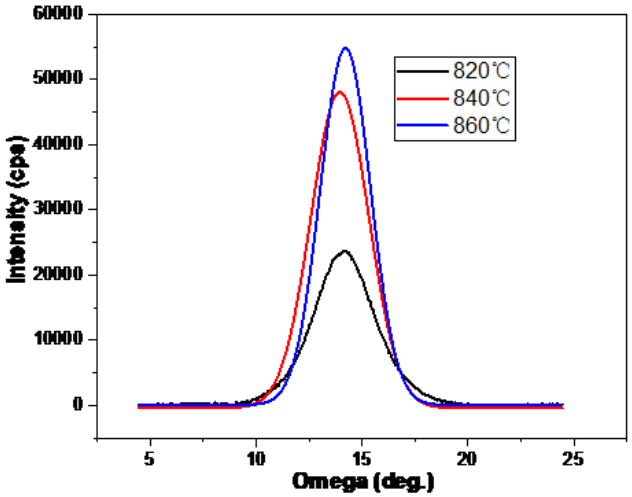

Figure 6.3 (400) peak XRD rocking curve of β-Ga_2O_3 film deposited at different temperatures from 820ºC to 860ºC.

6.1.3 Epitaxial growth of β-Ga_2O_3 on IBAD MgO as a function of O_2 flow

The relationship between O_2 flow and the β-Ga_2O_3 texture was investigated next. All deposition conditions remained consistent with the previous run, and the deposition temperature was set 800 ºC. Three different O_2 flow levels were employed.

In figure 6.4, when 0 sccm O_2 was applied, no (400) peak was observed, and the possible (-601) peak was identified instead. This peak was observed when the β-Ga_2O_3/MgO sample annealed in the N_2 atmosphere [177], which indicates possible oxygen atom loss from the as-deposited β-Ga_2O_3 film during the annealing process. Therefore, the absence of O_2 flow during the RF sputter deposition could cause the

growth of β-Ga_2O_3 in an another orientation different from (400). There was no significant difference observed in the XRD scan when 1 sccm and 2 sccm O_2 used applied, although (400) peaks of both samples showed low intensity.

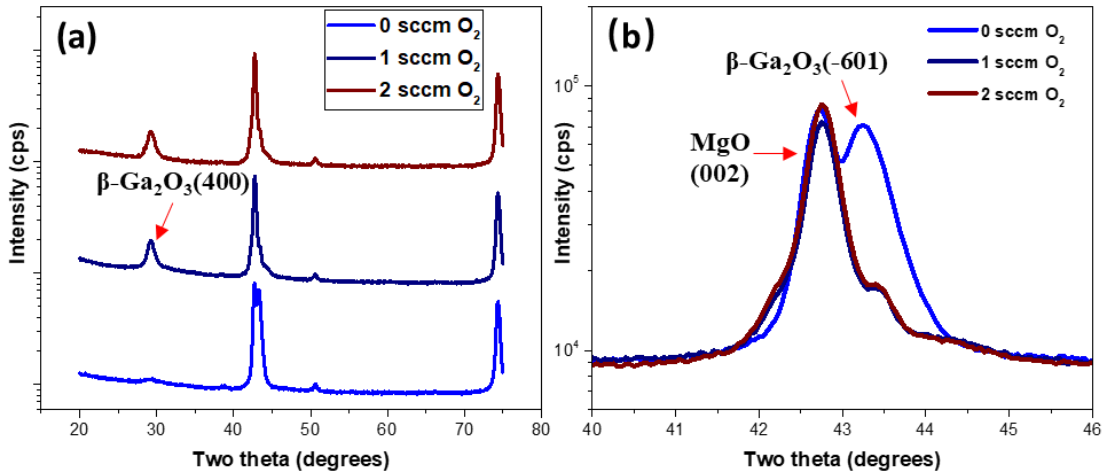

Figure 6.4 (a) XRD θ-2θ scan of β-Ga_2O_3 deposited on IBAD MgO with different O_2 flow; (b) θ-2θ scans magnified in the range of 40° to 46°.

6.1.4 Epitaxial growth of β-Ga_2O_3 on IBAD MgO as a function of the deposition pressure

In this section, the texture of β-Ga_2O_3 was investigated as a function of deposition pressure. All samples were processed with the same parameters (800 ºC, 1 sccm O_2), except the deposition pressure. The pressure during the β-Ga_2O_3 deposition was controlled by a throttle valve. The pressure was at 4.2 mTorr when the throttle valve is fully open.

As shown in figure 6.5 (a) and (b), the β-Ga_2O_3 (400) peak intensity increases when the pressure rose from 4.2 mTorr to 31 mTorr and drops when the pressure is increased from 31 mTorr to 61 mTorr. The smallest FWHM (Δω) of β-Ga_2O_3 (400) was also observed for the sample processed at 31mTorr, which indicates the high deposition rate with good textured film can be achieved simultaneously at this pressure level.

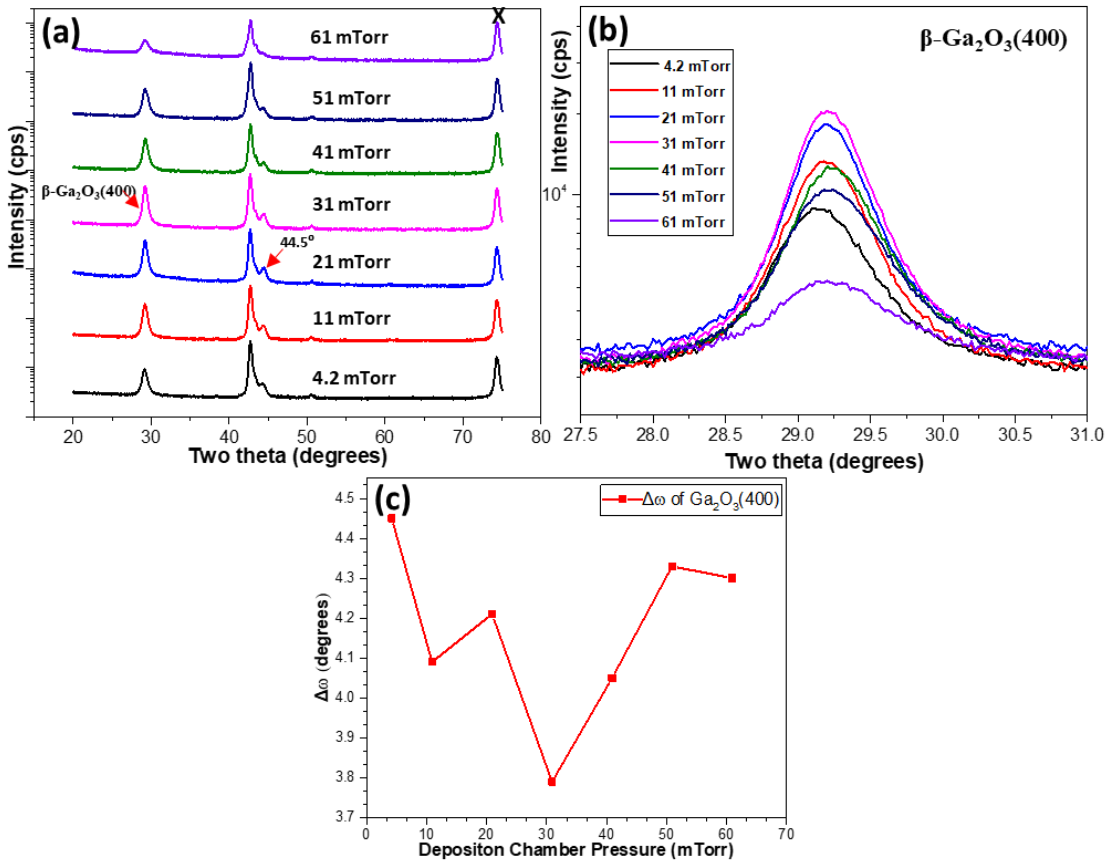

Figure 6.5 (a) XRD θ-2θ scan of β-Ga_2O_3 deposited on IBAD MgO at different chamber pressures; (b) θ-2θ scan curves magnified in the range of 27º to 31º. (c) FWHM (Δω) of β-Ga_2O_3 (400) peak as a function of chamber pressure.

There is another peak located at 44.5º 2-theta angle with the highest intensity at a deposition pressure of 30 mTorr. Wakabayashi suggests that there could a metastable γ-Ga_2O_3 interfacial layer that exists between the MgO and (100)-oriented β-Ga_2O_3. Since γ-Ga_2O_3 (400) shares the same 44.5º 2theta angle with β-Ga_2O_3 (600), the 44.5º peak may be the mixed peak between β-Ga_2O_3 (600) and metastable γ-Ga_2O_3 (400) [167]. In this case, the peak located at the 44.5º 2-theta angle could be dominated by γ-Ga_2O_3 (400) when a relatively low deposition rate was used. On the contrary, this peak will be dominated by β-Ga_2O_3 (600) if the film becomes thicker with a higher deposition rate, at 30 mTorr.

6.1.5 Epitaxial growth of β-Ga_2O_3 on IBAD MgO as a function of the tape feed speed

The relationship between the tape feed speed and the as-deposited β-Ga_2O_3 film texture was also investigated. Two speeds, 1.4 cm/min and 0.5 cm/min, were used for samples passing through the 12-cm length deposition zone (Mark as GOX1 and GOX2, respectively). All the samples were processed with 1 sccm O_2 flow and 800 W RF power. The deposition processed at 860ºC after better textured β-Ga_2O_3 film demonstrated at this temperature in previous run. The system pressure of 31 mTorr was maintained, as previously optimized.

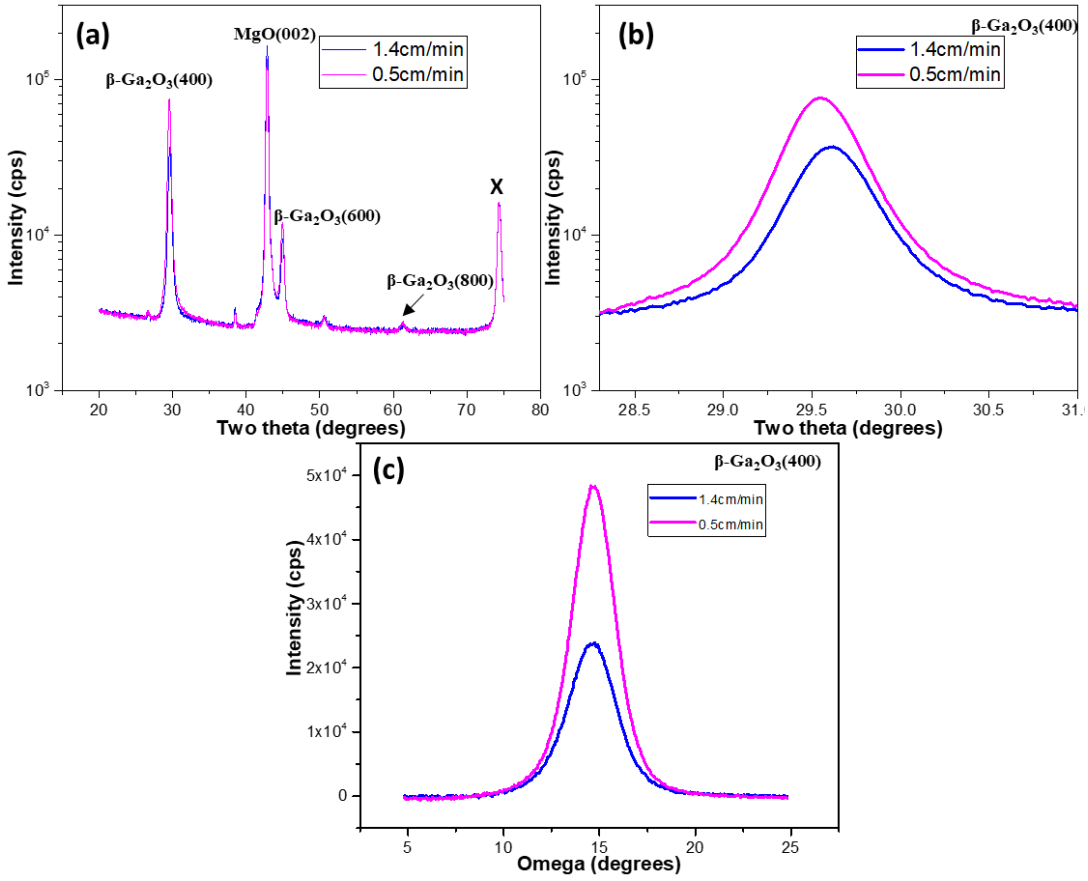

Figure 6.6 (a) XRD θ-2θ scans of β-Ga_2O_3 deposited on IBAD MgO with different tape feed speed; (b) θ-2θ scans magnified in the range of 27º to 31º. (c) (400) peak XRD rocking curves of β-Ga_2O_3 film.

Figure 6.6 (a) and (b) show the XRD θ-2θ scans of both samples. The β-Ga_2O_3 (400), (600), and (800) peaks have been identified in the XRD 2theta scan. Also, the peak intensity of β-Ga_2O_3 (400) reaches the same intensity as the MgO (002) peak, which indicates that a highly textured (100)-oriented β-Ga_2O_3 film achieved on the IBAD-MgO-capped Hastelloy tape. Figure 6.6 (c) provides the omega scan of (400) peaks for both GOX1 and GOX2. The FWHM (Δω) of GOX1 (400) is 3.1º and decreased to 2.78º for GOX2, which means that the thicker film has a better texture.

A slower tape speed (0.25cm/min) was also tested for β-Ga_2O_3 growth. Figure 6.7 provides the General Area Detector Diffraction System (GADDS) diffraction pattern of β-Ga_2O_3 on IBAD MgO when a 0.25cm/min tape speed was used. The bottom right corner shows the sample photo. The tape may have been overheated since the β-Ga_2O_3 (400) peak is spread and twins showing up, and possible MgO (002) peak split. Besides that, the sample tape shows severe curvature along the width direction. In general, the long-time heating brought about by the slow tape speed caused deterioration of the β-Ga_2O_3 texture.

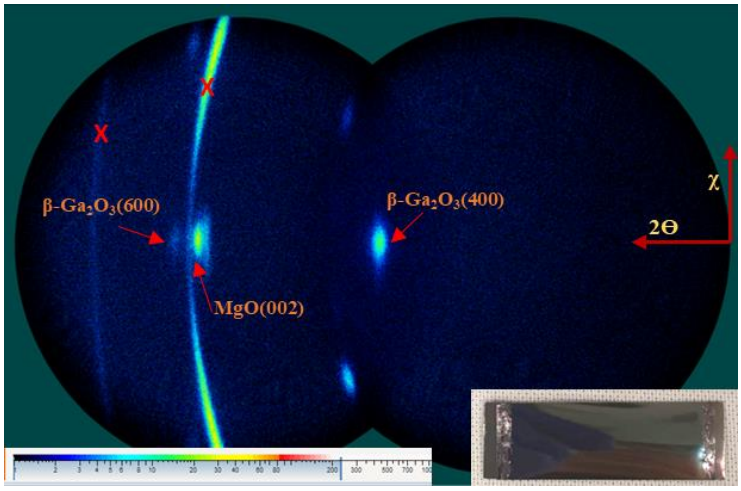

Figure 6.7 General Area Detector Diffraction System (GADDS) diffraction patterns for the β-Ga_2O_3 film deposited at 0.25cm/min tape feed speed; the sample photo is shown at the bottom right corner.

6.1.6 Epitaxial growth of β-Ga_2O_3 on IBAD MgO buffer of different thickness

The relationship between the IBAD MgO buffer layer and β-Ga_2O_3 was also investigated. IBAD MgO with different thickness homo epitaxial MgO layers was used as the substrate. The MgO thickness of the substrate is around 50-60nm (IBAD MgO1) and 150-200nm (IBAD MgO2), with corresponding MgO(002) FWHM(Δω) of 2.5º and 2.0º, respectively. All deposition processes followed the previously optimized conditions.

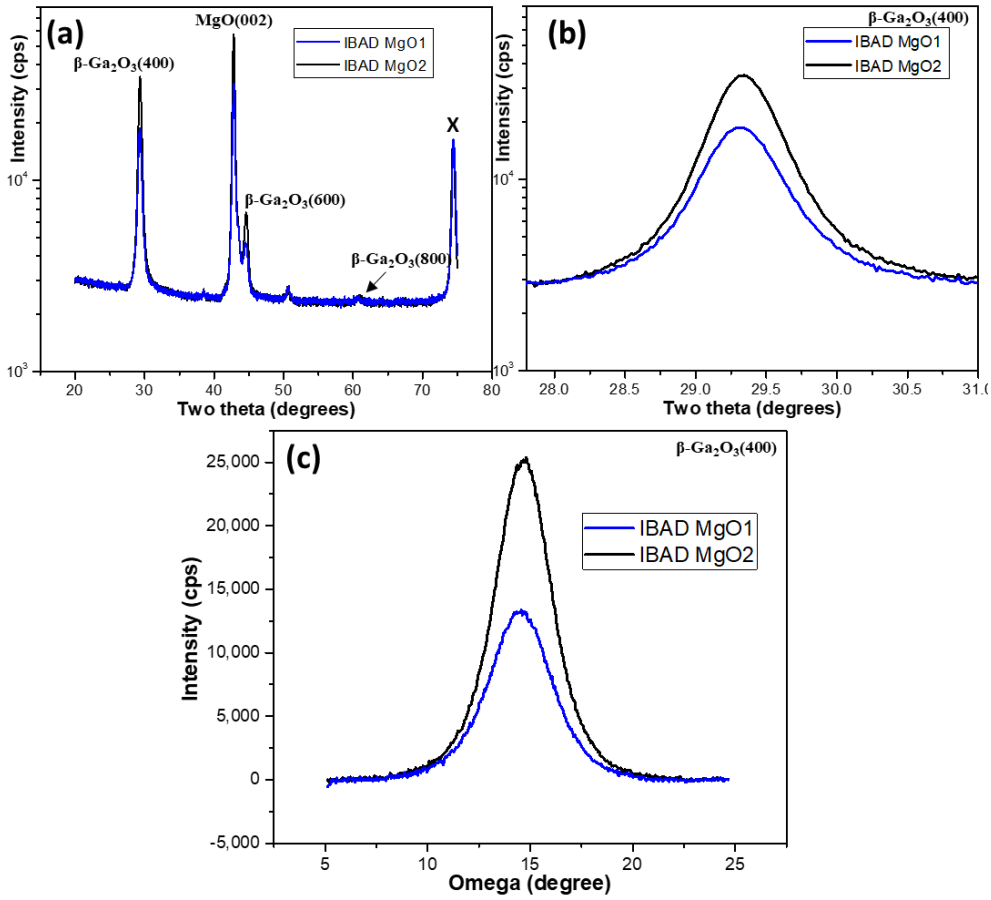

Figure 6.8 (a) XRD θ-2θ scans of β-Ga_2O_3 deposited on IBAD MgO with different thickness of homo-epitaxial MgO buffer layer; (b) θ-2θ scans magnified in the range of 27º to 31º. (c) (400) peak XRD rocking curves of β-Ga_2O_3 film.

As shown in Figure 6.8 (a) and (b), the intensity of the β-Ga_2O_3 (400) and (600) peaks increased with the corresponding MgO (002) peak. The omega scan of β-Ga_2O_3

(400) in Figure 6.8 (c) shows the Δω of (400) peak improved from 3.31º to 2.87º when the MgO substrate is thicker.

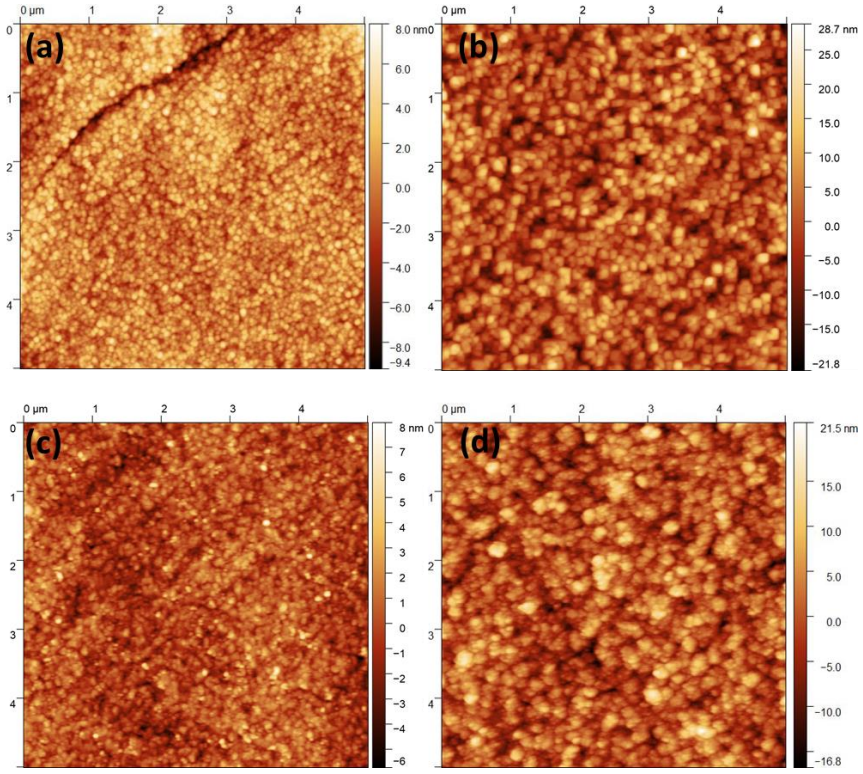

Figure 6.9 AFM surface profile of (a)IBAD MgO1; (b)IBAD MgO2; (c)β-Ga_2O_3/IBAD MgO1; (d) β-Ga_2O_3/IBAD MgO2.

Figure 6.9 shows the surface profiles of the IBAD MgO substrate and corresponding β-Ga_2O_3 measured by atomic force microscope (AFM). All AFM images illustrate the surface morphology at a 5 μm × 5 μm scale. Figures 6.9 (a) and (b) demonstrate the AFM surface profiles of IBAD MgO1 and IBAD MgO2 with corresponding R_q (RMS) roughness of 1.84 nm and 6.27 nm, respectively. It is evident that the biaxially-textured MgO cubic grains are larger when the MgO film becomes thick. Figures 6.9 (c) and (d) show the AFM profiles of IBAD MgO1 and IBAD MgO2 surfaces after the β-Ga_2O_3 deposition. β-Ga_2O_3 on IBAD MgO1 shows many small fine grains with RMS of 1.36 nm, which is close to the substrate. The β-Ga_2O_3 on IBAD MgO2 shows large grains, with an RMS roughness of 4.87 nm. It is not yet clear how this high roughness and large

grains could affect the next step of device fabrication or homoepitaxial growth by the MOCVD method.

6.1.7 Epitaxial growth of β-Ga_2O_3 on IBAD MgO buffer with Si-doped target

For device application, appropriate control of conductivity is an essential requirement for UWBG semiconductors like β-Ga_2O_3. N-type doping of β-Ga_2O_3 could be achieved by group IV elements such as Si, Ge, and Sn. These IV group dopants can substitute the Ga site in β-Ga_2O_3 and become shallow donors [178]. The deposition of β-Ga_2O_3 was repeated with a Ga_2O_3 target doped with 1wt% SiO_2 using the previously optimized conditions. Both IBAD MgO1 and IBAD MgO2 were used as the substrates in this run.

Figure 6.10 shows the AFM surface profiles and GADDS diffraction patterns of β-Ga_2O_3 on both kinds of IBAD MgO substrates. The Δω of β-Ga_2O_3 (400) reaches 1.685º and 1.541º on IBAD MgO1 and IBAD MgO2, respectively. Both β-Ga_2O_3 (400) and (600) peaks show much higher intensities. Besides that, only weak twins are observed near the (600) position on β-Ga_2O_3/IBAD MgO1, which may be caused by the Si doping. The AFM surface profiles also demonstrates the excellent texture of the β-Ga_2O_3 film. The grain size of β-Ga_2O_3 on IBAD MgO2 is still larger than that on IBAD MgO1, which is the same as before in films made with undoped target. However, all the grains are aligned in a diagonal orientation, 45º to the those of the MgO film, like knitted fabric. This is a good demonstration of the in-plane epitaxial relationship (β-Ga_2O_3[001] || MgO<011>) between the MgO and β-Ga_2O_3. This kind of AFM surface morphology is quite different compared to the previous sample, which was processed with an undoped Ga_2O_3 target. Further experiments are necessary to investigate if there was any

contribution from the Si atom to this excellent texture of β-Ga_2O_3 film with highly oriented grains.

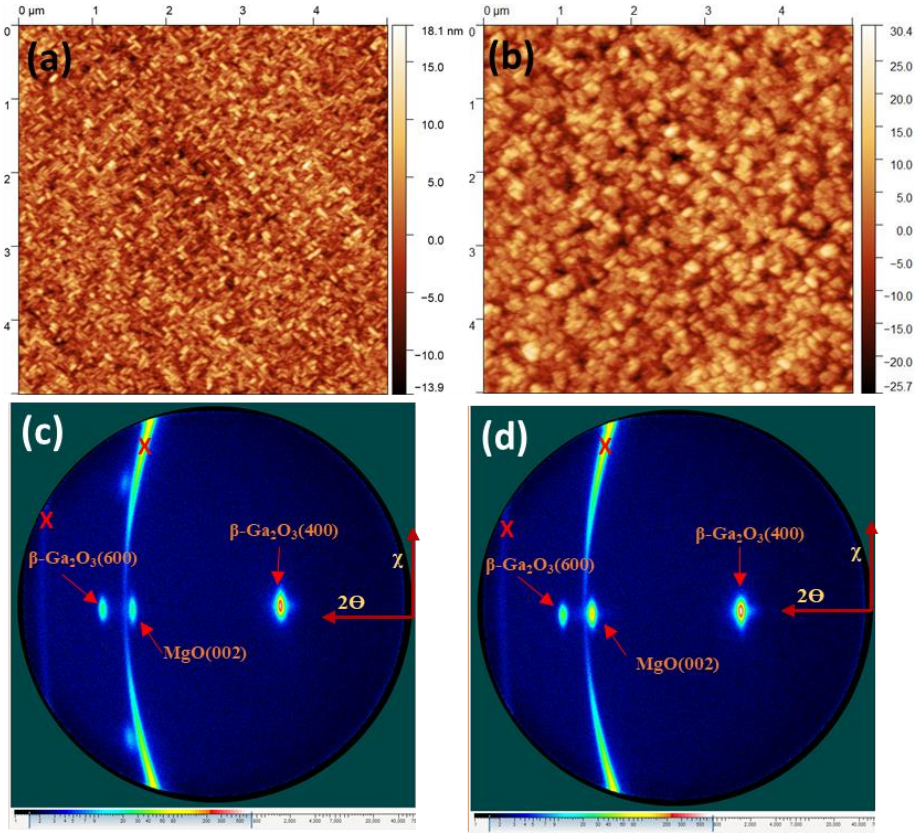

Figure 6.10 AFM surface profiles of (a) β-Ga_2O_3/IBAD MgO1;(b)β-Ga_2O_3/IBAD MgO2 when β-Ga_2O_3 processed with Si-doped target. (d) (e) Corresponding GADDS diffraction patterns, respectively.

6.2 Epitaxial relationship between the MgO and β-Ga_2O_3

As previously demonstrated, the out-of-plane epitaxial relationship between the IBAD MgO and β-Ga_2O_3 is β-Ga_2O_3(100) || MgO(100). The four-fold peaks of β-Ga_2O_3 (002) were observed at the same angle as MgO (222) in the XRD ϕ scan, which means that the β-Ga_2O_3 grains are in-plane titled 45º from the cubic MgO surface. An XRD in-plane ϕ scan was also performed on the β-Ga_2O_3/IBAD MgO2. Peaks with a four-fold symmetry was observed, and the average FWHM (Δϕ) of the {002} peaks was 4.8º,

which indicates the excellent in-plane texture of β-Ga_2O_3 grown on IBAD MgO (Figure 6.11).

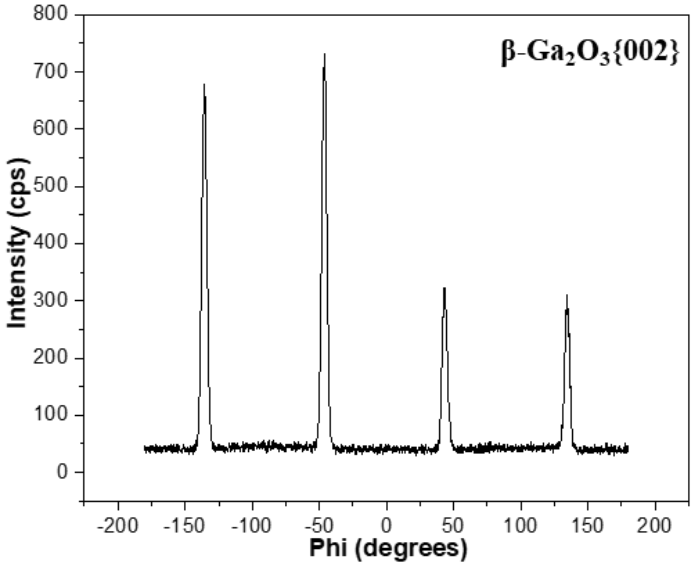

Figure 6.11 XRD {002} Phi scan of β-Ga_2O_3/IBAD MgO2 when β-Ga_2O_3 processed with a Si-doped target.

The in-plane epitaxial relationship could also be explained by the small lattice mismatch between the monoclinic β-Ga_2O_3 and the cubic MgO. The lattice constant (Mark as a^1) of the cubic MgO is 4.22 Å. For the monoclinic β-Ga_2O_3, the lattice parameters of a, b, and c are different: a=12.21Å, b=3.03Å, and c=5.79Å. In the MgO <011> direction, $\sqrt{2}a^1$=5.97Å, which is similar to the lattice constant c in β-Ga_2O_3 (2.9% lattice mismatch). On the other side, the lattice mismatch between 2b (6.08Å) and $\sqrt{2}a^1$ is only -1.8%.

In addition, the surface atomic arrangement of β-Ga_2O_3 helps this epitaxial growth. Figure 6.12 (a) and (b) provides two side views of two β-Ga_2O_3 unit cells along the b and a direction, respectively. Only part of the O atoms are shown here. The distance between the O atoms matches with the lattice parameters of 2b and c, which means β-

Ga_2O_3 could achieve a suitable epitaxial atom arrangement with a twisted, diagonal orientation of MgO.

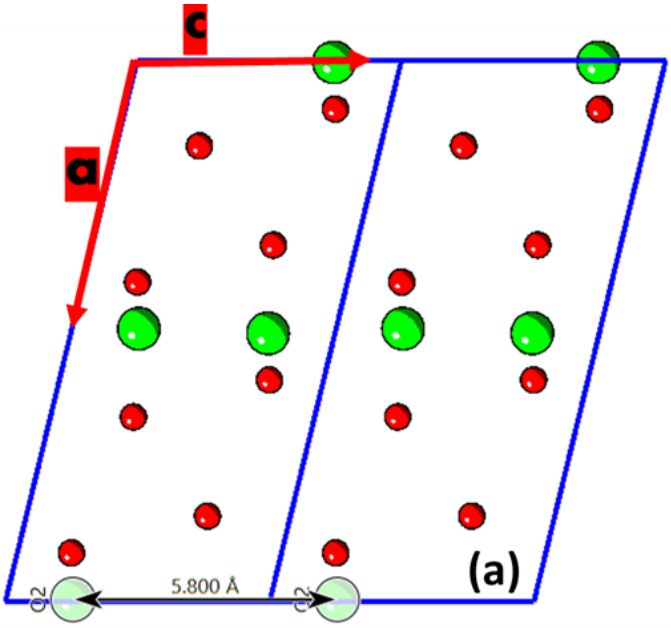

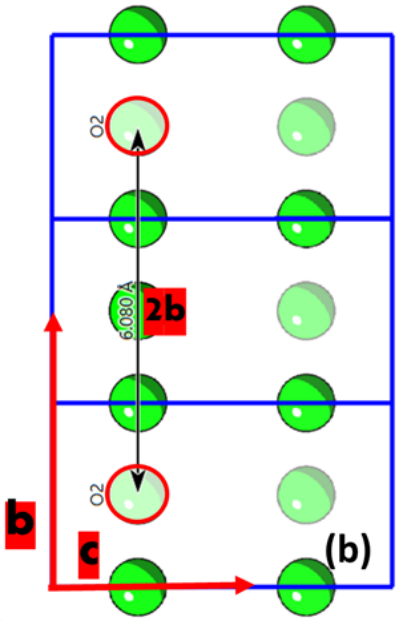

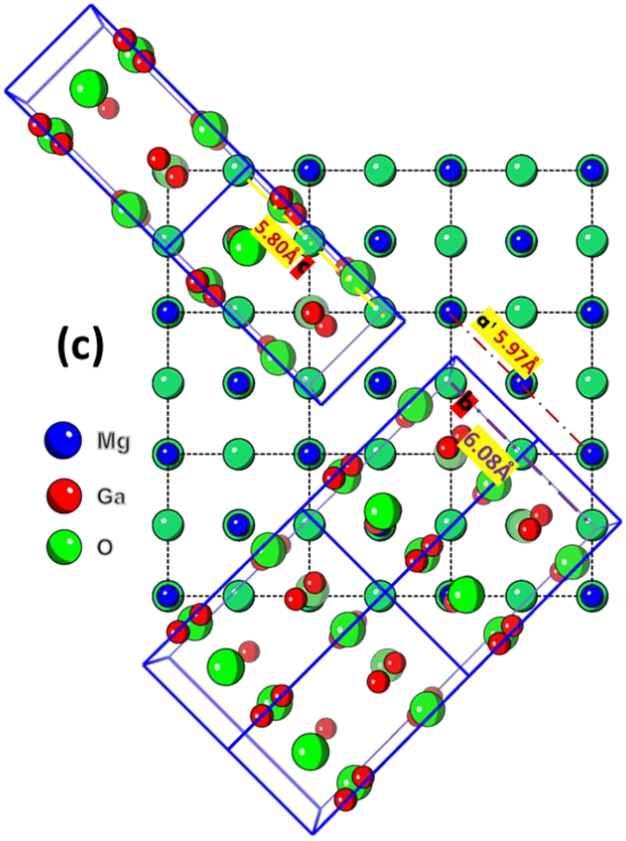

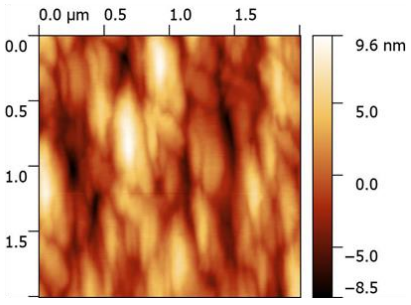

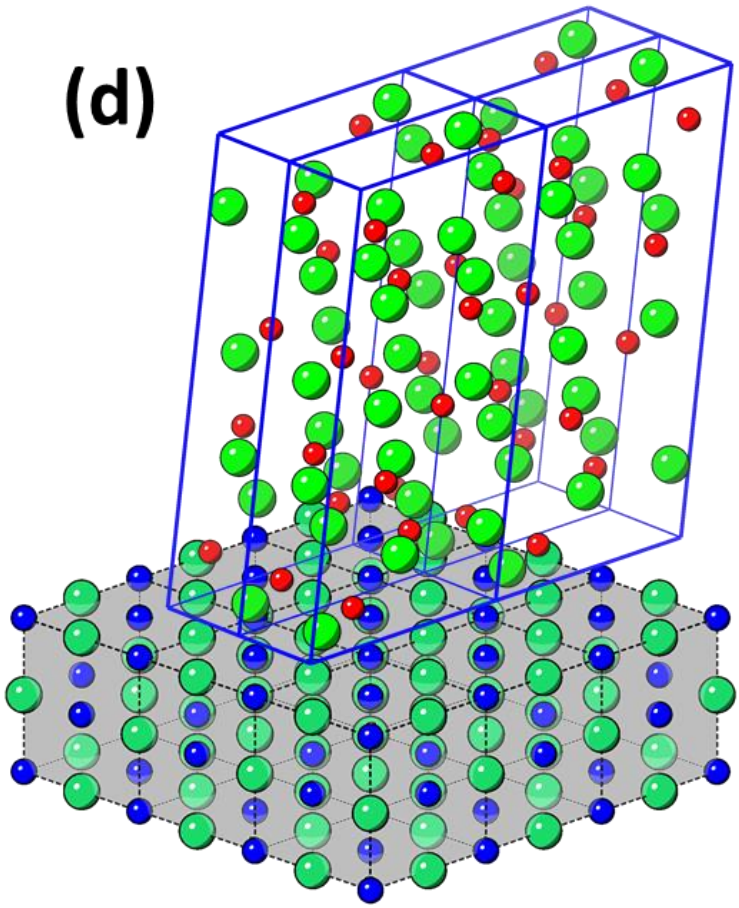

Figure 6.12 Crystal structure of β-Ga_2O_3, showing only Ga and O atoms at position 3 (a) projection of two unit cells along the b direction, the distance between two surface O atoms is 5.8Å; (b) projection of three unit cells along the a direction, the distances between O atoms in two end unit cells is 6.08Å, equal to 2b. (c) Schematic top view of β-Ga_2O_3 unit cells stack on top of MgO with different domains with corresponding AFM profile; (d) 3D view of β-Ga_2O_3 unit cells stack on MgO;

However, due to the unique monoclinic structure of β-Ga_2O_3 (β=103.8º), the lattice match between β-Ga_2O_3 and MgO could create four symmetry domains along [011], [01-1], [0-11], and [0-1-1], respectively [173]. Figure 6.12 (c) shows the schematic view of the β-Ga_2O_3 domains on the MgO substrate. This alignment relationship is also confirmed by the corresponding AFM surface image, as shown in Figure 6.12 (c) also. Figure 6.12 (d) provides a 3D view of β-Ga_2O_3 unit cells stack on top of MgO crystal.

Figure 6.13 shows the transmission electron microscopy (TEM) cross-section image of the (100)-oriented β-Ga_2O_3 on the IBAD MgO buffer. Many defects in the MgO layer

propagates to the top β-Ga_2O_3, as shown in figure 6.13 (b). There is also a 10-nm thickness interfacial layer between the β-Ga_2O_3 and MgO. This layer has been identified before by other researchers and is believed to be γ- Ga_2O_3. The γ-Ga_2O_3 phase may be easier to form at a temperature higher than 550 ºC, and it has a cubic structure, which is similar to MgO [176]. Besides that, it is evident to identify the faces parallel to β-Ga_2O_3 (100) in the TEM image of the β-Ga_2O_3 phase. Different twin domains also exist in the top β-Ga_2O_3 film, as demonstrated in figure 6.13 (d).

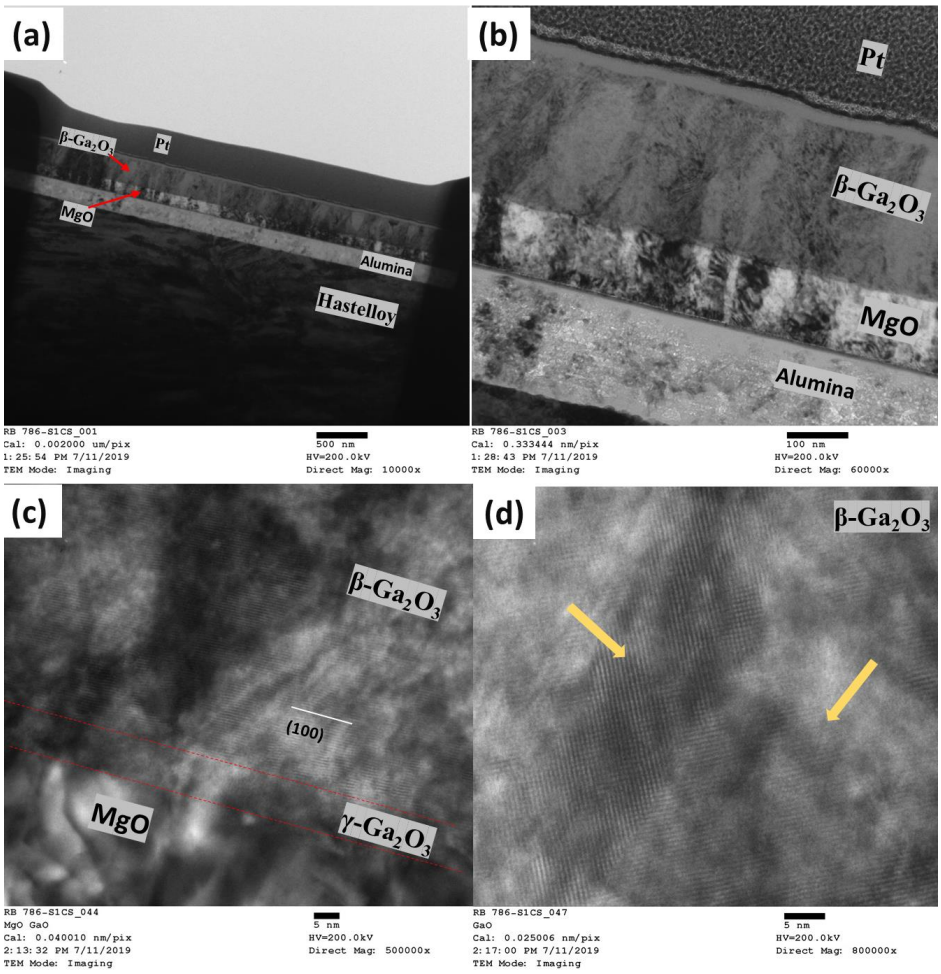

Figure 6.13 Cross-sectional transmission electron microscopy (TEM) image of β-Ga_2O_3 grown on IBAD-MgO-capped Hastelloy (a) a low-magnification view of the multilayer architecture; (b)high-magnification view of multilayer architecture;(c)(d) high-magnification view of β-Ga_2O_3 layer.

6.3 Summary

In this chapter, the heteroepitaxial β-Ga_2O_3 thin film was achieved on the biaxially-textured IBAD-MgO-capped flexible Hastelloy tape. The deposition temperature, pressure, O_2 flow, tape feed speed, and different thickness of the IBAD MgO were optimized for better β-Ga_2O_3 texture. The 1wt% SiO_2-doped β-Ga_2O_3 was used as the sputter source for doping purposes. The (100) oriented β-Ga_2O_3 deposited on the IBAD MgO with a Si-doped target can reach (400) Δω of 1.541º and {002} Δϕ of 4.81º. The as-deposited β-Ga_2O_3 film is highly textured with a knitted-fabric shape aligned β-Ga_2O_3 grains, which are 45º in-plane twisted from the MgO substrate. The crystal orientation relationship proved to be [100] β-Ga_2O_3 || <011> MgO for the in-plane and (100) β-Ga_2O_3 || (100) MgO for out-of-plane orientations. The TEM images reveal that a γ-Ga_2O_3 thin film exists at the interface between β-Ga_2O_3 and MgO. This highly-textured Si-doped β-Ga_2O_3 could provide a new avenue for fabrication of UWBG devices on a flexible and thermally-conductive substrate.

CHAPTER 7 SUMMARY AND FUTURE WORKS

7.1 Summary

Biaxially-textured TiN film was demonstrated on electropolished Hastelloy (EPH) substrate without using any foreign seed layer during the IBAD process. The Ar^+ ion-bombardment process before the IBAD removes foreign particles and smoothens the surface, helping to achieve better adatom adhesion. More than two minutes pre-etching is found stabilize the EPH surface morphology. IBAD TiN was grown on the pre-etched EPH surface with a (002) $\Delta\omega$ of 1.8º and (220) $\Delta\phi$ of 5.6º.

Biaxially-textured LMO/MgO/IBAD MgO has been realized on planarized yttria-stabilized zirconia (YSZ) flexible tape. A low surface roughness (<1 nm) was reached by the multilayer spin coating planarization process. As a following step, the IBAD MgO process parameters were optimized to achieve improved texture on the planarized YSZ. LMO with (200) $\Delta\omega$ of 2.87º and (220) $\Delta\phi$ of 6.48º was demonstrated on flexible YSZ tape.

Ag/TiN intermediate layers were employed to improve the texture of the well-established LMO/MgO/IBAD MgO buffer architecture on flexible Hastelloy tape. A TiN/Ag/IBAD MgO structure was developed first for texture improvement. LMO/MgO deposited on the buffer structure showed dramatic texture improvement with a $\Delta\omega$ of 1.7º and $\Delta\phi$ of 2.8º. This architecture has been optimized further to eliminate the twins generated from the IBAD MgO. An extra TiN layer has been added on top of the IBAD MgO before Ag deposition to prevent the Mg diffusion and enhance bonding between the Ag and TiN layers. LMO/MgO deposited on this TATM buffer also showed similar texture improvement compared with the TAM. A simplified TM buffer was also

designed and optimized for LMO/MgO texture improvement, and the LMO showed a 20% percentage texture improvement when 160 nm TiN intermediate layers were used in the LMTM structure.

Single-crystal-like, biaxially-textured β-Ga_2O_3 has been demonstrated for the first time on biaxially-textured IBAD MgO/Hastelloy flexible tape by a roll-to-roll RF sputtering process. The texture of this β-Ga_2O_3 film shows strong (100) out plane orientation growth over the (100) MgO. The epitaxial relationship between β-Ga_2O_3 and MgO substrates was found to be [100] β-Ga_2O_3 || <011> MgO and (100) β-Ga_2O_3 || (100) MgO for in-plane and out-of-plane orientations, respectively. The β-Ga_2O_3 deposited with a Si-doped target showed an excellent texture with (400) $\Delta\omega$ of 1.54º and {002} $\Delta\phi$ of 4.81º. The final film shows a knitted-fabric shape aligned β-Ga_2O_3 grains with 45º rotated in-plane from the MgO lattice.

7.2 Future works

The biaxially textured conductive buffer structure developed on Hastelloy tape has several attractive features since it can help minimize the risk of localized thermal damages in HTS tape and also simplify the GaAs solar cell device structure on flexible Hastelloy tape. As a future work, REBCO tapes need to be fabricated with IBAD TiN conductive cap layers. The EPH surface after ion bombardment needs further characterization by EDS and secondary-ion mass spectrometry (SIMS) to examine if any seed layer formed. Initial work that has been done to fabricate and test vertical GaAs solar cells needs to be continued.

Biaxially-textured buffers developed on flexible YSZ tape has a lot of promise for use of HTS in high signal-to-noise ratio MRI imaging and cryogenic quantum

computing transmission lines. Although good biaxially texture has been achieved on flexible ceramic substrate, there remains room for further optimization. The IBAD MgO texture can be optimized further as a function of different sputter beam energies. The REBCO deposition process needs to be developed to fit with the ceramic tape. Also, an appropriate coating method needs to be established to realize the planarization coating on long YSZ tapes in a continuous process. Mechanical bending test is necessary to evaluate the REBCO/buffer layer bonding strength on the YSZ tape.

Even though excellent texture was achieved using Ag in the buffer architecture for REBCO tapes, since the thermal expansion coefficient of Ag is quite different from the oxide buffers, the buffer architecture hardly survived during the roll-to-roll high-temperature REBCO MOCVD process. A modified REBCO deposition could be pursued to benefit from the improved texture of the buffer architecture with Ag/TiN layers.

Ultra-wide bandgap semiconductors are promising for next-generation high-power devices and ultraviolet photodetectors and the demonstration of epitaxial β-Ga_2O_3 on flexible metallic substrate has much potential. The electrical properties of Si-doped β-Ga_2O_3 film demonstrated in this work still needs further characterization such as the Hall mobility measurement. Since the surface roughness of β-Ga_2O_3 on metal substrate is higher compared with the homoepitaxial growth on a β-Ga_2O_3 wafer, multi-step deposition may be necessary to achieve low surface roughness. This sputter-deposited β-Ga_2O_3 can be now used as a template for MOCVD homoepitaxial growth.

References

[1] C.-F. Chien, J. Wang, T.-C. Chang, and W.-C. Wu, "Economic analysis of 450mm wafer migration." pp. 1-4.

[2] R. C. Leachman, S. Ding, and C.-F. Chien, "Economic efficiency analysis of wafer fabrication," *IEEE Transactions on Automation Science and Engineering,* vol. 4, no. 4, pp. 501-512, 2007.

[3] "Evolution of the Silicon Wafer," https://f450c.org/infographic/.

[4] D. Dobrev, "Ion-beam-induced texture formation in vacuum-condensed thin metal films," *Thin Solid Films,* vol. 92, no. 1-2, pp. 41-53, 1982.

[5] S. Rossnagel, and J. Cuomo, "Ion-Beam-Assisted Deposition and Synthesis," *MRS Bulletin,* vol. 12, no. 2, pp. 40-51, 1987.

[6] L. S. Yu, J. M. Harper, J. J. Cuomo, and D. A. Smith, "Alignment of thin films by glancing angle ion bombardment during deposition," *Applied physics letters,* vol. 47, no. 9, pp. 932-933, 1985.

[7] L. S. Yu, J. M. Harper, J. J. Cuomo, and D. A. Smith, "Control of thin film orientation by glancing angle ion bombardment during growth," *Journal of Vacuum Science & Technology A: Vacuum, Surfaces, and Films,* vol. 4, no. 3, pp. 443-447, 1986.

[8] Y. Iijima, N. Tanabe, Y. Ikeno, and O. Kohno, "Biaxially aligned $YBa_2Cu_3O_{7-x}$ thin film tapes," *Physica C: Superconductivity,* vol. 185, pp. 1959-1960, 1991.

[9] Y. Iijima, N. Tanabe, O. Kohno, and Y. Ikeno, "In-plane aligned $YBa_2Cu_3O_{7-x}$ thin films deposited on polycrystalline metallic substrates," *Applied Physics Letters,* vol. 60, no. 6, pp. 769-771, 1992.

[10] J. Dzick, J. Hoffmann, S. Sievers, L. Kautschor, and H. Freyhardt, “Ion-beam-assisted texturing of YSZ layers,” *Physica C: Superconductivity,* vol. 372, pp. 723-728, 2002.

[11] Y. Iijima, K. Kakimoto, and K. Takeda, “Ion beam assisted growth of fluorite type oxide template films for biaxially textured HTSC coated conductors,” *IEEE transactions on applied superconductivity,* vol. 11, no. 1, pp. 3457-3460, 2001.

[12] C. Wang, K. Do, M. Beasley, T. Geballe, and R. Hammond, “Deposition of in-plane textured MgO on amorphous Si_3N_4 substrates by ion-beam-assisted deposition and comparisons with ion-beam-assisted deposited yttria-stabilized-zirconia,” *Applied Physics Letters,* vol. 71, no. 20, pp. 2955-2957, 1997.

[13] V. Matias, J. Hänisch, E. J. Rowley, C. Sheehan, P. G. Clem, N. Kumasaka, and I. Kodaka, “Preparation of substrates for IBAD-MgO coated conductors,” *MRS Online Proceedings Library Archive,* vol. 1001, 2007.

[14] N. Sonnenberg, A. Longo, M. Cima, B. Chang, K. Ressler, P. McIntyre, and Y. Liu, “Preparation of biaxially aligned cubic zirconia films on pyrex glass substrates using ion-beam assisted deposition,” *Journal of applied physics,* vol. 74, no. 2, pp. 1027-1034, 1993.

[15] A. Goyal, D. Norton, J. Budai, M. Paranthaman, E. Specht, D. Kroeger, D. Christen, Q. He, B. Saffian, and F. List, “High critical current density superconducting tapes by epitaxial deposition of $YBa_2Cu_3O_x$ thick films on biaxially textured metals,” *Applied Physics Letters,* vol. 69, no. 12, pp. 1795-1797, 1996.

[16] Y. Iijima, M. Hosaka, N. Tanabe, N. Sadakata, T. Saitoh, O. Kohno, and K. Takeda, “Growth structure of yttria-stabilized-zirconia films during off-normal ion-beam-assisted deposition,” *Journal of materials research,* vol. 13, no. 11, pp. 3106-3113, 1998.

[17] V. Matias, and R. H. Hammond, “Ion beam induced crystalline texturing during thin film deposition,” *Surface and Coatings Technology,* vol. 264, pp. 1-8, 2015.

[18] Y. Iijima, K. Onabe, N. Futaki, N. Tanabe, N. Sadakata, O. Kohno, and Y. Ikeno, “Structural and transport properties of biaxially aligned $YBa_2Cu_3O_{7-x}$ films on polycrystalline Ni-based alloy with ion-beam-modified buffer layers," *Journal of Applied Physics,* vol. 74, no. 3, pp. 1905-1911, 1993.

[19] X. Wu, S. Foltyn, P. Arendt, J. Townsend, C. Adams, I. Campbell, P. Tiwari, Y. Coulter, and D. E. Peterson, “High current $YBa_2Cu_3O_{7-\delta}$ thick films on flexible nickel substrates with textured buffer layers,” *Applied Physics Letters,* vol. 65, no. 15, pp. 1961-1963, 1994.

[20] S. Gnanarajan, and N. Savvides, “Evolution of texture of CeO_2 thin film buffer layers prepared by ion-assisted deposition,” *Thin Solid Films,* vol. 350, no. 1-2, pp. 124-129, 1999.

[21] X. Xiong, and D. Winkler, “Rapid deposition of biaxially-textured CeO_2 buffer layers on polycrystalline nickel alloy for superconducting tapes by ion assisted pulsed laser deposition,” *Physica C: Superconductivity,* vol. 336, no. 1-2, pp. 70-74, 2000.

[22] J. Wang, R. Fromknecht, and G. Linker, “Preparation of biaxially textured CeO_2 buffer layers by ion beam-assisted deposition,” *Surface and Coatings Technology*, vol. 158, pp. 548-551, 2002.

[23] H.-F. Li, T. Parker, F. Tang, G.-C. Wang, T.-M. Lu, and S. Lee, “Biaxially oriented CaF_2 films on amorphous substrates,” *Journal of crystal growth*, vol. 310, no. 15, pp. 3610-3614, 2008.

[24] J. R. Groves, J. B. Li, B. M. Clemens, V. LaSalvia, F. Hasoon, H. M. Branz, and C. W. Teplin, “Biaxially-textured photovoltaic film crystal silicon on ion beam assisted deposition CaF_2 seed layers on glass,” *Energy & Environmental Science*, vol. 5, no. 5, pp. 6905-6908, 2012.

[25] R. Hühne, S. Fähler, and B. Holzapfel, “Thin biaxially textured TiN films on amorphous substrates prepared by ion-beam assisted pulsed laser deposition,” *Applied physics letters*, vol. 85, no. 14, pp. 2744-2746, 2004.

[26] K. Yokota, T. Kasuya, K. Nakamura, M. Ohnishi, and F. Miyashita, “Ion beam current dependence of compositions and resistivities on titanium nitride films deposited onto silicon by an ion beam assisted deposition method,” *Nuclear Instruments and Methods in Physics Research Section B: Beam Interactions with Materials and Atoms*, vol. 242, no. 1-2, pp. 390-392, 2006.

[27] J. R. Groves, P. N. Arendt, S. R. Foltyn, R. F. DePaula, E. J. Peterson, T. G. Holesinger, J. Y. Coulter, R. W. Springer, C. P. Wang, and R. H. Hammond, “Ion-beam assisted deposition of bi-axially aligned MgO template films for YBCO coated conductors,” *IEEE transactions on applied superconductivity*, vol. 9, no. 2, pp. 1964-1966, 1999.

[28] R. T. Brewer, and H. A. Atwater, “Rapid biaxial texture development during nucleation of MgO thin films during ion beam-assisted deposition,” *Applied physics letters,* vol. 80, no. 18, pp. 3388-3390, 2002.

[29] P. N. Arendt, and S. R. Foltyn, “Biaxially textured IBAD-MgO templates for YBCO-coated conductors,” *MRS bulletin,* vol. 29, no. 8, pp. 543-550, 2004.

[30] Y. Li, “Epitaxial Growth of Single-Crystalline-Like Ge Templates with Conductive Buffers on Low-Cost, Flexible Substrates for Thin Film III-V Solar Cells, and Methods for Texture Improvement and Defect Reduction,” 2018.

[31] A. Goyal, D. Norton, D. Christen, E. Specht, M. Paranthaman, D. Kroeger, J. Budai, Q. He, F. List, and R. Feenstra, “Epitaxial superconductors on rolling-assisted biaxially-textured substrates (RABiTS): A route towards high critical current density wire,” *Applied superconductivity,* vol. 4, no. 10-11, pp. 403-427, 1996.

[32] V. S. Sarma, J. Eickemeyer, C. Mickel, L. Schultz, and B. Holzapfel, “On the cold rolling textures in some fcc Ni–W alloys,” *Materials Science and Engineering: A,* vol. 380, no. 1-2, pp. 30-33, 2004.

[33] D. M. Ginsberg, *Physical properties of high temperature superconductors III*: World Scientific, 1992.

[34] X. Xiong, S. Kim, K. Zdun, S. Sambandam, A. Rar, K. P. Lenseth, and V. Selvamanickam, “Progress in high throughput processing of long-length, high quality, and low cost IBAD MgO buffer tapes at SuperPower,” *IEEE transactions on applied superconductivity,* vol. 19, no. 3, pp. 3319-3322, 2009.

[35] T. Forgan. "Resistance is futile," https://physicsworld.com/a/resistance-is-futile/.

[36] X. Xiong, K. P. Lenseth, J. L. Reeves, A. Rar, Y. Qiao, R. M. Schmidt, Y. Chen, Y. Li, Y.-Y. Xie, and V. Selvamanickam, "High throughput processing of long-length IBAD MgO and epi-buffer templates at SuperPower," *IEEE transactions on applied superconductivity,* vol. 17, no. 2, pp. 3375-3378, 2007.

[37] M. P. Paranthaman, and T. Izumi, "High-performance YBCO-coated superconductor wires," *MRS bulletin,* vol. 29, no. 8, pp. 533-541, 2004.

[38] M. Paranthaman, T. Aytug, D. Christen, P. Arendt, S. Foltyn, J. Groves, L. Stan, R. DePaula, H. Wang, and T. Holesinger, "Growth of thick $YBa_2Cu_3O_{7-\delta}$ films carrying a critical current of over 230 A/cm on single LaMnO 3-buffered ion-beam assisted deposition MgO substrates," *Journal of materials research,* vol. 18, no. 9, pp. 2055-2059, 2003.

[39] C. Yoshida, H. Tamura, A. Yoshida, Y. Kataoka, N. Fujimaki, and N. Yokoyama, "Electric field effect in $LaTiO_3/SrTiO_3$ heterostructure," *Japanese journal of applied physics,* vol. 35, no. 11R, pp. 5691, 1996.

[40] K. Kim, M. Paranthaman, D. P. Norton, T. Aytug, C. Cantoni, A. A. Gapud, A. Goyal, and D. K. Christen, "A perspective on conducting oxide buffers for Cu-based YBCO-coated conductors," *Superconductor Science and Technology,* vol. 19, no. 4, pp. R23, 2006.

[41] T. Aytug, M. Paranthaman, H. Zhai, H. Christen, S. Sathyamurthy, D. Christen, and R. Ericson, "Single buffer layers of $LaMnO_3$ or $La_{0.7}Sr_{0.3}MnO_3$ for the

development of $YBa_2Cu_3O_{7-\delta}$-coated conductors: A comparative study," *Journal of materials research,* vol. 17, no. 9, pp. 2193-2196, 2002.

[42] T. Aytug, M. Paranthaman, B. Kang, S. Sathyamurthy, A. Goyal, and D. Christen, "$La_{0.7}Sr_{0.3}MnO_3$: A single, conductive-oxide buffer layer for the development of $YBa_2Cu_3O_{7-\delta}$ coated conductors," *Applied Physics Letters,* vol. 79, no. 14, pp. 2205-2207, 2001.

[43] T. Aytug, J. Wu, C. Cantoni, D. Verebelyi, E. Specht, M. Paranthaman, D. Norton, D. Christen, R. Ericson, and C. Thomas, "Growth and superconducting properties of $YBa_2Cu_3O_{7-\delta}$ films on conductive $SrRuO_3$ and $LaNiO_3$ multilayers for coated conductor applications," *Applied Physics Letters,* vol. 76, no. 6, pp. 760-762, 2000.

[44] Q. Jia, S. Foltyn, P. Arendt, J. Groves, T. Holesinger, M. Hawley, and P. Lu, "Role of $SrRuO_3$ buffer layers on the superconducting properties of $YBa_2Cu_3O_{7-\delta}$ films grown on polycrystalline metal alloy using a biaxially oriented MgO template," *Applied physics letters,* vol. 81, no. 24, pp. 4571-4573, 2002.

[45] R. Hühne, R. Gärtner, S. Oswald, L. Schultz, and B. Holzapfel, "Coated conductor architectures based on IBAD-TiN for high-Jc YBCO films," *Physica C: Superconductivity and its Applications,* vol. 471, no. 21-22, pp. 966-969, 2011.

[46] M. Liu, D. Shi, Q. Li, L. Wang, S. Ye, H. Suo, and S. Dou, "YBCO films doping with SZO particles grown by chemical solution deposition,"

International Journal of Modern Physics B, vol. 23, no. 17, pp. 3532-3537, 2009.

[47] M. Bhuiyan, M. Paranthaman, S. Sathyamurthy, T. Aytug, S. Kang, D. Lee, A. Goyal, E. Payzant, and K. Salama, "MOD approach for the growth of epitaxial CeO_2 buffer layers on biaxially textured Ni–W substrates for YBCO coated conductors," *Superconductor Science and Technology*, vol. 16, no. 11, pp. 1305, 2003.

[48] J. Xiong, Y. Chen, Y. Qiu, B. Tao, W. Qin, X. Cui, J. Tang, and Y. Li, "A novel process for CeO_2 single buffer layer on biaxially textured metal substrates in YBCO coated conductors," *Superconductor Science and Technology,* vol. 19, no. 10, pp. 1068, 2006.

[49] V. Selvamanickam, Y. Chen, X. Xiong, Y. Y. Xie, M. Martchevski, A. Rar, Y. Qiao, R. M. Schmidt, A. Knoll, and K. P. Lenseth, "High performance 2G wires: From R&D to pilot-scale manufacturing," *IEEE transactions on applied superconductivity,* vol. 19, no. 3, pp. 3225-3230, 2009.

[50] V. Matias, J. Hänisch, E. J. Rowley, and K. Güth, "Very fast biaxial texture evolution using high rate ion-beam-assisted deposition of MgO," *Journal of Materials Research,* vol. 24, no. 1, pp. 125-129, 2009.

[51] A. K. Saxena, *High-temperature superconductors*: Springer Science & Business Media, 2012.

[52] C. Cantoni, T. Aytug, D. T. Verebelyi, M. Paranthaman, E. D. Specht, D. P. Norton, and D. K. Christen, "Conductive buffer layers and overlayers for the

thermal stability of coated conductors," *IEEE transactions on applied superconductivity,* vol. 11, no. 1, pp. 3309-3312, 2001.

[53] P. Dutta, M. Rathi, D. Khatiwada, S. Sun, Y. Yao, B. Yu, S. Reed, M. Kacharia, J. Martinez, and A. Litvinchuk, "Flexible GaAs solar cells on roll-to-roll processed epitaxial Ge films on metal foils: a route towards low-cost and high-performance III–V photovoltaics," *Energy & Environmental Science,* vol. 12, no. 2, pp. 756-766, 2019.

[54] S. Pouladi, M. Rathi, D. Khatiwada, M. Asadirad, S. K. Oh, P. Dutta, Y. Yao, Y. Gao, S. Sun, and Y. Li, "High-efficiency flexible III-V photovoltaic solar cells based on single-crystal-like thin films directly grown on metallic tapes," *Progress in Photovoltaics: Research and Applications,* vol. 27, no. 1, pp. 30-36, 2019.

[55] Y. Gao, M. Asadirad, Y. Yao, P. Dutta, E. Galstyan, S. Shervin, K.-H. Lee, S. Pouladi, S. Sun, and Y. Li, "High-performance flexible thin-film transistors based on single-crystal-like silicon epitaxially grown on metal tape by roll-to-roll continuous deposition process," *ACS applied materials & interfaces,* vol. 8, no. 43, pp. 29565-29572, 2016.

[56] V. Selvamanickam, S. Sambandam, A. Sundaram, S. Lee, A. Rar, X. Xiong, A. Alemu, C. Boney, and A. Freundlich, "Germanium films with strong in-plane and out-of-plane texture on flexible, randomly textured metal substrates," *Journal of Crystal Growth,* vol. 311, no. 21, pp. 4553-4557, 2009.

[57] I. Kim, P. N. Barnes, A. Goyal, S. A. Barnett, R. Biggers, G. Kozlowski, C. Varanasi, I. Maartens, R. Nekkanti, and T. Peterson, "Growth of YBCO thin

films on TiN (001) and CeO_2-coated TiN surfaces," *Physica C: Superconductivity*, vol. 377, no. 3, pp. 227-234, 2002.

[58] S. Q. Wang, I. Raaijmakers, B. J. Burrow, S. Suthar, S. Redkar, and K. B. Kim, "Reactively sputtered TiN as a diffusion barrier between Cu and Si," *Journal of applied physics*, vol. 68, no. 10, pp. 5176-5187, 1990.

[59] B. Rauschenbach, and J. Gerlach, "Texture development in titanium nitride films grown by low-energy ion assisted deposition," *Crystal Research and Technology: Journal of Experimental and Industrial Crystallography*, vol. 35, no. 6-7, pp. 675-688, 2000.

[60] J. Xiong, V. Matias, H. Wang, J. Zhai, B. Maiorov, D. Trugman, B. Tao, Y. Li, and Q. Jia, "Much simplified ion-beam assisted deposition-TiN template for high-performance coated conductors," *Journal of Applied Physics*, vol. 108, no. 8, pp. 083903, 2010.

[61] Y. Xia, J. Xiong, F. Zhang, Y. Xue, P. Guo, P. Xu, X. Zhao, and B. Tao, "A Novel All-Conductive Architecture on Biaxially Textured Metal Substrates for YBCO Coated Conductors," *Journal of superconductivity and novel magnetism*, vol. 26, no. 3, pp. 495-498, 2013.

[62] K. Guth, R. Huhne, V. Matias, J. Rowley, T. Thersleff, L. Schultz, and B. Holzapfel, "Preparation of conductive buffer architectures based on IBAD-TiN," *IEEE transactions on applied superconductivity*, vol. 19, no. 3, pp. 3447-3450, 2009.

[63] R. Hühne, K. Güth, R. Gärtner, M. Kidszun, F. Thoss, B. Rellinghaus, L. Schultz, and B. Holzapfel, "Application of textured IBAD-TiN buffer layers in

coated conductor architectures," *Superconductor Science and Technology*, vol. 23, no. 1, pp. 014010, 2009.

[64] Y. Xia, J. Xiong, X. Zhang, K. Hu, F. Zhang, Y. Xue, J. Chu, X. Zhao, B. Tao, and Y. Li, "Preparation and characterization of TiN seed layer in all-conductive multilayer structure for coated conductors," *Journal of Superconductivity and Novel Magnetism,* vol. 27, no. 3, pp. 871-875, 2014.

[65] K. Kim, D. P. Norton, D. K. Christen, C. Cantoni, T. Aytug, and A. Goyal, "Epitaxial (La, Sr) TiO_3 on textured Ni–W as a conductive buffer architecture for high temperature superconducting coated conductor," *Physica C: Superconductivity and its applications,* vol. 468, no. 13, pp. 961-967, 2008.

[66] M. Sungurov, V. Derevyanko, S. Leonov, T. Sukhareva, V. Finkel, and Y. N. Shakhov, "Substrates with a cubic texture based on paramagnetic Ni-W alloy ribbons with thin TiN coating for second-generation high-temperature superconductors," *Technical Physics Letters,* vol. 40, no. 9, pp. 797-800, 2014.

[67] R. Hühne, K. Güth, M. Kidszun, R. Kaltofen, L. Schultz, and B. Holzapfel, "Metallic seed layers for ion-beam assisted pulsed laser deposition of highly textured transition metal nitride films," *Journal of Physics D: Applied Physics,* vol. 41, no. 24, pp. 245404, 2008.

[68] D. Dimos, P. Chaudhari, and J. Mannhart, "Superconducting transport properties of grain boundaries in $YBa_2Cu_3O_{7-x}$ bicrystals," *Physical Review B,* vol. 41, no. 7, pp. 4038, 1990.

[69] D. Larbalestier, A. Gurevich, D. M. Feldmann, and A. Polyanskii, "High-Tc superconducting materials for electric power applications," *Materials For*

Sustainable Energy: A Collection of Peer-Reviewed Research and Review Articles from Nature Publishing Group, pp. 311-320: World Scientific, 2011.

[70] D. Dimos, P. Chaudhari, J. Mannhart, and F. LeGoues, "Orientation Dependence of Grain-Boundary Critical Currents in $YBa_2Cu_3O_{7-\delta}$ Bicrystals," *Physical Review Letters,* vol. 61, no. 2, pp. 219, 1988.

[71] Y. Xue, Y.-H. Zhang, R.-P. Zhao, F. Zhang, Y.-M. Lu, C.-B. Cai, J. Xiong, and B.-W. Tao, "Biaxial texture evolution in MgO films fabricated using ion beam-assisted deposition," *Journal of Electronic Materials,* vol. 45, no. 7, pp. 3546-3553, 2016.

[72] X. Obradors, and T. Puig, "Coated conductors for power applications: materials challenges," *Superconductor Science and Technology,* vol. 27, no. 4, pp. 044003, 2014.

[73] D. Khatiwada, M. Rathi, P. Dutta, S. Sun, C. Favela, Y. Yao, Y. Li, S. Pouladi, J.-H. Ryou, and V. Selvamanickam, "Passivation Studies on Single-Junction GaAs Thin Film Solar Cells on Flexible Metal Tapes for Low-Cost Photovoltaics," *ACS Applied Energy Materials,* vol. 2, no. 5, pp. 3114-3119, 2019.

[74] J. Chen, and T. Sekiguchi, "Carrier recombination activity and structural properties of small-angle grain boundaries in multicrystalline silicon," *Japanese Journal of Applied Physics,* vol. 46, no. 10R, pp. 6489, 2007.

[75] S. Gsell, M. Schreck, R. Brescia, B. Stritzker, P. N. Arendt, and J. R. Groves, "Iridium on Biaxially Textured Oxide Templates: A Concept to Grow Single

Crystals on Arbitrary Substrates," *Japanese Journal of Applied Physics*, vol. 47, no. 12R, pp. 8925, 2008.

[76] "Iridium-wikipedia," https://en.wikipedia.org/wiki/Iridium.

[77] Y. Li, S. Sun, Y. Gao, Y. Yao, E. Galstyan, P. Rudra, M. Rathi, P. Dutta, S. Pouladi, and J. H. Ryou, "Significant texture improvement in single-crystalline-like materials on low-cost flexible metal foils through growth of silver thin films," *Journal of Applied Crystallography*, vol. 52, no. 4, 2019.

[78] Y. Zhang, T. F. Lehner, T. Fukushima, H. Sakamoto, and D. W. Hazelton, "Progress in production and performance of second generation (2G) HTS wire for practical applications," *IEEE Transactions on applied superconductivity*, vol. 24, no. 5, pp. 1-5, 2014.

[79] S. A. Gourlay, G. Sabbi, F. Kircher, N. Martovetsky, and D. Ketchen, "Superconducting magnets and their applications," *Proceedings of the IEEE*, vol. 92, no. 10, pp. 1675-1687, 2004.

[80] M. S. Zisman, "Technical challenges and scientific payoffs of Muon beam accelerators for particle physics," *IEEE transactions on applied superconductivity*, vol. 18, no. 2, pp. 82-91, 2008.

[81] A. D. Elster. "Radiofrequency Coils - What are the function(s) of radiofrequency (RF) coils? ," http://mriquestions.com/rf-coil-functions.html.

[82] C. E. Hayes, and L. Axel, "Noise performance of surface coils for magnetic resonance imaging at 1.5 T," *Medical physics*, vol. 12, no. 5, pp. 604-607, 1985.

[83] A. D. Elster. "Receive-only RF coils - How do receive-only coils work? ," http://mriquestions.com/receive-only-coils.html.

[84] W. A. Edelstein, R. A. Hedeen, R. P. Mallozzi, S.-A. El-Hamamsy, R. A. Ackermann, and T. J. Havens, "Making MRI quieter," *Magnetic Resonance Imaging,* vol. 20, no. 2, pp. 155-163, 2002.

[85] R. Withers, G.-C. Liang, B. Cole, and M. Johansson, "Thin-film HTS probe coils for magnetic-resonance imaging," *IEEE transactions on applied superconductivity,* vol. 3, no. 1, pp. 2450-2453, 1993.

[86] J. Wosik, L.-M. Xie, K. Nesteruk, L. Xue, J. A. Bankson, and J. D. Hazle, "Superconducting single and phased-array probes for clinical and research MRI," *IEEE transactions on applied superconductivity,* vol. 13, no. 2, pp. 1050-1055, 2003.

[87] J. Wosik, L. Xue, L.-M. Xie, M. Kamel, K. Nesteruk, and J. A. Bankson, "Superconducting array for high-field magnetic resonance imaging," *Applied Physics Letters,* vol. 91, no. 18, pp. 183503, 2007.

[88] I. De Roeck, G. De Winter, R. Van Paemel, R. De Gryse, J. Denul, I. Van Driessche, E. Bruneel, S. Hoste, E. Georgiopoulos, and C. Andreouli, "Rotatable magnetron sputtering of $YBa_2Cu_3O_{7-x}$ thin films on single crystal substrates," *Physica C: Superconductivity,* vol. 372, pp. 1067-1070, 2002.

[89] K. Uhlig, "3He/4He dilution refrigerator with pulse-tube refrigerator precooling," *Cryogenics,* vol. 42, no. 2, pp. 73-77, 2002.

[90] D. Rosenberg, S. Weber, D. Conway, D. Yost, J. Mallek, G. Calusine, R. Das, D. Kim, M. Schwartz, and W. Woods, "3D integration and packaging for solid-state qubits," *arXiv preprint arXiv:1906.11146,* 2019.

[91] J.-H. Yeh, J. LeFebvre, S. Premaratne, F. Wellstood, and B. Palmer, "Microwave attenuators for use with quantum devices below 100 mK," *Journal of Applied Physics,* vol. 121, no. 22, pp. 224501, 2017.

[92] F. Yan, S. Gustavsson, A. Kamal, J. Birenbaum, A. P. Sears, D. Hover, T. J. Gudmundsen, D. Rosenberg, G. Samach, and S. Weber, "The flux qubit revisited to enhance coherence and reproducibility," *Nature communications,* vol. 7, no. 1, pp. 1-9, 2016.

[93] S. Krinner, S. Storz, P. Kurpiers, P. Magnard, J. Heinsoo, R. Keller, J. Luetolf, C. Eichler, and A. Wallraff, "Engineering cryogenic setups for 100-qubit scale superconducting circuit systems," *EPJ Quantum Technology,* vol. 6, no. 1, pp. 2, 2019.

[94] J. Hornibrook, J. Colless, I. C. Lamb, S. Pauka, H. Lu, A. Gossard, J. Watson, G. Gardner, S. Fallahi, and M. Manfra, "Cryogenic control architecture for large-scale quantum computing," *Physical Review Applied,* vol. 3, no. 2, pp. 024010, 2015.

[95] D. B. Tuckerman, M. C. Hamilton, D. J. Reilly, R. Bai, G. A. Hernandez, J. M. Hornibrook, J. A. Sellers, and C. D. Ellis, "Flexible superconducting Nb transmission lines on thin film polyimide for quantum computing applications," *Superconductor Science and Technology,* vol. 29, no. 8, pp. 084007, 2016.

[96] R. Bai, "Superconducting resonators on thin film flexible substrates," Ph. D. dissertation, Auburn Univ., Auburn, AL, USA, 2016.[Online]. Available …, 2016.

[97] Y. Zhang, S. Sun, R. Pratap, E. Galstyan, J. Wosik, and V. Selvamanickam, "Development of REBCO Tapes on Nonmetallic Flexible Substrates for RF Applications," *IEEE Transactions on Applied Superconductivity,* vol. 29, no. 5, pp. 1-5, 2019.

[98] H. Ohya, V. Kudryavsev, and S. I. Semenova, *Polyimide membranes: applications, fabrications and properties*: CRC Press, 1997.

[99] E. incorporated. "Zirconia Ribbon Ceramic," https://www.enrg-inc.com/products/ribbons.

[100] DuPont. "Kapton® Polyimide films," https://www.dupont.com/electronic-materials/kapton-polyimide-film.html.

[101] H. Yousef, K. Hjort, and M. Lindeberg, "Vertical thermopiles embedded in a polyimide-based flexible printed circuit board," *Journal of microelectromechanical systems,* vol. 16, no. 6, pp. 1341-1348, 2007.

[102] Y.-E. Miao, G.-N. Zhu, H. Hou, Y.-Y. Xia, and T. Liu, "Electrospun polyimide nanofiber-based nonwoven separators for lithium-ion batteries," *Journal of Power Sources,* vol. 226, pp. 82-86, 2013.

[103] A. Tiwari, A. Romeo, D. Baetzner, and H. Zogg, "Flexible CdTe solar cells on polymer films," *Progress in Photovoltaics: Research and Applications,* vol. 9, no. 3, pp. 211-215, 2001.

[104] N. Zin, K. McIntosh, S. Bakhshi, A. Vázquez-Guardado, T. Kho, K. Fong, M. Stocks, E. Franklin, and A. Blakers, "Polyimide for silicon solar cells with double-sided textured pyramids," *Solar energy materials and solar cells,* vol. 183, pp. 200-204, 2018.

[105] A. M. Herrera, A. A. Martins de Oliveira, A. P. Novaes de Oliveira, and D. Hotza, “Processing and characterization of yttria-stabilized zirconia foams for high-temperature applications,” *Journal of Ceramics,* vol. 2013, 2013.

[106] E. incorporated. "Thin E-state Material Properties," https://www.enrg-inc.com/documents/Material%20Property%20Table%20V2%202015.pdf.

[107] P. Elumalai, and N. Miura, “Performances of planar NO_2 sensor using stabilized zirconia and NiO sensing electrode at high temperature,” *Solid State Ionics,* vol. 176, no. 31-34, pp. 2517-2522, 2005.

[108] R. You, G. Jing, H. Yu, and T. Cui, “Flexible mixed-potential-type (MPT) NO_2 sensor based on an ultra-thin ceramic film,” *Sensors,* vol. 17, no. 8, pp. 1740, 2017.

[109] M. Aryal, S. W. Allison, K. Olenick, and F. Sabri, “Flexible thin film ceramics for high temperature thermal sensing applications,” *Optical Materials,* vol. 100, pp. 109656, 2020.

[110] S. H. Kim, S. Singh, S. K. Oh, D. K. Lee, K. H. Lee, S. Shervin, M. Asadirad, V. Venkateswaran, K. Olenick, and J. A. Olenick, “Visible flip-chip light-emitting diodes on flexible ceramic substrate with improved thermal management,” *IEEE Electron Device Letters,* vol. 37, no. 5, pp. 615-617, 2016.

[111] C. S. Brian Berland, Alvin Compaan, Victor Plotnikov, David Carey, John, and a. K. O. Olenick, “Ultra-Thin, Flexible Solid-State Battery with Integrated Solar Energy Harvesting,” 2018.

[112] J. A. Olenick. "Zirconia Ribbon Ceramic," https://www.enrg-inc.com/documents/Conference%20Presentations/2018/2018%20AEC%20Presentation.pdf.

[113] M. Kim, J.-H. Seo, U. Singisetti, and Z. Ma, "Recent advances in free-standing single crystalline wide band-gap semiconductors and their applications: GaN, SiC, ZnO, β-Ga_2O_3 , and diamond," *Journal of Materials Chemistry C,* vol. 5, no. 33, pp. 8338-8354, 2017.

[114] G. Xu, A. Salvador, W. Kim, Z. Fan, C. Lu, H. Tang, H. Morkoç, G. Smith, M. Estes, and B. Goldenberg, "High speed, low noise ultraviolet photodetectors based on GaN pin and AlGaN (p)-GaN (i)-GaN (n) structures," *Applied physics letters,* vol. 71, no. 15, pp. 2154-2156, 1997.

[115] J. Millan, P. Godignon, X. Perpiñà, A. Pérez-Tomás, and J. Rebollo, "A survey of wide bandgap power semiconductor devices," *IEEE transactions on Power Electronics,* vol. 29, no. 5, pp. 2155-2163, 2013.

[116] P. Kung, and M. Razeghi, "III-Nitride wide bandgap semiconductors: a survey of the current status and future trends of the material and device technology," *Opto-electronics review,* vol. 8, no. 3, pp. 201-239, 2000.

[117] P. Wheeler, and S. Bozhko, "The more electric aircraft: Technology and challenges," *IEEE Electrification Magazine,* vol. 2, no. 4, pp. 6-12, 2014.

[118] K. O. Armstrong, S. Das, and J. Cresko, "Wide bandgap semiconductor opportunities in power electronics." pp. 259-264.

[119] M. Higashiwaki, and G. H. Jessen, "Guest Editorial: The dawn of gallium oxide microelectronics," AIP Publishing LLC, 2018.

[120] M. Higashiwaki, K. Sasaki, M. H. Wong, T. Kamimura, K. Goto, K. Nomura, Q. T. Thieu, R. Togashi, H. Murakami, and Y. Kumagai, "Current Status of Gallium Oxide-Based Power Device Technology." pp. 1-4.

[121] R. Roy, V. Hill, and E. Osborn, "Polymorphism of Ga_2O_3 and the system Ga_2O_3—H_2O," *Journal of the American Chemical Society,* vol. 74, no. 3, pp. 719-722, 1952.

[122] H. Hasegawa, and H. Hartnagel, "Anodic oxidation of GaAs in mixed solutions of glycol and water," *Journal of The Electrochemical Society,* vol. 123, no. 5, pp. 713-723, 1976.

[123] M. Passlack, E. Schubert, W. Hobson, M. Hong, N. Moriya, S. Chu, K. Konstadinidis, J. Mannaerts, M. Schnoes, and G. Zydzik, "Ga_2O_3 films for electronic and optoelectronic applications," *Journal of applied physics,* vol. 77, no. 2, pp. 686-693, 1995.

[124] M. Ogita, N. Saika, Y. Nakanishi, and Y. Hatanaka, "Ga_2O_3 thin films for high-temperature gas sensors," *Applied surface science,* vol. 142, no. 1-4, pp. 188-191, 1999.

[125] B. Zheng, W. Hua, Y. Yue, and Z. Gao, "Dehydrogenation of propane to propene over different polymorphs of gallium oxide," *Journal of Catalysis,* vol. 232, no. 1, pp. 143-151, 2005.

[126] S. Stepanov, V. Nikolaev, V. Bougrov, and A. Romanov, "Gallium Oxide: Properties and applications - a review," *Rev. Adv. Mater. Sci,* vol. 44, pp. 63-86, 2016.

[127] S. Pearton, J. Yang, P. H. Cary IV, F. Ren, J. Kim, M. J. Tadjer, and M. A. Mastro, "A review of Ga_2O_3 materials, processing, and devices," *Applied Physics Reviews,* vol. 5, no. 1, pp. 011301, 2018.

[128] K. Hoshikawa, E. Ohba, T. Kobayashi, J. Yanagisawa, C. Miyagawa, and Y. Nakamura, "Growth of β-Ga_2O_3 single crystals using vertical Bridgman method in ambient air," *Journal of Crystal Growth,* vol. 447, pp. 36-41, 2016.

[129] G. Sinha, K. Adhikary, and a. Chaudhuri, "Sol–gel derived phase pure α-Ga_2O_3 nanocrystalline thin film and its optical properties," *Journal of crystal growth,* vol. 276, no. 1-2, pp. 204-207, 2005.

[130] H. Son, and D.-W. Jeon, "Optimization of the growth temperature of α-Ga_2O_3 epilayers grown by halide vapor phase epitaxy," *Journal of Alloys and Compounds,* vol. 773, pp. 631-635, 2019.

[131] D.-W. Jeon, H. Son, J. Hwang, A. Polyakov, N. Smirnov, I. Shchemerov, A. Chernykh, A. Kochkova, S. Pearton, and I.-H. Lee, "Electrical properties, structural properties, and deep trap spectra of thin α-Ga_2O_3 films grown by halide vapor phase epitaxy on basal plane sapphire substrates," *APL Materials,* vol. 6, no. 12, pp. 121110, 2018.

[132] S. D. Lee, K. Akaiwa, and S. Fujita, "Thermal stability of single crystalline alpha gallium oxide films on sapphire substrates," *physica status solidi (c),* vol. 10, no. 11, pp. 1592-1595, 2013.

[133] M. Oda, R. Tokuda, H. Kambara, T. Tanikawa, T. Sasaki, and T. Hitora, "Schottky barrier diodes of corundum-structured gallium oxide showing on-

resistance of 0.1 mΩ· cm2 grown by MIST EPITAXY®," *Applied Physics Express,* vol. 9, no. 2, pp. 021101, 2016.

[134] F. Boschi, M. Bosi, T. Berzina, E. Buffagni, C. Ferrari, and R. Fornari, "Hetero-epitaxy of ε-Ga2O3 layers by MOCVD and ALD," *Journal of Crystal Growth,* vol. 443, pp. 25-30, 2016.

[135] M. Baldini, Z. Galazka, and G. Wagner, "Recent progress in the growth of β-Ga_2O_3 for power electronics applications," *Materials Science in Semiconductor Processing,* vol. 78, pp. 132-146, 2018.

[136] Y. Kokubun, K. Miura, F. Endo, and S. Nakagomi, "Sol-gel prepared β-Ga_2O_3 thin films for ultraviolet photodetectors," *Applied physics letters,* vol. 90, no. 3, pp. 031912, 2007.

[137] M. Orita, H. Ohta, M. Hirano, and H. Hosono, "Deep-ultraviolet transparent conductive β-Ga_2O_3 thin films," *Applied Physics Letters,* vol. 77, no. 25, pp. 4166-4168, 2000.

[138] M. A. Mastro, A. Kuramata, J. Calkins, J. Kim, F. Ren, and S. Pearton, "Perspective—opportunities and future directions for Ga_2O_3" *ECS Journal of Solid State Science and Technology,* vol. 6, no. 5, pp. P356-P359, 2017.

[139] A. Blicher, "Physics of semiconductor power devices," *Reports on Progress in Physics,* vol. 45, no. 4, pp. 427, 1982.

[140] M. Mastro, J. Hite, C. Eddy Jr, M. Tadjer, S. Pearton, F. Ren, and J. Kim, "Opportunities and Challenges in MOCVD of βGa_2O_3 for Power Electronic Devices," *International Journal of High Speed Electronics and Systems,* vol. 28, no. 01n02, pp. 1940007, 2019.

[141] H. Von Wenckstern, "Group-III sesquioxides: growth, physical properties and devices," *Advanced Electronic Materials,* vol. 3, no. 9, pp. 1600350, 2017.

[142] Z. Guo, A. Verma, X. Wu, F. Sun, A. Hickman, T. Masui, A. Kuramata, M. Higashiwaki, D. Jena, and T. Luo, "Anisotropic thermal conductivity in single crystal β-gallium oxide," *Applied Physics Letters,* vol. 106, no. 11, pp. 111909, 2015.

[143] B. Chatterjee, K. Zeng, C. D. Nordquist, U. Singisetti, and S. Choi, "Device-Level thermal management of gallium oxide field-effect transistors," *IEEE Transactions on Components, Packaging and Manufacturing Technology,* vol. 9, no. 12, pp. 2352-2365, 2019.

[144] O. Manca, P. Mesolella, S. Nardini, and D. Ricci, "Numerical study of a confined slot impinging jet with nanofluids," *Nanoscale research letters,* vol. 6, no. 1, pp. 188, 2011.

[145] S. Choi, G. M. Peake, G. A. Keeler, K. M. Geib, R. D. Briggs, T. E. Beechem, R. A. Shaffer, J. Clevenger, G. A. Patrizi, and J. F. Klem, "Thermal design and characterization of heterogeneously integrated InGaP/GaAs HBTs," *IEEE Transactions on Components, Packaging and Manufacturing Technology,* vol. 6, no. 5, pp. 740-748, 2016.

[146] K. W. Jung, C. R. Kharangate, H. Lee, J. Palko, F. Zhou, M. Asheghi, E. M. Dede, and K. E. Goodson, "Microchannel cooling strategies for high heat flux (1 kW/cm 2) power electronic applications." pp. 98-104.

[147] J. Pomeroy, C. Middleton, M. Singh, S. Dalcanale, M. Uren, M. Wong, K. Sasaki, A. Kuramata, S. Yamakoshi, and M. Higashiwaki, "Raman

Thermography of Peak Channel Temperature in beta-Ga_2O_3 MOSFETs," *IEEE Electron Device Letters,* vol. 40, no. 2, pp. 189-192, 2018.

[148] M. J. Tadjer, T. J. Anderson, K. D. Hobart, T. I. Feygelson, J. D. Caldwell, C. R. Eddy, F. J. Kub, J. E. Butler, B. Pate, and J. Melngailis, "Reduced self-heating in AlGaN/GaN HEMTs using nanocrystalline diamond heat-spreading films," *IEEE electron device letters,* vol. 33, no. 1, pp. 23-25, 2011.

[149] Z. Cheng, L. Yates, J. Shi, M. J. Tadjer, K. D. Hobart, and S. Graham, "Thermal conductance across β-Ga_2O_3 -diamond van der Waals heterogeneous interfaces," *APL Materials,* vol. 7, no. 3, pp. 031118, 2019.

[150] M. J. Tadjer, "Cheap ultra-wide bandgap power electronics? Gallium oxide may hold the answer," *The Electrochemical Society Interface,* vol. 27, no. 4, pp. 49-52, 2018.

[151] S. H. Lee, S. B. Kim, Y.-J. Moon, S. M. Kim, H. J. Jung, M. S. Seo, K. M. Lee, S.-K. Kim, and S. W. Lee, "High-responsivity deep-ultraviolet-selective photodetectors using ultrathin gallium oxide films," *Acs Photonics,* vol. 4, no. 11, pp. 2937-2943, 2017.

[152] B. R. Tak, V. Gupta, A. K. Kapoor, Y.-H. Chu, and R. Singh, "Wearable Gallium Oxide Solar-Blind Photodetectors on Muscovite Mica Having Ultrahigh Photoresponsivity and Detectivity with Added High-Temperature Functionalities," *ACS Applied Electronic Materials,* vol. 1, no. 11, pp. 2463-2470, 2019.

[153] R. T. Brewer, “Quantitative biaxial texture analysis with reflection high-energy electron diffraction for ion beam-assisted deposition of MgO and heteroepitaxy of perovskite ferroelectrics,” California Institute of Technology, 2004.

[154] R. Lu, R. N. Vallejo, D. W. Fisher, and J. Z. Wu, “Development of textured MgO templates on nonmetallic flexible ceraflex,” *Applied physics letters,* vol. 89, no. 13, pp. 132505, 2006.

[155] S. Gnanarajan, and J. Du, “Flexible Y $Ba_2Cu_3O_{7-\delta}$-coated superconductor tapes on non-metallic substrates with spin-on-glass and IBAD-YSZ buffer layers,” *Superconductor Science and Technology,* vol. 18, no. 4, pp. 381, 2005.

[156] Y. Li, *Microelectronic applications of chemical mechanical planarization*: John Wiley & Sons, 2007.

[157] F. van Vught, “SPIN-ON GLASS MATERIALS AND APPLICATIONS IN ADVANCED IC TECHNOLOGIES.”

[158] T. Mii, and H. Casey, “Properties of spin-on glass as an insulator for InP metal-insulator-semiconductor structures,” *Journal of electronic materials,* vol. 19, no. 11, pp. 1281-1288, 1990.

[159] S. A. Wheelock, J. N. Bremmer, D. S. Schwab, L. Moore, K. Kozel, G. Bujouves, J. Lommel, and D. Rast, “Spin-On Inter-Metal Dielectric Materials: Hydrogensilsesquioxane versus Methylsiloxane,” *SEMICON® China 2003*, 2003.

[160] filmtronics. "SPIN-ON POLYMERS," http://filmtronics.com/capabilities/products/spin-on-polymers.

[161] Futurrex. "Intermediate Coating IC1-200," http://davidlu.net/IC1-200.pdf.

[162] Y. Gao, “High Mobility Single-Crystalline-Like Si and Ge Thin Films on Flexible Substrates by Roll-to-Roll Vapor Deposition Processes,” 2016.

[163] M. J. Tadjer, M. A. Mastro, N. A. Mahadik, M. Currie, V. D. Wheeler, J. A. Freitas, J. D. Greenlee, J. K. Hite, K. D. Hobart, and C. R. Eddy, “Structural, optical, and electrical characterization of monoclinic β-Ga_2O_3 grown by MOVPE on sapphire substrates,” *Journal of Electronic Materials,* vol. 45, no. 4, pp. 2031-2037, 2016.

[164] M. Higashiwaki, K. Sasaki, H. Murakami, Y. Kumagai, A. Koukitu, A. Kuramata, T. Masui, and S. Yamakoshi, “Recent progress in Ga_2O_3 power devices,” *Semiconductor Science and Technology,* vol. 31, no. 3, pp. 034001, 2016.

[165] S. Müller, L. Thyen, D. Splith, A. Reinhardt, H. von Wenckstern, and M. Grundmann, “High-Quality Schottky Barrier Diodes on β-Gallium Oxide Thin Films on Glass Substrate,” *ECS Journal of Solid State Science and Technology,* vol. 8, no. 7, pp. Q3126-Q3132, 2019.

[166] K. Matsuzaki, H. Hiramatsu, K. Nomura, H. Yanagi, T. Kamiya, M. Hirano, and H. Hosono, “Growth, structure and carrier transport properties of Ga_2O_3 epitaxial film examined for transparent field-effect transistor,” *Thin solid films,* vol. 496, no. 1, pp. 37-41, 2006.

[167] R. Wakabayashi, K. Yoshimatsu, M. Hattori, and A. Ohtomo, “Epitaxial structure and electronic property of β-Ga_2O_3 films grown on MgO (100) substrates by pulsed-laser deposition,” *Applied Physics Letters,* vol. 111, no. 16, pp. 162101, 2017.

[168] K. Sasaki, M. Higashiwaki, A. Kuramata, T. Masui, and S. Yamakoshi, "MBE grown Ga_2O_3 and its power device applications," *Journal of Crystal Growth,* vol. 378, pp. 591-595, 2013.

[169] A. Petitmangin, B. Gallas, C. Hebert, J. Perriere, L. Binet, P. Barboux, and X. Portier, "Characterization of oxygen deficient gallium oxide films grown by PLD," *Applied surface science,* vol. 278, pp. 153-157, 2013.

[170] D. J. Comstock, and J. W. Elam, "Atomic layer deposition of Ga_2O_3 films using trimethylgallium and ozone," *Chemistry of Materials,* vol. 24, no. 21, pp. 4011-4018, 2012.

[171] Z. Feng, M. R. Karim, and H. Zhao, "Low pressure chemical vapor deposition of β-Ga_2O_3 thin films: Dependence on growth parameters," *APL Materials,* vol. 7, no. 2, pp. 022514, 2019.

[172] E. G. Víllora, K. Shimamura, K. Kitamura, and K. Aoki, "Rf-plasma-assisted molecular-beam epitaxy of β-Ga_2O_3" *Applied physics letters,* vol. 88, no. 3, pp. 031105, 2006.

[173] L. Kong, J. Ma, C. Luan, W. Mi, and Y. Lv, "Structural and optical properties of heteroepitaxial beta Ga_2O_3 films grown on MgO (100) substrates," *Thin Solid Films,* vol. 520, no. 13, pp. 4270-4274, 2012.

[174] W. Mi, J. Ma, C. Luan, Y. Lv, H. Xiao, and Z. Li, "Characterization of β-Ga_2O_3 epitaxial films grown on MgO (111) substrates by metal-organic chemical vapor deposition," *Materials Letters,* vol. 87, pp. 109-112, 2012.

[175] N. Matsuo, N. Doko, Y. Yasukawa, H. Saito, and S. Yuasa, "Epitaxial growth of MgO/Ga_2O_3 heterostructure and its band alignment studied by X-ray

photoemission spectroscopy," *Japanese Journal of Applied Physics,* vol. 57, no. 7, pp. 070304, 2018.

[176] S. Nakagomi, and Y. Kokubun, "Crystal orientation of monoclinic β-Ga_2O_3 thin films formed on cubic MgO substrates with a γ-Ga_2O_3 interfacial layer," *Journal of Crystal Growth,* vol. 479, pp. 67-74, 2017.

[177] W. Mi, J. Ma, Z. Li, C. Luan, and H. Xiao, "Characterization of Sn-doped β-Ga_2O_3 films deposited on MgO (100) substrate by MOCVD," *Journal of Materials Science: Materials in Electronics,* vol. 26, no. 10, pp. 7889-7894, 2015.

[178] S. Lany, "Defect phase diagram for doping of Ga_2O_3 " *APL Materials,* vol. 6, no. 4, pp. 046103, 2018.